UC Merced

UC Merced Electronic Theses and Dissertations

Title

Computational Modeling of Low Temperature Microplasmas and Applications

Permalink

https://escholarship.org/uc/item/3v14p4d0

Author

Verma, Abhishek Kumar

Publication Date

2020

Copyright Information

This work is made available under the terms of a Creative Commons Attribution-NonCommercial-NoDerivatives License, availalbe at https://creativecommons.org/licenses/by-nc-nd/4.0/

Peer reviewed|Thesis/dissertation

eScholarship.org Powered by the California Digital Library
University of California

UNIVERSITY OF CALIFORNIA, MERCED

Computational Modeling of Low Temperature Microplasmas and Applications

A dissertation submitted in partial satisfaction of the

requirements for the degree of

Doctor of Philosophy

in

Mechanical Engineering

by

Abhishek Kumar Verma

Committee in charge:

Professor Venkattraman Ayyaswamy, Chair
Professor Gerardo Diaz
Professor James Palko
Professor Yanbao Ma

Fall 2020

Computational Modeling of Low Temperature Microplasmas and Applications

Copyright 2020
by
Abhishek Kumar Verma

The dissertation of Abhishek Kumar Verma, titled Computational Modeling of Low Temperature Microplasmas and Applications, is approved:

Chair _____

Venkattraman Ayyaswamy

_____

Gerardo Diaz

_____

James Palko

_____

Yanbao Ma

University of California, Merced

Dedicated to my parents and my sister

Acknowledgments

First and foremost my deepest gratitude goes to my advisor Dr. Venkattraman Ayyaswamy for his enthusiasm, surprising insight, tireless help, and most of all his long-suffering support and mentorship of me. The freedom he provided in exploring the topics that interested me is deeply acknowledged. I am forever indebted to him for guiding me and developing me throughout my time at UC Merced.

I would like to thank the rest of my thesis committee: Professor Gerardo Diaz, Professor Yanbao Ma and Professor James Palko for their insightful comments and reading drafts of my dissertation. I owe Dr. Arghavan Alamatsaz much gratitude for being an amazing colleague and friend.

I thank my parents and my sister for their endless love and unwavering support, and always encouraging me. Finally, I owe my Ph.D. to my family and friends without whose support this day would have remained a dream forever!

Contents

List of Figures

List of Tables

Vita

Abhishek Kumar Verma received the Bachelor of Technology degree in Mechanical Engineering from the Guru Nanak Dev Engineering College, Ludhiana in May 2011. He attended Indian Institute of Technology Kanpur and received his Master of Technology in Aerospace Engineering in July 2014. In August 2015, he entered the graduate school at University of California, Merced as a Ph.D. student working with Professor Venkattraman Ayyaswamy. His research interests include computational plasma physics with an emphasis on low temperature plasmas ignited in microscale dimensions.

Abstract

Computational Modeling of Low Temperature Microplasmas and Applications

by

Abhishek Kumar Verma

Doctor of Philosophy in Mechanical Engineering

University of California, Merced

Professor Venkattraman Ayyaswamy, Chair

We report the development of a modular multiphysics computational framework for performing continuum simulations of low-temperature plasmas. The primary goal of this work is to discuss the features of this framework along with representative results provided as examples for a range of operating conditions and geometries. This includes plasma and plasma-dielectric systems operating in direct current, radio frequency, and microwave regimes from pressures as low as 100 mTorr to atmospheric pressure. The code has several useful features including the ability to run massively parallel simulations using arbitrary geometries, structured/unstructured meshes, choice of various models such as drift-diffusion/full-momentum at runtime, and species-dependent timesteps to name a few. The verification/validation studies presented include comparison with previously published continuum and kinetic simulations with experiments. The performance of the code is also discussed with serial and distributed memory parallel runs with scaling demonstrated up to 512 cores. The design and implementation of the code can be expected to play an important role in computational studies of low-temperature plasmas in academic and industry. As part of the dissertation research, the framework was also used to study direct current and microwave microplasmas with the goal of quantifying the accuracy of continuum simulations in comparison with fundamental kinetic simulations. These results will enable decision-making in the context of choice of simulation strategy while modeling various microplasma devices.

Chapter 1

Introduction

Nonequilibrium low temperature plasmas are of paramount importance for a variety of technological applications ranging from chip manufacturing to the biomedicine and agricultural applications. Plasmas are essentially collection of free charged particles and excited species in addition to the neutrals (atoms, molecules, radicals). All plasmas have several features in common. For instance, they are, on the average, electrically neutral. The charged particles are arranged without any local ordering, being free to move, hence plasmas are electrically conductive in nature. Fully ionized plasma typically occurs at very high temperature, whereas at moderate and room temperatures the plasma is partially ionized. The density of charged species, degree of ionization, the operating mechanism, and the thermodynamic properties of charged species can be used to characterize the plasmas in a broad sense. The thermodynamic classification of plasmas is as following:

- Equilibrium, High Temperature - electrons, gas and ions are in thermal equilibrium and well above practical temperatures. ($T_{electron} \sim T_{ion} \sim T_{gas} \sim 100\ eV$)
- Equilibrium, Moderate Temperature - electrons, gas and ions are in thermal equilibrium and well above room temperature. ($T_{electron} \sim T_{ion} \sim T_{gas} \sim 1\ eV$)
- Non-Equilibrium, Low Temperature - electron temperature much higher than the temperature of the gas and ions and exhibits extreme thermodynamic nonequilibrium. ($T_{electron} \sim 1\ eV;\ T_{ion} \sim T_{gas} \sim 10^2\ K$)

The classification of plasmas based on density–energy parameter space, shown in Fig. 1.1, includes innumerable distinctly different plasmas. An argon plasma containing positive ions only is distinguishable from one containing both negative and positive ions formed in Argon-carbon tetrafluoride plasma.

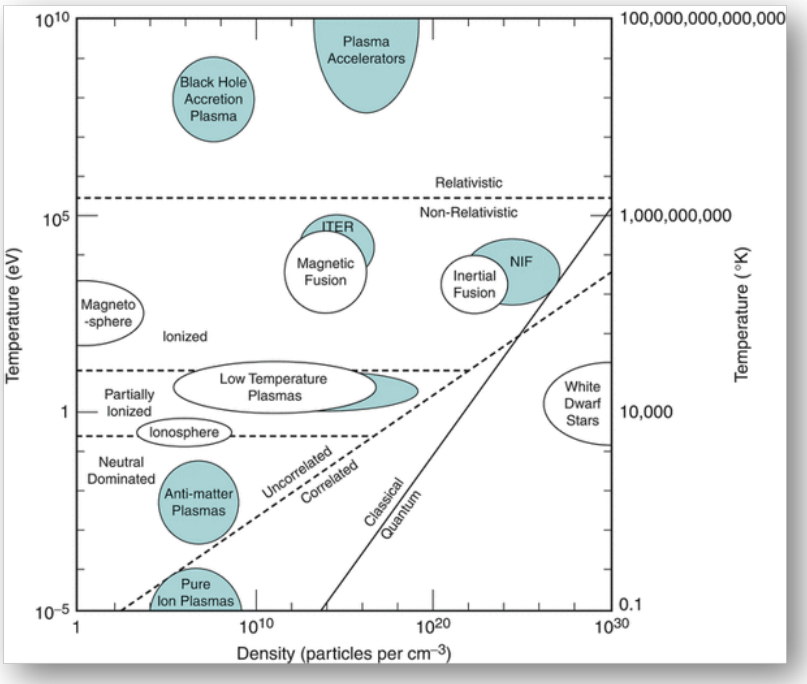

Figure 1.1: A sketch of classification of plasma over density-energy parameter space

The thermonuclear fusion plasmas have very high densities and temperatures (electron temperature $\sim 100 - 10000\ eV$). On contrary, interstellar plasmas (nearly all the matter in the universe) are at low densities and temperature. Non-equilibrium low temperature plasmas are primary focus of this dissertation. These discharges are the most common types of plasmas used in industrial and technological applications. For these discharges, the degree of ionization is small ($10^{-6} - 10^{-4}$), and the thermal non-equilibrium ($T_{electron} >> T_{gas}$) exists between the electrons and heavy particles.

The laboratory or confined plasmas are always essentially in transient state. A dynamic steady state is achieved using continuous or pulsed electrical discharges after the plasma formation, by balance of production and loss of the electrons and ions by various mechanisms. In the steady state, a supply of power is required for production and the energy responsible for production is dynamically transported to the place of loss. The energy from the power source is usually coupled to the electrons in the plasma created by the electric and/or magnetic fields produced by the power source such as direct current (dc), capacitively coupled (RIE, PECVD), inductively coupled

(ICP, TCP, Helicon) and microwaves (ECR, Surfatron).

The origin of charged species in plasma follows various physical and chemical mechanisms. Surface reactions forms major basis for utility of plasma in a range of plasma sources, particularly in surface etching or deposition. Surface production of electrons from a solid surface requires a minimum energy and is called work function. This energy arrives in many forms in different plasma sources: Thermal (thermionic emission including phonons/photons), secondary electrons (bombardment of particles such as ions and excited states), field emission (very high electric field pulling electrons out of surface through quantum tunneling). Surface production of positive ions can be achieved by similar mechanism as secondary electron emission. The most influential mechanism for production in bulk plasma is volume ionization which simultaneously produces electrons and ions. The negative ions are mainly produced by electron attachment with neutral atom or molecule. The volume and surface recombination could also play important roles and works as a sink for charged species.

The fundamental time scale in plasma is defined by the electron plasma frequency:

$$\omega_{pe} = \sqrt{\frac{e^2 n_{electron}}{\epsilon_0 m_{electron}}} \tag{1.1}$$

and the characteristic length scale is defined as the Debye length, which is the length of space charge regions where potential is equal to or larger than $kT_{electron}/e$:

$$l = \sqrt{\frac{\epsilon_0 k T_{electron}}{n_{electron} e^2}} \tag{1.2}$$

where $n_{electron}$, $m_{electron}$, and $T_{electron}$ are the electron density, mass and temperature respectively, and e is the fundamental charge. Plasmas are electrically neutral at length scales larger than the Debye length, and time scales larger than time period of the plasma oscillations.

In general, the electrical neutrality of plasmas is valid over the bulk of the plasma but not close to electrode and dielectric surfaces. The electric field generated by potential gradient accelerates electrons to the walls with higher flux relative to positive ions due to their larger mobilities and lower mass. The new potential structure formed due to negative charge accumulation on surface through high flux of electrons. A thin boundary layer of positive charge adjacent to this surface charge forms, with large potential gradients, leading to the formation of a sheath region in the plasma. This deposition of net positive space charge causes a restoring force to develop which accelerates the positive ions into the walls but the electrons away from it. The sheath is relatively thin region relative to plasma size and so ions can easily pass through it

without collisions and it can be assumed that ions are in free fall from the plasma-sheath interface. This forms the basis of Bohm criterion for minimum ion velocity at the plasma-sheath interface.

$$c_s \geq \sqrt{\frac{kT_{electron}}{m_{electron}}} \tag{1.3}$$

This relation shows that positive ions must come out of the plasma into the space-charge sheath with a minimum speed, therefore quantifies the ion particle flux ($n_{ion,sheath}c_s$) at a normal surface. As such, the sheath characteristics and dynamical properties is critical to materials processing and surface modification because the ion and neutral species fluxes are influenced by the sheath characteristics.

Typically, the electron temperatures are a few eV and the ion temperature is taken same as the gas temperature. The assumption that gas temperature equals ion temperature is valid over a range of pressure, particularly at high pressure where the ion-neutral collision frequency is large, leading to a thermal equilibrium.

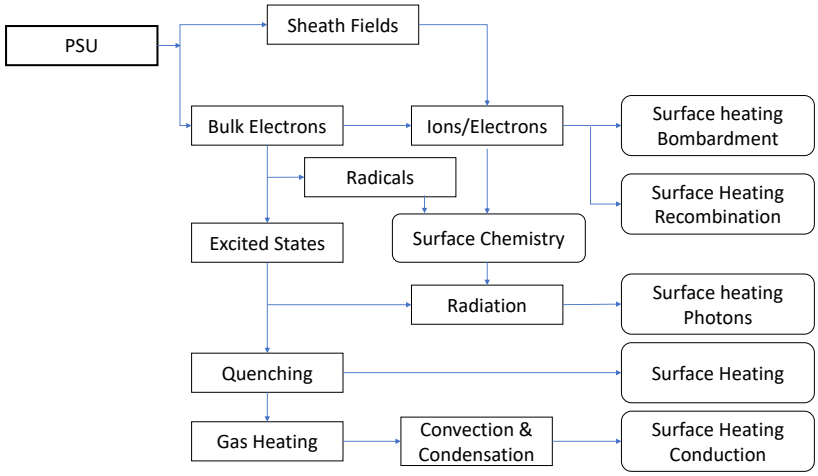

Figure 1.2: Energy flow in low temperature plasmas

The paths by which the electrical energy flows through a laboratory discharge is illustrated in Fig. 1.2.

A complete description of the various physical processes occurring in plasmas is beyond the scope of this work and a comprehensive text on the physics of plasmas can be found in [59].

1.1 Microplasmas

There are two key parameters that need to be considered for low temperature plasma based applications - plasma's characteristic dimension and the gas pressure. For operation in high pressure regime, the characteristic dimensions of the plasma should be in the submillimeter range. These plasmas are traditionally referred to as microplasmas or microdischarges. These plasmas discharges have high charge density, the gas temperatures of $1000-2000\ K$ and operational at high pressures ($100\ Torr-1000\ Torr$).

While early microdischarges/microplasmas were the outcome of the quest to operate stable discharges at or near atmospheric pressure, the advances in micro/nano fabrication have led to rapid miniaturization of microplasma devices with a constant push toward the 1 μm limit. Microplasma devices have been demonstrated to lead to unique physical and chemical mechanisms with diverse applications including electronics [13, 96, 73, 72], nanomaterial synthesis [65], and metamaterials [76] to name a few. The operating regime of these devices has expanded from direct current and low-frequency alternating current to high frequency excitation in the microwave and terahertz regimes thereby enabling low-power high-plasma density operating modes.

Microplasma can be generated by various methods such as direct current [94], microhollow cathode [82], dielectric barrier [67], capacitively coupled [4] and inductively coupled [42] sources. While the direct current [20, 68] and low-frequency [4] excited versions of these microplasmas have contributed to various devices that have revolutionized specific applications, interest has also shifted to igniting microplasmas in microwaves [42, 34, 40] and, more recently, higher frequencies bordering the terahertz regime. The microwave microplasma devices showing enhanced electron confinement have become popular due to capable of demonstrating very long lifetimes and lower power requirements. This enahanced lifetime can be directly attributed to the reduced electrode erosion from particle bombardment. Also, the energy of ions eroding material is very low due to low sheath potentials. The earliest configurations for microplasma ignition using microwaves involved the use of a microstrip split-ring resonator [39]. Other configurations include the use of a transmission line or a surface-wave propagating in a dielectric tube filled with gas [34]. While the earliest microwave microplasmas still involved the use of frequencies less than 1 GHz, recent advances in the field have led to the demonstration of microplasma ignition at millimeter waves with a frequency of 43.44 GHz [74]. Despite the experimental demonstration of various microwave microplasmas and their applications, there is a significant knowledge gap regarding the fundamental understanding of discharge mechanism. Current plasma diagnostics including optical methods [99] face challenges to provide information on fundamental plasma dynamics relevant to microplasmas [2].

In DC microdischarges, the secondary electron emission is the major mechanism

to sustain the discharge [59]. The secondary electron emission is a material property of the electrode over which one seldom has active control. The DC microdischarges characteristics include weak background radiation and high electron temperatures. In general, DC plasmas are operated at low pressures ($1-30\ Torr$) but DC microdischarges are preferred due to simplicity of operation and obviate the use of a vacuum pump at atmospheric pressure. A typical DC microdischarge is represented by micro hollow cathode discharges, which contains a hollow structure, and an arbitrarily shaped anode. The minimum pd value for DC microdischarge is governed by mean free path for electrons must not exceed the hole diameter. The maximum value for pd is due to the inter-electrode distance must not exceed the lengths of the two cathode fall regions [79].

1.2 Computational Modeling

Modeling of low-temperature plasmas involves the interplay of various physical and chemical phenomena that span several time/length scales and is of immense importance to many scientific and technological applications [49]. Specifically, they involve non-linear interactions between charged particles and radicals existing in non-equilibrium conditions apart from being affected by externally applied or self-induced electromagnetic fields. Scientific computing, in tandem with theory and experiment, has an extremely high potential to assist/lead in the development of low-temperature plasma systems. In this context, low-temperature plasma modeling techniques mainly fall into two categories: particle and continuum methods. Continuum simulation methods play a significant role in the large-scale modeling of engineering problems of interest because of the relatively low computational cost (in comparison with kinetic methods). The plasma fluid model is described by a set of conservation equations constructed by taking velocity moments of the Boltzmann equation using a presumed velocity/energy distribution function for each species. Furthermore, this model coupled with the Maxwell's equations fully describes the dynamics of a self-sustained plasma. On the other hand, particle models deal with a Lagrangian formulation of plasmas and are very useful in resolving kinetic behavior and multiscale dynamics of low-temperature plasmas. However, as discussed earlier, they suffer from a high computational cost when compared to continuum models and may even be infeasible for certain real-world problems [45]. Over the years, fluid modeling has evolved to a level where it can closely mimic the dynamics of various plasma processes and is widely used for both fundamental and applied research.

In this context, there has been constant interest in the development of high-fidelity computational methods for simulation of plasmas over the last few decades. In par-

ticular, simulation methods have seen a sustained level of improvement, and in partnership with modern computational hardware, have facilitated a multifold increase in the use of high performance computing (HPC) in the low-temperature plasma community. However, it would not be an overstatement to say that plasma fluid modeling has not been well-positioned in terms of adoption of novel techniques and developments in numerical computing, development of new numerical methods, high performance programming paradigm and utilization of advances in HPC (parallelism, streaming architectures etc.). This is particularly true when we compare advances in fluid modeling of plasmas to other areas of computational science such as computational fluid dynamics (CFD), and molecular dynamics (MD). Many self-consistent, modular, multi-dimensional in-house and commercial plasma solvers are available for the plasma research community, such as MOOSE(Shannon group, North Carolina State University/Argonne National Lab) [61], HPEM (Kushner group, University of Michigan) [49], PLASIMO (Eindhoven University of Technology) [18], and COMSOL Multiphysics®. However, there appears to be the lack of a modern, general-purpose code that is extensible and includes key features that are required to capture both physical and chemical phenomena that are unique to low-temperature plasmas and this effort is an attempt to fill this void.

To summarize, having reviewed the literature and to address key fundamental challenges in the field of low temperature plasma physics, a new tool for plasma simulation, is necessary for many reasons discussed above. Low temperature plasma physics is a rich area of physics and chemistry that involves complex mechanisms. A versatile simulation framework for low temperature plasma simulations should be massively parallel, utilizes efficient numerical schemes, highly flexible, highly extensible and allows wrapping of external libraries.

1.3 Objectives

The role of computations is critical to obtain a complete understanding of the operation of low temperature plasmas with the goal of design and optimization for a given application. The available plasma simulation frameworks and previous studies are largely based on gross simplification of continuum plasma model and hence do not provide adequate detail. To alleviate some of these issues, a self-consistent model based on plasma fluid and Maxwell's equations was implemented in a simulation toolbox. The main goal of this work is to develop and design this toolbox with a range of features, study the parallel efficiency, perform validation and verification; a continuum plasma solver developed inside Eulerian finite volume framework in *foam-extend*. Furthermore, the framework was used to study direct current and

microwave microplasmas with the goal of quantifying the accuracy of continuum simulations in comparison with fundamental kinetic simulations. These results will enable decision-making in the context of choice of simulation strategy while various modeling microplasma devices.

The primary objective of the framework design is to be able to perform plasma simulations using a high-level interface, while maintaining appropriate level of abstraction for further extension such as coupled multiphysics, design optimization and uncertainty quantification. In general, performing complex and multiphysics plasma simulation is very tedious task while dealing with case setup and software at the source code level. The user interface produces huge amount of overhead to set up physical conditions, choosing appropriate model for specific problem, numerical parameters etc. On the other hand, to maintain considerable flexibility of multiphysics framework, one preferably chooses to write tools and couple established codes together, where one has to deal with incompatible data structure, code practices, library interface etc. To answer some of these issues, one of the major design choice for this framework is to use OpenFOAM C++ code practices.

The developed plasma simulation framework is used to study the following problems.

- Simulation of GEC reference cell and one-dimensional radio frequency capacitively coupled plasma. This work is intended at extensive validation from simulation and experimental results available in literature. It also provides insights into the features and capability of framework.
- Simulation of a confined microdischarge with curved dielectric surfaces and Helium plasma needle. These simulations are aimed at exploring the nature of the micro hollow cathode discharge and dielectric barrier discharge.
- Simulation of argon microplasmas operating in the direct current and microwave regimes. This study aims at comparisons between continuum and kinetic simulations.

1.4 Dissertation Outline

The rest of this dissertation delves into the development of proposed framework and demonstrates its utility through validation and verification cases and microplasma simulations.

Chapter 2 outlines governing equations describing fundamental equations describing low temperature plasma systems. Chapter 3 describes the framework in detail,

the need for which was outlined in section above. The performance of the framework is demonstrated alongside simulations of various low temperature plasma configurations.

Finally, the computational framework is applied to microplasma problems in chapter 4. A detailed study of DC and microwave microplasma is presented. These results are compared with results from particle-in-cell results. Accuracy and utility of fluid model in the context of microplasma is presented and limitations are discussed.

Concluding remarks and future directions for research and improvements are provided in chapter 5.

Chapter 2

Computational Model

In this chapter, the physical and computational model used in this study is described in detail. The computational model mainly focuses on microplasma simulations but could be applicable to all forms of low temperature plasmas.

2.1 Governing equations

A brief overview of the plasma governing equations is provided here. The code employs a plasma fluid model which is essentially derived by taking velocity moments of the Boltzmann equation [8] and is coupled with the Poisson's equation thereby providing an electrostatic description of the plasma. It should be mentioned that the formulation closely follows the description by Fitzpatrick [21] and is summarized here for self-sufficiency.

A continuum model describes the plasma dynamics by a set of macroscopic parameters such as density, momentum, and mean energy for each species. The temporal evolution of these variables is determined by solving the governing plasma fluid equations. At a microscopic level, the Boltzmann-Vlasov equation may be used to describe the dynamics of charged particles and is given by

$$\frac{\partial f}{\partial t} + v \cdot \nabla f + \frac{q}{m}(E + v \times B) \cdot \frac{\partial f}{\partial v} = Q(f, f^{'})$$

where f is the velocity distribution function of a given species in phase space, $\mathbf{v}$ is the particle velocity, E is the electric field, and B is the magnetic field . The right-hand side of the above equation describes the collisions contributing to a rate of change in the velocity distribution function.

In most plasma sources, frequency is sufficiently low such that the electric and magnetic fields can be assumed to be quasi-static. Furthermore, in the Lorentz force

term (last term on the left hand side), electric field is the dominating term which makes the contribution of magnetic field negligible in most cases [32]. With these assumptions, the Maxwell's equations in Couloumb gauge is reduced to

$$\nabla \times E = 0, \quad \nabla \cdot E = \frac{\rho}{\varepsilon_0}$$

Also $E = -\nabla\phi$, which transforms above equation to a standard Poisson equation, here ρ is net charge density and ϕ is scalar potential associated with curl-less electric field. The macroscopic quantities on which the fluid equations will be established are either defined or derived using the first three velocity moments of the distribution function f, namely particle density $n(x,t)$, mean velocity $u(x,t)$, energy flux $Q(x,t)$, temperature and pressure tensor.

We obtain equations relating these macroscopic quantities by taking the first velocity moments of the Vlasov-Boltzmann equation, which reduces computational difficulty from 6 dimension in phase space to 3 dimension in Cartesian coordinates. In the computation, we shall use that distribution function f vanishes at infinity and that the plasma is periodic in space. Finally, the general form of fluid equations up to two order velocity moments for one monoatomic specie present in plasma:

$$\frac{\partial n}{\partial t} + \nabla \cdot (n\mathbf{u}) = Q$$

$$m\frac{\partial (n\mathbf{u})}{\partial t} + m\nabla.(n\mathbf{u} \otimes \mathbf{u}) + \nabla(p) = qn\mathbf{E} + \mathbf{Q}_p^{'}$$

$$\frac{\partial}{\partial t}(\frac{3}{2}p + \frac{1}{2}mn|\mathbf{u}|^2) + \nabla.(\frac{5}{2}p\mathbf{u} + \frac{m}{2}n|\mathbf{u}|^2\mathbf{u}) + \nabla.(\mathbf{L}) = E \cdot (qn\mathbf{u}) + Q_E^{'}$$

which corresponds, in three dimensions, to a system of 5 scalar equations with 5 scalar unknowns which are the density n, the three components of the mean velocity u and the scalar pressure p (neglecting viscosity and anisotropic effects). L is defined as heat flux, Q,$\mathbf{Q}_p^{'}$ and $Q_E^{'}$ are conservative and non-conservative collisional contribution to continuity, momentum and energy equation respectively.

2.2 Numerical formulation, input parameters & closure

Here we discuss some important variations in numerical formulation and their closure, along side relevant transport and numerical input parameters for LTP modeling. The

framework has multiple formulation to resolve different level of details (multiscale, multiphysics) to simulate broad range of applications. It provides the feature to selectively include the different physical model at run time and follows formulation available commonly in literature [16, 12].

Over years, improvements in continuum plasma models and closure approximation has provided us capabilities to include many kinetic and particle interaction effects in the scope of fluid modeling. For most practical problems, closure for scalar pressure is derived by assuming thermodynamic equilibrium, hence can be computed by ideal gas law. The higher order moments are truncated in the second order to provide explicit algebraic expression for heat flux L, where it may be modelled based on Fourier approximation with thermal conductivity

$$K = \frac{5}{2m_i\nu_i} n_i k_b^2 T_i$$

The collisional terms can be approximated as:

$$Q = \sum R_{i,j}$$

$$\mathbf{Q}_p^{'} = (\mathbf{u}Q + \mathbf{Q}^p) = -\sum_j \frac{m_i m_j}{m_i + m_j} \nu_{ij} n_i (u_i - uj) + \sum_{j|R_{ij}<0} m_i u_i R_{ij} + \sum_{j|R_{ij}>0} m_j u_j R_{ij}$$

$$Q_E^{'} = (\frac{1}{2}|\mathbf{u}|^2 Q + \mathbf{u}.\mathbf{Q}^p + Q^E) = -\sum_j \frac{m_i m_j}{m_i + m_j} \nu_{ij} n_i \big[(m_i u_i.u_i - m_j u_j.u_j + (m_i - m_j) u_i.u_j)$$

$$+3k_b(T_i - T_j)] + \sum_{j|R_{ij}<0} \frac{1}{2}(m_i u_i.u_i + 3k_b T_i) R_{ij} + \sum_{j|R_{ij}>0} \frac{1}{2}(m_j u_j.u_j + 3k_b T_j) R_{ij} + \sum_j \epsilon_{ij} S_{ij}$$

where i and j are indices such that ith specie solution will include interaction with the jth specie present in plasma. R is gain/loss in inelastic reactions, S is gain/loss of specie in inelastic collisions and ϵ is corresponding energy gain/loss. ν is momentum transfer frequency in elastic collisions. m is mass and T is temperature of the specie. k_b and q are Boltzmann constant and specie charge respectively.

In many cases, the momentum conservation equation is replaced by a simplified drift-diffusion (DD) model obtained by neglecting the inertial effect and some less influential physical effects [37, 87]. The DD model's primary advantages include ease of implementation and reduced computational cost. The DD equation is given by

$$\mathbf{\Gamma_i} = \mu_i n_i \mathbf{E} - \eta_i \nabla(n_i k_b T_i)$$

where $\mathbf{\Gamma_i} = n_i \boldsymbol{u_i}$ is specie flux. The mobility $\mu_i = q_i/m_i\nu_i$ and $\eta_i = D_i/m_i\nu_i$, with D being the diffusion constant and $\nu_i = \sum_j \nu_{ij}$ is total collisional frequency. The first term in the above equation models the effect of electric field on charged particles (drift) and the second term accounts for the effect of diffusion in a nonuniform plasma.

The transport parameters and rate coefficients for plasma specie depend mainly on velocity distribution function. Fluid model truncation closure scheme requires a presumed velocity distribution function, commonly chosen to be Maxwell-Boltzmann distribution function, and is used to compute unknown parameters. This way all fluid model parameters and closures are divided between assumption of thermodynamic equilibrium and non-equilibrium. To be able to perform self-sustainable plasma modeling, one has to judiciously choose the model parameters based on availability of accurate description, mathematical and computational demand. Most charged specie transport parameters can be obtained by either solution of approximated Boltzmann equation or Monte Carlo methods. Reaction coefficients are based on combining empirical and first principle studies of plasma specie.

This section attempts to provide a brief overview of extensive theoretical development of plasma continuum model applicable to LTP, which can be seen as archetype example of multiscale, multiphysics and complex phenomenon. The work done here is based on many extensions of this theory and the results include references to precise formulation used to perform specific simulation.

Chapter 3

Numerical Framework

In this work, we introduce a modern low-temperature plasma simulation software called SOMAFOAM (an acronym for **S**imulations **O**f plas**MA** using **F**ield **O**peration And **M**anipulation) based on the multiphysics toolkit *foam-extend*, which is a popular variant of the OpenFOAM® [93] finite volume framework. Incidentally, the term Soma has also been used to refer to plasma in ancient Indian literature (Rig Veda). It is important to discuss the reasons for the adoption of OpenFOAM as the underlying foundation for our code. The OpenFOAM framework provides multi-dimensional simulation capabilities on mixed-element polyhedral mesh with support for complex geometry along with a vast resource of validated numerics (including but not restricted to field algebra, boundary conditions, sparse matrices, and finite volume space discretization). While a lot of the underlying numerical capabilities required for the development of a code for continuum simulations of low-temperature plasmas are already available in OpenFOAM, extensive code development was required to enable the addition of the unique features specific to plasma modeling. Some of the features of our code include the capability to simulate an arbitrary number of plasma species apart from providing a high-level interface for the choice of species transport equations (drift-diffusion vs full-momentum). The plasma chemistry library builds on the existing OpenFOAM chemistry library to include support for reactions depending on electron as well as gas temperatures apart from the ability to utilize features such as reduced chemistry. The electrostatic solver could be used for plasma only or any configuration involving plasma and dielectric regions.

The OpenFOAM framework is highly influenced by the use of object orientation and template meta-programming to provide modular C++ class structure and high mathematical abstraction. These features combined with complex geometry support, automatic mixed meshing, massive parallelization, well established pre/post-processing capabilities and a large set of supporting tools make OpenFOAM an op-

timal choice as a master code for SOMAFOAM. Also, OpenFOAM can provide potential interoperability between a range of multiphysics solvers (fluid mechanics and heat transfer, reaction and physical kinetics, direct simulation Monte Carlo (DSMC), Multiphase flows etc.) for a coupled description that could be important for certain plasma applications. While it does not exist as of date, the direct simulation Monte Carlo code of OpenFOAM could be extended to create a particle-in-cell-Monte Carlo collisions (PIC-MCC) code within OpenFOAM that could provide us with an open-source hybrid plasma simulation tool in future.

In this regard, the primary purpose of this work is to describe representative features of our code and back it with relevant verification/validation and parallel efficiency studies.

3.1 Implementation, structure and models

The major component of the toolbox as part of this work has been developed using the open source utility *foam-extend* which is a popular derivative of the OpenFOAM solver suite. OpenFOAM is essentially a numerical environment to solve partial differential equations that are commonly encountered in continuum mechanics. In addition to that, it provides suitable data structures for extensions to particle methods (dsmcFoam, mdFoam are two examples available already). OpenFOAM is written in C++ and uses object orientation and generic programming which makes it a suitable platform for library development as shown in the code structure below. It uses the staggered grid formulation of the finite volume method for the discretization of equations wherein flux quantities are stored at the faces while conservation variables are stored at the cell centers. The solution variables in tensorial formulation are abstracted as arbitrarily unstructured internal and boundary fields at discrete points in the domain. A large number of numerical schemes are provided for associated mathematical operators such as divergence, laplacian etc., and could be easily modified by the user. A more exhaustive introduction to OpenFOAM can be found elsewhere [93].

One of the goals of this framework is to develop a convenient user interface with high performance and flexible structure. The main solver of SOMAFOAM itself performs only the role of coordinating the calling of various functions that are implemented elsewhere. In this regard, the underlying element of our code is the `plasmaCookBook` module that is designed for the numerical solution of the plasma governing equations. All plasma species continuity and flux/momentum equation models inherit a virtual base class `multiSpeciePlasmaModels`. The design interface allows the user to create new physical models by using existing class implementations as a template and by inheriting the base class. The code design for the

`multiSpeciePlasmaModels` class is depicted using the Universal Modeling Language (UML) block diagram and shown in Figure 3.1 in order to provide an idea of the software design.

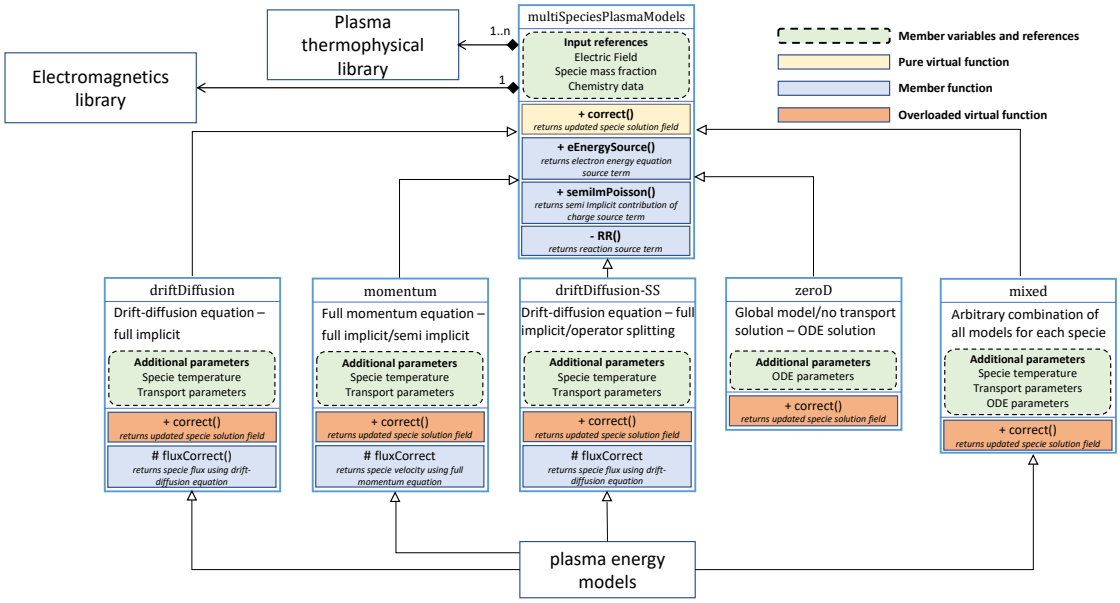

Figure 3.1: The UML class diagram of the SOMAFOAM computational framework

The `multiSpeciePlasmaModels` class solves the continuity equation in conjunction with the drift-diffusion/full-momentum equation in a segregated manner using a cell-centered finite-volume method. The `driftDiffusion` and `momentum` classes implement the drift-diffusion and full-momentum equation respectively in full implicit/explicit and ImEx (Implicit-Explicit) forms. Implicit solution of the continuity equation is achieved by an implicit source term treatment [69] which facilitates matrix diagonal dominance and hence better numerical stability. The full-momentum equation solution is based on a semi-implicit implementation and largely follows [15]. Operator splitting is a commonly deployed method to handle highly non-linear advection-diffusion-reaction partial differential equations. The objective here is to split advection-diffusion and reaction components in order to deal with the tightly coupled nature of these mechanisms. `driftDiffusion-SS` implements the Strang splitting method [85, 64] to achieve stable and accurate solution in time and the implementation follows closely from section III.A of [95]. The stiff chemical source term is integrated using OpenFOAM's `ODE` library.

The `plasmaBoundaryConditions` class implements domain-specific boundary conditions for plasma governing equations and are largely based on descriptions in [60, 92]. `plasmaEnergyModels` class is designed to provide multi-temperature species energy equation of charged and neutral particles. The implementation supports ImEx and explicit formulation of energy equation for electron, ions and neutral species. Implementation of the neutral species energy equation is similar to the description provided in [50]. `electroMagnetics` class provides a lot of flexibility in terms of numerical solutions of Maxwell's equations and coupling of plasma-dielectric regions. A general-purpose solver for Poisson's equation is available, with explicit inclusion of charged species. A linearized and semi-implicit formulation is also available for certain specie solution. All the governing equations are implemented in a segregated manner. Traditionally, coupled formulation provides better convergence but at the cost of high memory requirement and numerical complexity. To provide a general-purpose plasma solver, segregated implementation is more suitable as the required implicit/explicit formulation can be achieved with high flexibility, matrix size scaling with variables and low memory overhead.

`plasmaThermophysical` library is concerned with reactions, thermal/physical properties of plasma and background gas. Plasma chemistry modeling and thermophysical parameters have many unique requirements as compared to traditional thermophysical library for reacting flow modeling that is available by default in OpenFOAM. We modified and extended the existing `thermophysical` library for efficient calculation of plasma chemistry, thermophysical source term and transport parameters: a significant development from the limited pressure-temperature system already implemented in OpenFOAM. The library includes a range of possible combinations for plasma reactions, thermodynamic state and transport mechanism using C++ templates. The library provides an abstraction layer beginning from the equation of state to reaction dynamics while maintaining the original OpenFOAM chemistry interface. The transport and reaction data can be imported from BOLSIG+ [29], a popular freeware for solution of the zero-dimensional Boltzmann's equation using a two-term approximation. Also, transport parameters can be described as constant or as a function of local reduced electric field or local mean energy. A tabular interface is created inside the library to facilitate efficient interpolation of transport and reaction data.

The framework provides an optimal interface to support multiphysics and multiscale simulation. Multiple time scales can be chosen at run time to facilitate simulation with large time scale disparity. The library interface is such that the user could choose to extend plasma solution to include neutral gas flow, lagrangian dynamics, multiphase flow, heat transfer etc., by combining any established solver available in OpenFOAM. The code infrastructure maintains extensive use of operator overloading and template metaprogramming in OpenFOAM. This practice facilitates quick

translation of scientific models into efficient finite volume code with auxillary numerics. Also the performance centric implementation of C++ directives and distributed memory parallelism allow this framework suitable to use from laptop to large high-performance computers. The code snippet below shows the conversion of a given partial differential equation - in this case the ion/neutral gas energy equation [1] - to OpenFOAM code.

```
//Generic Equation:
```

$$\frac{\partial(n_i C_p T_i)}{\partial t} + \nabla \cdot (-\kappa_i \nabla T_i) + \nabla \cdot (\mathbf{\Gamma_i} C_V T_i) = -p_i \nabla \cdot \vec{v_i} + D_i + P_i \tag{3.1}$$

where n_i, T_i, $\mathbf{\Gamma}_i$, $\mathbf{v}_i$ and p_i are number density, temperature, species flux, mean velocity and scalar pressure of species i. D and L represent energy lost due to collision drag and input power respectively.

```
//Openfoam code:

fvScalarMatrix TiEqn
(
  fvm::ddt((Ni*Cp), Ti)
  - fvm::laplacian(kappai, Ti)
  + fvm::div((gammai*Cv), Ti)
  ==
  - pi*fvc::div(vi)
  + Di + Pi
);

TiEqn.solve();
```

In the template above, the energy equation is being solved in semi-implicit formulation. Static function `fvm` produces implicit terms for the matrix solution and `fvc` performs finite volume operations on rest of the terms for explicit treatment of terms resulting in contributions to the right hand side of resulting matrix system $Ax = b$. `ddt, laplacian, div` are differential operators implemented as static functions for the discretization of solution and other field variables. `fvScalarMatrix` class is discretized after inheriting the finite volume mesh and field variables classes

and produces a sparse solution matrix. The solution of the equation is achieved by user-provided parameters for space and time discretization, interpolation techniques and matrix iterative solvers (Krylov subspace methods) at runtime.

3.2 Multi-region coupling

Most practical plasma applications have one or more dielectric materials used, either for plasma confinement or for the formation of barrier discharges. Hence, a plasma-dielectric coupled simulation is one of the common features expected from a plasma modeling framework. The plasma-dielectric interface requires the inclusion of the accumulated surface discharge into Gauss' Law (Poisson's equation) for a consistent electrostatic solution, as detailed in [97]. A popular method to couple multiple region/mesh such as plasma-dielectric medium is weak or explicit coupling and is commonly available in solvers for low-temperature plasma simulation. Explicit coupling involves multiple solvers operating in different regions of the mesh. Each solver handles its own region and coupling is achieved through boundary condition update. Convergence to a solution is usually achieved by iteration techniques such as Picard's method [44]. This method is trivial to implement and provides flexibility of solver and numerical implementation choices. However, it suffers heavily from weak or no convergence.

On the other hand, strong coupling or implicit coupling can provide a way to achieve faster convergence coupled with efficient solution method for given systems of equations. In this work, a solution matrix level coupling is implemented for the solution of Poisson's equation over the plasma and dielectric regions. A coupled matrix system couples matrices for each mesh region. The surface discharge and accurate description of interface physics is enforced by manipulating the inner face values between matrices. The coupling boundary condition is a critical component to achieve performance. A general grid interface (GGI) algorithm for the boundary condition [11] is used in order to handle partially overlapped, non-coincident mesh interfaces. The linear coupled solver, based on biconjugate gradient stabilized method (BiCGSTAB), utilizes internal solver sweeps for all coupled matrices. In this way every mesh region has its own solver control and physics, while they can take advantage of the robustness of the tightly coupled solution. The implementation in SOMAFOAM could be extended as described in [48] for more optimized solution control.

Code Performance

Single node performance

Single node/core performance is evaluated on a Dell machine with Intel® Xeon Gold 6140 CPU @2.30GHz with Hyper-threading enabled. To conduct this evaluation, a three dimensional GEC reference cell geometry is chosen which is briefly described in subsection 3.3. The code was compiled using Intel® Parallel Studio XE 2019 (Intel® C++ compiler with Intel® MPI library) on a CentOS linux based machine and uses Intel® VTune™ profiler. To analyze the performance results, all software kernels are grouped into these categories: plasma dynamics, plasma chemistry, coupled poisson equation matrix and MPI.

The GEC reference cell mesh shown in figure 3.2, consists of plasma and dielectric section, with 1990400 and 35840 block structured hexahedral mesh cells respectively. Rest of the simulation parameters are same as described for case 1 in subsection 3.3. A simulation case containing three species Ar, Ar^+, e^- and one ionization reaction uses 60% of CPU time spend on plasma solution including 7.5% of CPU time for plasma chemistry related solution. 30% of CPU time is involved in coupled Poisson's equation solution. Another case containing four species Ar, Ar^+, Ar^*, e^- and six reactions shows plasma solution time as high as 70% including 24% plasma chemistry solution time of total CPU time. The coupled Poisson's equation solution time is 20%.

The parallel profiling on a single node was done with varying number of cores of the machine. Parallel configuration details are same as described in section below. The Intel® MPI library auto tuning was used along with process pinning on physical cores. The VTune™ `hpc-performance` analysis shows efficient parallel implementation. The MPI imbalance was less than 2% for all runs, showing efficient communications operations and low overhead. The MPI busy wait time was shown to be less than 0.01% of CPU time, showing balanced domain decomposition, efficient linear solver and preconditioner operations. OpenFOAM's parallel functions responsible for communications `MPI_Allreduce/MPI_Recv/MPI_Waitall` tend to be less than 2% of wall time, which makes this application suitable for massive parallel simulation. Traditionally mesh based continuum methods' performance tend to be memory bandwidth bounded and this application is not an exception as the VTune™ `hotspots` analysis shows high memory bound parametric value.

Parallel Scalability

Parallel scaling analysis is done on 347 mixed nodes machine, Triton Shared Computing Cluster (TSCC) of San Diego Supercomputer Center using General Computing

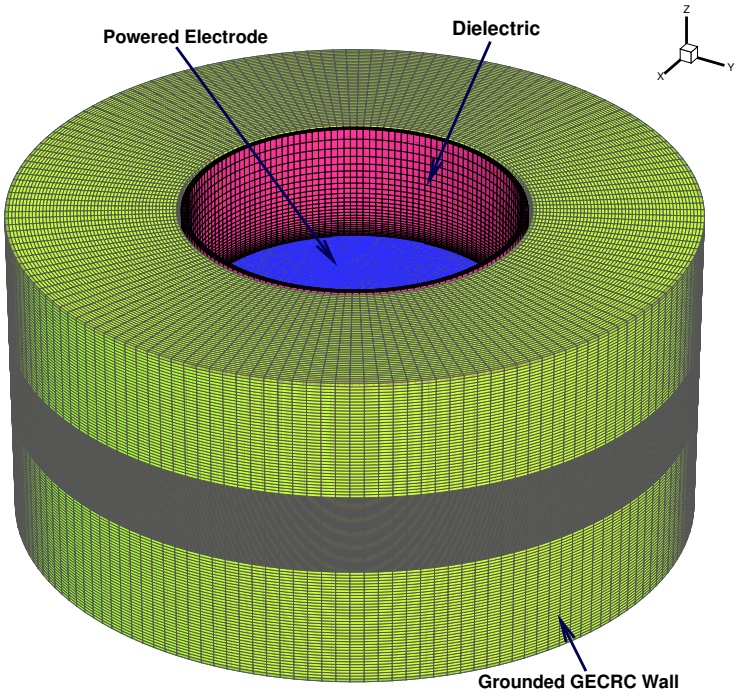

Figure 3.2: Three dimensional GEC reference cell geometry and computational mesh

Nodes which mostly consists of dual-socket, 8-core, 2.6 GHz Intel Xeon® E5-2670 processor. For the purpose of scaling analysis, simulations of three dimensional capacitively coupled GEC reference cell has been performed. The simulation parameters and geometry are same as used for single node performance analysis. An optimized code was used for this study and is built on top of OpenFOAM-v1906. The code was compiled with Intel® Icc compiler 2016.3.210 with Intel MPI. The toolbox provides distributed memory parallelism based on domain decomposition: a typical for OpenFOAM based solvers and can be used with any standard MPI implementation to perform parallel simulations. In this study, the multi-region domain was decomposed using graph partitioning software METIS [43] using k-way/recursive multilevel partitioning algorithm. The final choice between partitioning algorithm is made after performance testing. Partitioning is done in away that each partitioned region corresponds to a unique MPI process. In this study, data structure optimization or effect of parallel data I/O on parallel performance is not performed and can be a topic for future study. No particular optimization flag or environment variables other than default settings for compiler and any supporting library was used, in order to

present a general result. The communication cost of MPI could be bottleneck for the overall performance. The communication cost was minimized by using non-blocking MPI communications, parallel consistent linear solver and preconditioner. We chose to look performance of the code till 1024 cores/32 nodes which is acceptable count for feasible computational resource and problem size/complexity in most capacity computing runs.

Parallel scalability study is performed by classical test measures for time to solution, strong and weak scaling. Strong scaling keeps the total problem size fixed and processors count (P) varies, whereas weak scaling keeps the problem size per processor (x) fixed for the same. Perfect scaling for strong scaling analysis would corresponds to solution in $1/P$ time and for weak scaling, solution time should be same for Px problem size. For cell-centered finite volume method, computational cost per cell for up to second order schemes is relatively very low as compared to high order numerical methods. This puts a high lower bound for mesh cells per partition to be able to outweigh computational cost to communication cost. The higher bound on number of mesh cells per partition may comes from hardware related factors, such as processing power, memory bandwidth etc. Beyond these bounds, parallel performance degrades rapidly.

The geometry of GEC reference cell along with block structured mesh is shown in figure 3.2. The capacitively coupled Argon plasma includes Ar^+ ions and electrons. For simplicity only ionization reaction is included. The plasma species solution is achieved by solving continuity, momentum and energy equation for both specie. A second order second order upwind euler time method for temporal discretization and second order central differencing for spacial discretization is used along with Sweby limiter [86] for convective terms. The Poisson's equation solution is achieved in explicit formulation using geometric agglomerated algebraic multigrid method. The boundary conditions for all solution variables are same as described in [92]. The dielectrics are not include in this study for simplicity and an approximate dielectric boundary condition is used, similar to described in [47].

A single node parallel scalability test was established first. The machine used is two socket 18 core Intel® Xeon Gold 6140 CPU @2.30GHz running with Hyper-threading enabled, providing up to 72 logical cores. The results for strong scaling efficiency is presented in figure 3.3. The fine and coarse mesh cases consists of 1990400 and 15923200 hex cells respectively. The lower cell count is chosen based on analysis done on 2D axisymmetric solution, satisfying mesh requirement for stable solution for both implicit and explicit solution. Although a rigorous grid refinement/order of convergence analysis could be used to develop better understanding but excluded from this study. The results can be analyzed based on dynamics of memory cache, CPU sockets and Hyper Threading etc. It can be seen from results that scaling

efficiency for both cases reduces as the cores count increases. The total memory footprint of this simulation on single node is too large for any of the parallel runs. In this case, increasing the core count can not provide more parallel performance as the simulation is not CPU bound and performance deteriorates further by increasing core count because of communications overhead. It can be seen that negative effect of hyperthreading become apparent at higher thread counts for fine mesh simulation case.

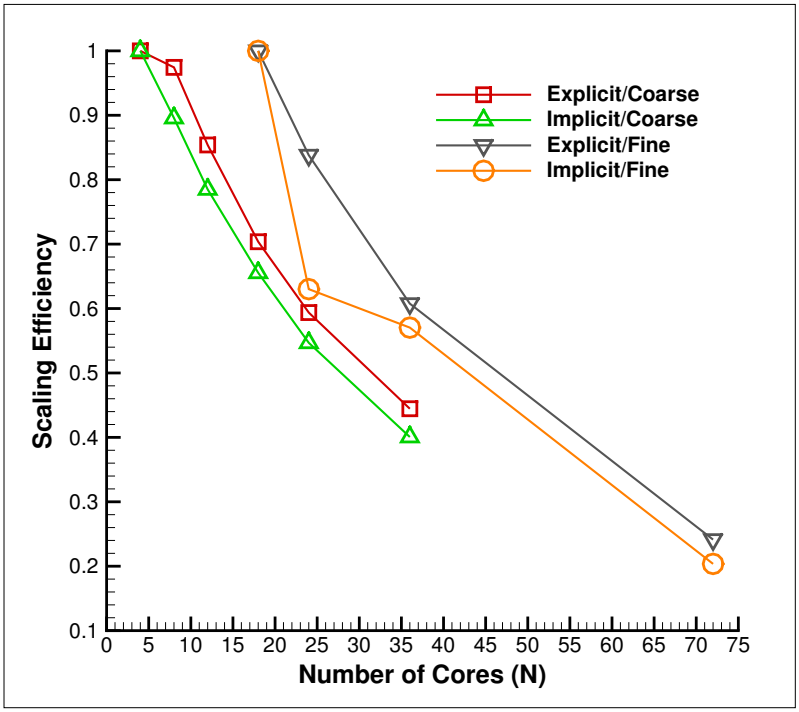

Figure 3.3: Single node strong scaling efficiency

Some of these performance issues should not be present for multi node simulations where MPI communication should be the major scaling bottleneck. The results presented in figure 3.4 for multi node strong scaling performance, shows excellent parallel strong scaling at high core count. Each cluster node for this study contains 16 cores and the baseline simulation uses 2 nodes i.e. 32 cores, rest of the simulations cases use 128, 192, 304, 394, 512, 768, 1024 cores. The simulated case consists of three dimensional GEC reference cell mesh containing 95539200 hexahedral block structured cells. The ideal strong scaling corresponds to decrease in computational time in proportion with increase in processing power. The strong scaling results show

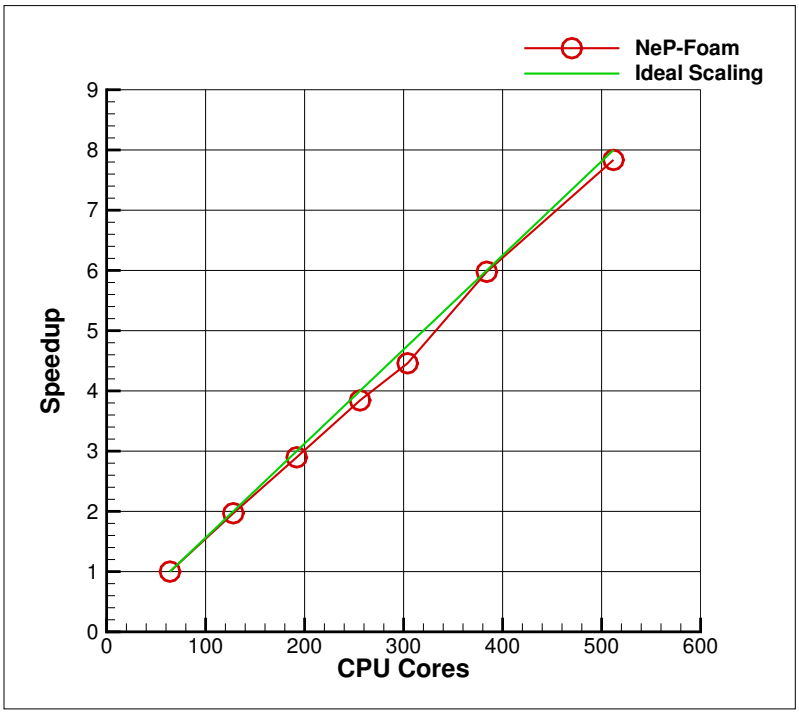

Figure 3.4: Strong scaling

perfect scaling to a very high processor count. Although we expect this behavior to be present outside upper and lower bounds of mesh cells and at larger core count, we have not performed any other study.

The weak scaling provides more general purpose metric for choice of parallel resources for simulations. It presents an aspect of limits of parallel computing, usually opposite to unavoidable limits of strong scaling. Figure 3.5 shows weak scaling over multiple core count configuration. The weak scaling analysis was done on different set of compute nodes and mesh cells count, in succession of multiple of 2, to preserve cell count/core ratio. The case 1 & 2 are only different in mesh configuration, and consists of 1224400 and 62200 cell pre CPU core respectively. Case 1 baseline run starts at 16 cores and goes till 256 cores, whereas Case 2 is from 32 to 512 cores. The analysis show that up to 6 computational nodes, scaling is withing 15% limit of ideal scaling but at higher node count it drops as much as 30%. The shortcoming of weak scaling could be attributed to overhead of parallelization growing with problem size. Also the TSCC cluster contains mixed node configuration, based on a range of hardware with varying degree of performance. It is not always viable to make sure that our

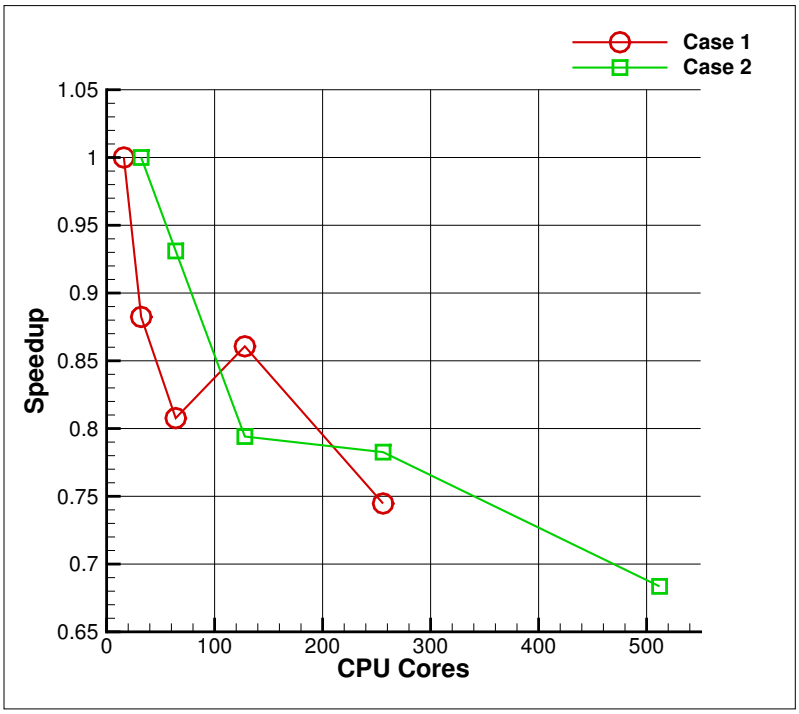

Figure 3.5: Weak scaling

simulations run on nodes containing same hardware altogether, to provide better load balancing and communication for optimal performance. The complexity of partition graph at large problem size also affect contention in network communications.

The plasma solver's performance assessment is hard due to inherent complexity associated with nature of plasma governing equations and associated multiphysics. As plasma specie, chemistry and electromagnetics may fall in different performance regime due to their unique numerical behavior, the choice of optimized algorithm and performance tools becomes critical for the scalable performance. This section attempts to provide a rough sketch of performance criteria associated to problem size and resources.

In summary, the current features of the toolbox can be summarized as follows:

- Support for transient, steady and pseudo-transient problems.
- Arbitrary 1D/2D/3D and axi-symmetric geometry with ability to handle complex geometry.

- Well-studied parallel processing and data I/O capabilities at all levels of code.
- Unstructured polyhedral mixed-mesh elements.
- A range of established plasma and electromagnetic boundary conditions available in literature.
- Arbitrary number of plasma and gas species and their mixture properties.
- A range of reaction types including elastic, inelastic, Arrhenius rate constant based on species temperature and/or any other plasma variables etc..
- A suitable interface for I/O or coupled multiphysics with other solvers.
- A general-purpose implementation and support for electromagnetic simulations, plasma or coupled plasma-dielectric multi-region.

3.3 Results and Discussion

To demonstrate some of the capabilities of the code, we verify and validate the results obtained using the code by comparing with established benchmark results for low temperature plasma problems. Later, we present representative simulations performed using SOMAFOAM to demonstrate its features. The problems simulated here include a wide range of operating conditions for pressure and excitation frequency thereby demonstrating the versatility of the framework.

Low-pressure radio frequency plasma

The first validation case is for code-to-code validation where capacitively coupled plasma simulation results are analyzed based on established fluid model and particle methods results. GEC reference cell experimental data is then studied for experimental validation of solver in order to illustrate solver's capability to handle complex simulation requirements of plasma applications design. For these tests, our results have been compared for most relevant physical and numerical parameters. Further, the validation problems are chosen to be ccp system operating at rf voltages. We argue that these systems are less sensitive to the surface interaction, show linear behavior over large range and relatively well understood in terms of plasma chemistry and power dynamics etc. to facilitate verification and validation of our framework. Further in result section, we show more capabilities of framework which could be used to simulate plasma sources other than ccp.

In order to evaluate the implementation of plasma fluid equations in our code, we use the benchmark simulation results proposed by Turner et. al [88]. It should be mentioned that this benchmarking utilizes the experimental data of Godyak et al. [25]. The benchmark problem simulates a one dimensional discharge between two plane-parallel electrodes, excited by a sinusoidally varying voltage difference. The benchmark conditions included are simulated by the particle-in-cell with Monte Carlo collisions (PIC-MCC) method which is considered to provide the most accurate description of the plasma at these operating conditions. The benchmark results included in the work [88], were produced with a verification and validation framework using independently developed PIC-MCC codes whose results were shown to have bounded uncertainty for a range of conditions. Also a set of solutions for moment based models (fluid models) are provided in [88] for comparison. Our focus for this validation is to evaluate the performance of our code by comparing with these published benchmark results. While comparing fluid models with PIC-MCC simulations, one should note that these two simulation methods will seldom lead to exact agreement due to underlying differences in the building blocks of the two models that are briefly discussed in [49]. However, PIC-MCC simulations provide an excellent reference for comparing the results obtained using our code.

The benchmark case simulates a Helium plasma with electron and Helium monomer ions being the only species included in the simulation (in order to match with the PIC-MCC simulations). A wide range of gas pressures ($30 - 1000\, mTorr$) was considered with the gas temperature fixed at $300\, K$. The voltage amplitude was chosen such that the resulting current density amplitude was $\sim 10\ Am^{-2}$ (since the PIC-MCC simulations were performed in constant current mode). It should be noted that our code has the capability to perform constant voltage and constant power simulations and therefore we chose to vary the voltage amplitude until the desired current density was obtained. The test physical conditions are described in Table 3.1.

Parameters/Case #	1	2	3	4
Electrode Gap (cm)		6.7		
Gas Pressure (Torr)	0.03	0.1	0.3	1
Gas Temperature (K)		300		
Frequency (MHz)		13.56		
Voltage (V)	450	200	150	120

Table 3.1: Validation cases derived from CCP benchmark simulations in Turner et al.[88]

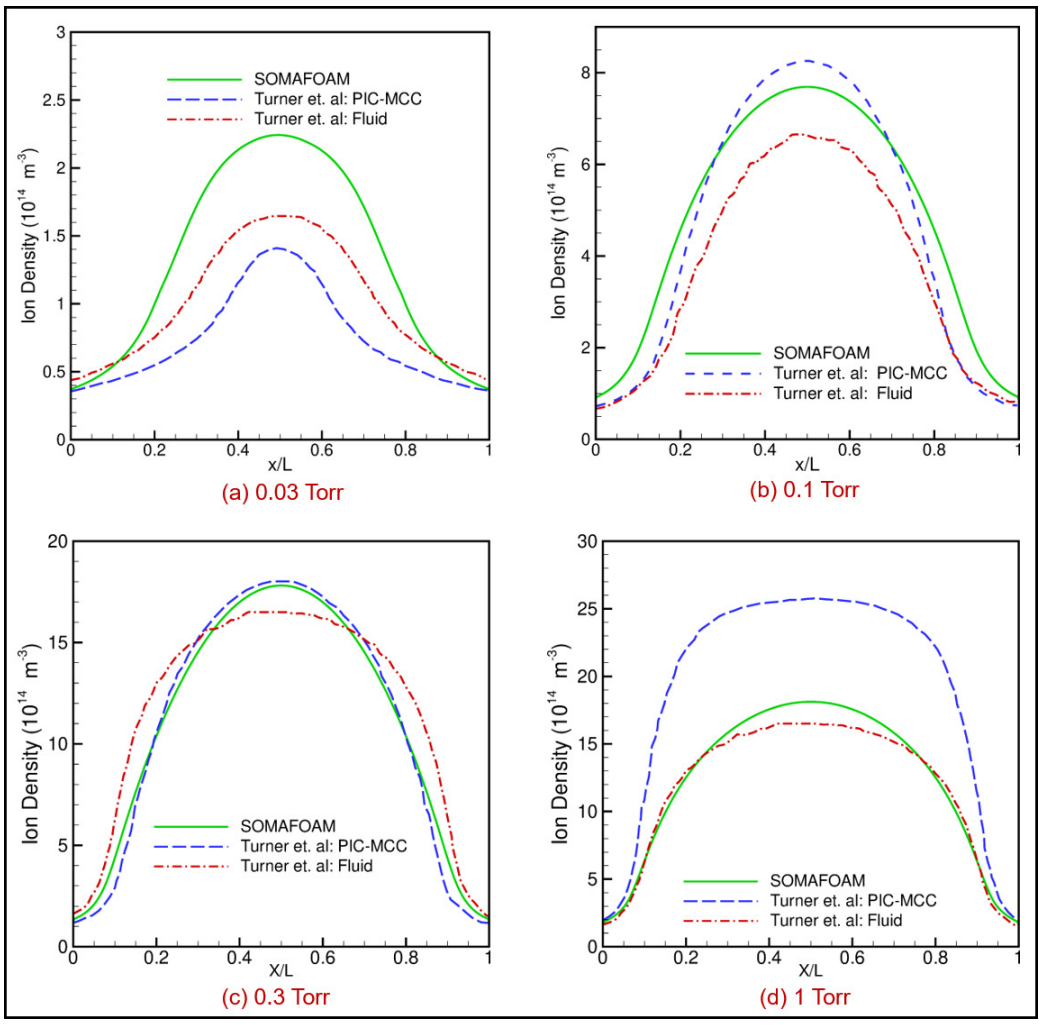

Figure 3.6: Comparison of ion number density profiles obtained using SOMAFOAM simulations with kinetic and continuum simulations of Turner et al. [88]

The fluid simulation for the validation employs numerical parameters similar to those utilized by Turner et al. [88], whenever possible. It should be mentioned that fluid simulations require a large number of input parameters with most of them not being explicitly provided in plasma literature. Thus, one has to make a number of suitable choices when it comes to numerical implementation and parameters, to account for the missing information. In our fluid model, we employed a traditional drift-diffusion approximation for charged species continuity equation alongside the

electron energy equation. The Poisson's equation with a linearized source term [3] was used to obtain the self-consistent electric field. The mobility data for electrons and helium ions are assumed to depend on the local reduced electric field, and are obtained from BOLSIG+ [29] and drift tube experiments [5] respectively. Diffusion coefficients for both species are calculated using the Einstein's relation.

Here, we compare results obtained using our code with PIC-MCC and fluid model results from Turner et. al [88], for cycle-averaged plasma parameters once the simulation reaches a periodic steady state. Figure 3.6 shows the results for Argon ion number density compared with benchmark results for case 2 from Table 3.1. It can be seen that results obtained in this work agree well with the PIC-MCC simulations. In fact our fluid model, seems to perform better than the fluid model results shown by Turner et al. [88]. The differences in results obtained using the two fluid simulations can be attributed to differences in some of the input parameters with our choice leading to better agreement for the peak number density at the chosen conditions. However, the same set of input parameters lead to significant differences at other operating conditions as seen in Figure 3.6. In particular, the intermediate pressures (Case 2 and Case 3) lead to good agreement between fluid and kinetic simulations whereas discrepancies appear at both low and high pressures. In spite of these discrepancies, these simulations certainly serve our current purpose which is to validate the fluid code with kinetic simulations. The results obtained from SOMAFOAM simulations are also comparable with the fluid simulations reported by Turner et al. [88] which employed the plasma module in COMSOL to perform the simulations. It should be noted that an exact match is hard to expect (even though both results utilize the same modeling approach) due to potential differences in the physical parameters. In this case, we attribute the small discrepancies to differences in the diffusion constant (the values of which are not explicitly reported by Turner et al. [88]). This is also consistent with the observation that the discrepancies between SOMAFOAM and Turner et al [88] decrease with increasing pressure. We conclude this study by emphasizing that the good overall agreement with kinetic simulations serves as a validation case for the SOMAFOAM code. A more detailed study explaining the factors contributing to the observed discrepancy is beyond the scope of the work but is likely due to fundamental differences in the electron energy distribution function.

Capacitively Coupled GEC Reference Cell

The Gaseous Electronics Conference (GEC) reference cell is a common standard for plasma experiment and modeling among researchers around the world [30]. It is conceived as a well defined plasma reactor that either operates in CCP or inductively coupled plasma (ICP) mode that could be used for benchmarking of plasma simu-

lations. Over years, numerous studies have been performed to validate and analyze GEC reference cell fluid simulation results [63, 7, 53]. Considering the complex nature of low temperature plasma and high sensitivity of reference parameters, both in experiment and numerical modeling, a well characterized system such as GEC reference cell, is still a classical benchmark problem.

In this validation, we focus on experimental measurements done by Overzet et al. [71, 70]. The capacitively coupled GEC reference cell geometry is same as that described in [63]. The simulations are performed for an axisymmetric configuration to account for the cylindrical symmetry of the GEC reference cell. The plasma-dielectric electrostatic solution was achieved by a coupled formulation of the Poisson's equation as implemented in the SOMAFOAM code. We consider argon plasma ignited in the GEC reference cell at varying pressures between $0.1 - 1\ Torr$ and at 300 K gas temperature. The plasma consists of electron(e^-), argon ion(Ar^+) and excited argon atoms (Ar^*) as active constituents with neutral Argon as background gas. The set of reactions included in this study are listed in Table 3.2.

#	Process	Reaction	Ref.
1	Elastic scattering	$e^- + Ar \rightarrow Ar + e^-$	[29]
2	Ionization	$e^- + Ar \rightarrow Ar^+ + 2e^-$	[29]
3	Metastable excitation	$e^- + Ar \rightarrow Ar^* + e^-$	[29]
4	Multi-step ionization	$e^- + Ar^* \rightarrow Ar^+ + 2e^-$	[29]
5	Multi-step ionization	$2e^- + Ar^+ \rightarrow Ar^* + e^-$	[28]
6	Multi-step ionization	$e^- + Ar^* \rightarrow Ar + e^-$	[28]
7	Inelastic metastable production	$e^- + Ar^+ \rightarrow Ar^*$	[28]
8	Metastable pooling	$Ar^* + Ar^* \rightarrow Ar + Ar^+ + e^-$	[28]
9	Radiation decay	$Ar^* \rightarrow Ar$	[28]
10	Inelastic depletion	$Ar^* + Ar \rightarrow 2Ar$	[28]

Table 3.2: List of reactions considered for the GEC reference cell simulation of an argon plasma at various pressures.

The plasma species solution is based on the drift-diffusion approximation with coupling to Poisson's equation. The temporal discretization for all equations was done using the first order implicit Euler method. Second order central differencing was utilized for spatial discretization. Convective terms in plasma species and electron energy equation were discretized using Sweby [86] and Vanleer [6] limiters respectively. It should be reiterated that the SOMAFOAM code uses the underlying

OpenFOAM framework to choose from a wide range of discretization schemes for spatial discretization. The resultant matrix system was solved using a BICGStab solver with simplified diagonal based incomplete LU preconditioner. The Poisson's equation solution matrix was solved in coupled formulation using the BICGStab method with the Cholesky preconditioner. The axisymmetric mesh (not shown) contains between 19050 and 26580 block structured mesh cells for the plasma region. The transport coefficients were obtained from same sources as described in Section 3.3. Argon metastable diffusion coefficient was obtained from literature[7]. Both simulations reported here were performed with a DC bias of -81 V and an excitation frequency of 13.56 MHz. The peak voltages for the two cases were different.

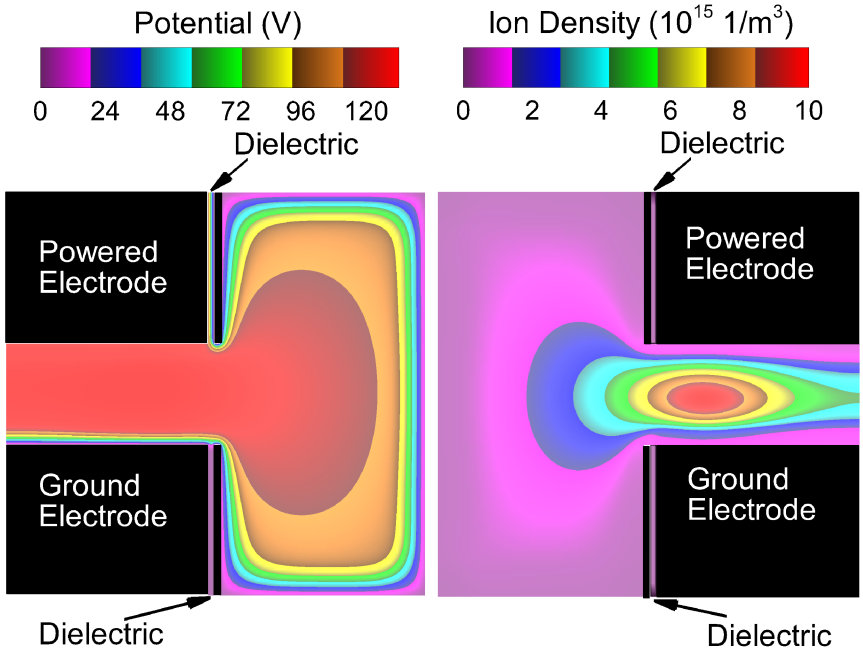

Figure 3.7: GEC reference cell operating at $100\,mTorr$ and $400\,V$ peak-to-peak voltage. Results shown correspond to end of the sinusoidal cycle. The potential (V) is shown on the left and Ar^+ ion density (m^{-3}) is shown on the right.

Figure 3.7 shows contours of potential and ion density for the GEC reference cell operating at $100\,mTorr$ and $400\,V$ peak-to-peak voltage. The ion density reaches its

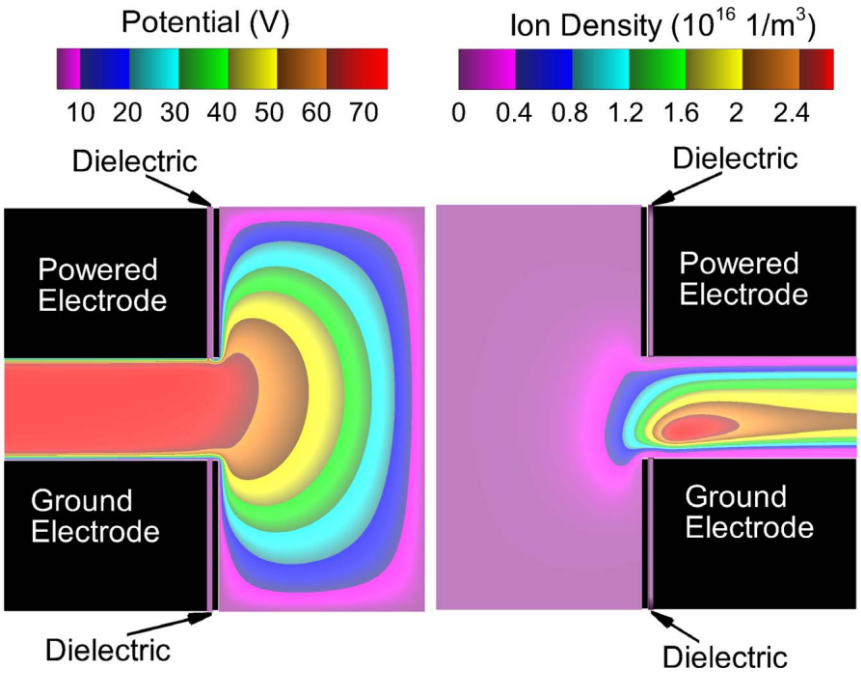

Figure 3.8: GEC reference cell operating at $1\,Torr$ and $200\,V$ peak-to-peak voltage. Rest of the details are same as figure 3.7.

maximum value of about 10^{16} 1/m^3 at the mid-point of the gap between the powered and ground electrodes as would be expected for a low-pressure discharge where the species diffusion coefficients are large. On the other hand, when the pressure is increased by a factor of 10 (to 1 Torr) and the peak-to-peak voltage decreased to 200 V, the peak ion (plasma) density of about 2.5×10^{16} $1/m^3$ occurs closer to the ground electrode thereby demonstrating that the number density profile is not completely diffusion-limited and is asymmetric about the centerline. Figure 3.9 compares the radial ion number density profiles, at the centerline, obtained from SOMAFOAM simulations with those obtained from experiments for the GEC reference cell operating at 100 mTorr and 250 mTorr respectively. The peak-to-peak voltage was fixed at 200 V for both cases in order to enable comparison with previously published experimental data [70]. The overall agreement between experiments and SOMAFOAM simulations is qualitatively good with the peak ion number density and its radial location being predicted accurately. While the simulations do predict a more rapid decrease in the ion number density than in experiments, we consider this acceptable and the agreement could potentially be improved by fine-tuning various input parameters

including mobility and diffusion coefficients.

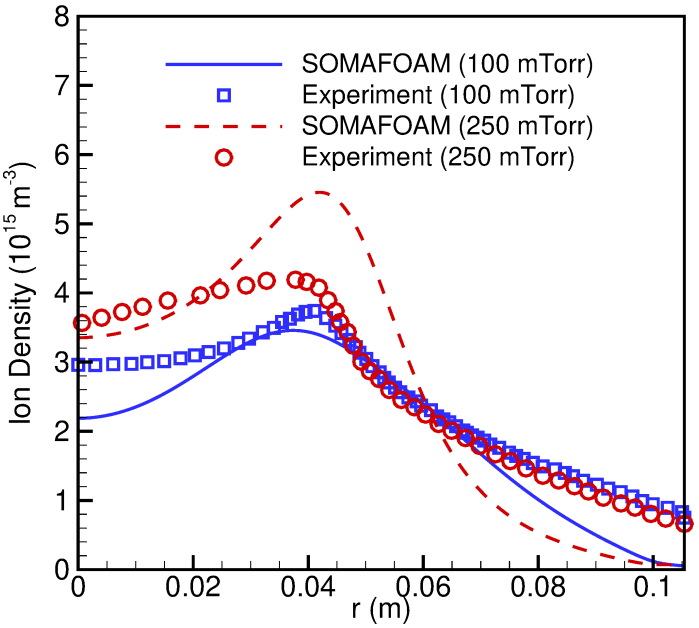

Figure 3.9: Comparison of radial Ar^+ ion density (m^{-3}) profiles (at the centerline) obtained from SOMAFOAM simulations and experiments.

Direct Current Plasma

SOMAFOAM was also used to simulate argon direct current (DC) plasmas for a one-dimensional planar geometry as well as two-dimensional device with straight and curved dielectric boundaries to demonstrate representative features of the computational framework.

Low pressure

In this section, we consider a one dimensional direct current low pressure glow discharge that was also simulated by Deconinck et. al [17]. In their set-up, a glow discharge is ignited by applying a constant voltage difference of 250 V between electrodes that are 1 cm apart and filled with argon gas at 1 Torr. The simulations were performed by including two active species (Ar^+ ions and electrons). The species

continuity equation for ions and electrons was solved in conjunction with the drift-diffusion approximation. For simplicity, it is assumed that the plasma chemistry comprises of only the electron impact ionization reaction. The reaction rate coefficients and electron transport coefficients were tabulated as a function of electron mean energy and reduced electric field (E/N) respectively. These parameters were obtained using BOLSIG+ [29] with the standard set of reaction cross sections. Ion transport coefficients were obtained from available experimental data [19]. The secondary electron emission coefficient was set to 0.05. The computational domain was divided into 250 cells that were generated using the `blockMesh` utility.

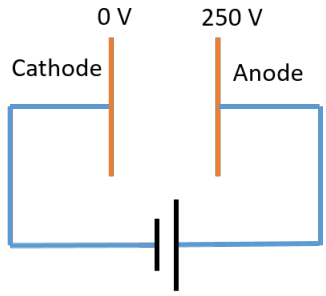

Figure 3.10: One dimensional direct current plasma arrangement

Figure 3.11 compares the steady state results for the electron/ion densities, electron temperature and potential profiles obtained from SOMAFOAM with the results presented by Deconinck et al. [17]. In spite of minor differences in the profiles, the results are in good overall agreement. Once again, the discrepancies could be attributed to potentially small differences in the physical/numerical parameters used. The sheath represents about 20 % of the gap size in both simulations with a peak number density of about 1.5×10^{16} $1/\mathrm{m}^3$. The maximum electron temperature of about 28 eV occurs in the sheath with the quasi-neutral region electron temperature computed as 5 eV which is consistent across both the simulations.

High pressure

After the verification of the low-pressure DC plasma simulation, we used SOMAFOAM to simulate a two-dimensional high pressure direct current microdischarge bounded by dielectric regions. In order to demonstrate the capabilities of SOMAFOAM, we report simulations where the plasma-dielectric is curved. Figure 3.12 shows the mesh used for the curved interface simulation along with an inset showing a zoomed in version

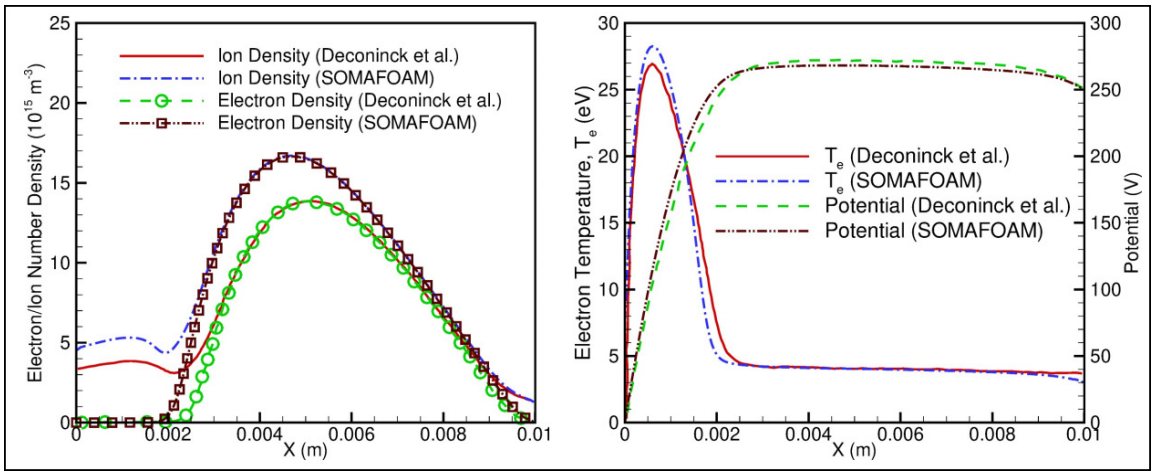

Figure 3.11: Comparison of electron/ion number density, potential and electron temperature profiles obtained using SOMAFOAM with the results presented by Deconinck et al. [17] for a low pressure argon direct current plasma.

of the mesh in a certain region close to the plasma-dielectric interface. The distance between the electrodes was set as 200 μm and the width of the plasma cell varies from 200 μm at the electrodes to 240 μm at the centerline between the electrodes. The gas pressure was fixed at 300 Torr thereby resulting in a relatively high pd value of 6 $Torr - cm$. The mesh was constructed using an open source three-dimensional finite element mesh generation utility, Gmsh [24]. The plasma region was decomposed into of $34,896$ hexahedral unstructured cells and the dielectric section consisted of $14,602$ structured hexahedral curved mesh elements. The cell size in the plasma region varied between 0.8 μm to 1.4 μm. The plasma-dielectric curved interface contained conforming mesh elements for efficient solution on the curved surface.

Even though the authors acknowledge the over-simplified chemistry considered for the low-pressure plasma simulated earlier, we use the same chemistry here for simplicity. This does not affect the objective of these simulations which is to demonstrate the capability of the solver to deal with devices comprising of both plasma and dielectric regions as well as the ability to deal with curved surfaces as part of the geometry. The electron transport parameters (mobility, diffusion) were obtained as a function of reduced electric field (E/N) using BOLSIG+ [29]. The reaction rate coefficient for the ionization reaction was obtained by assuming that the electron energy distribution function (EEDF) was a Maxwellian distribution function. While this may seem incorrect in a non-equilibrium low-temperature plasma, it was demonstrated

by Verma et al. [91, 92] that the rate coefficients obtained from kinetic simulations showed better agreement with reaction rate coefficients that were obtained using a Maxwellian EEDF than those obtained using a non-Maxwellian EEDF provided by the two-term approximation in BOLSIG+. The secondary electron coefficient was set to 0.05. A potential of 250 V was applied to the bottom electrode while the top electrode was grounded.

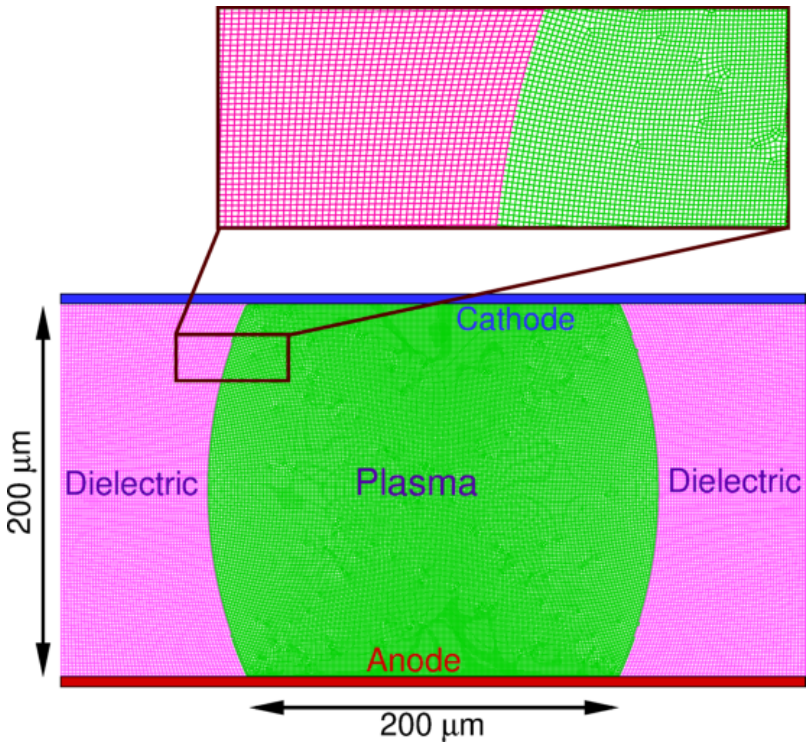

Figure 3.12: A schematic of the plasma with curved dielectric sidewalls. The hybrid mesh used for the simulations is also shown

Figure 3.13 shows contours of the electron and argon ion number density at steady state with a peak density of about 1.5×10^{20} m^{-3}, that is typical for high pressure microdischarges. The results indicate the presence of a sharp local maximum in the density profiles which is typical of high-pressure microdischarges where the ions and electrons do not diffuse significantly. The curved sidewalls allow some room for the plasma to expand and can be confirmed by the small lobes in the ion number density. Figure 3.14 shows contours of electron temperature and potential. While the electron temperature is only relevant to the plasma region, the potential is shown for

both plasma and dielectric regions. The electron temperature peaks at about 10 eV at a location in the sheath (as was the case for the low-pressure plasma) with an electron temperature between 3 and 4 eV in the quasi-neutral region. The contours also show the presence of sheath regions (with higher electron temperature) near the plasma-dielectric interface. Figure 3.15 shows contours of the the electric field components (E_x and E_y) in the plasma and dielectric regions where the sheath-like region shown by the electron temperature contours is characterized by high electric fields pointing towards the surface (analogous to the sheath region near the cathode). The plasma-dielectric interface near the anode encounters much smaller electric fields. The plasma-dielectric interface also shows a discontinuity in the electric field due to the surface charge that accumulates on the surface of the dielectric.

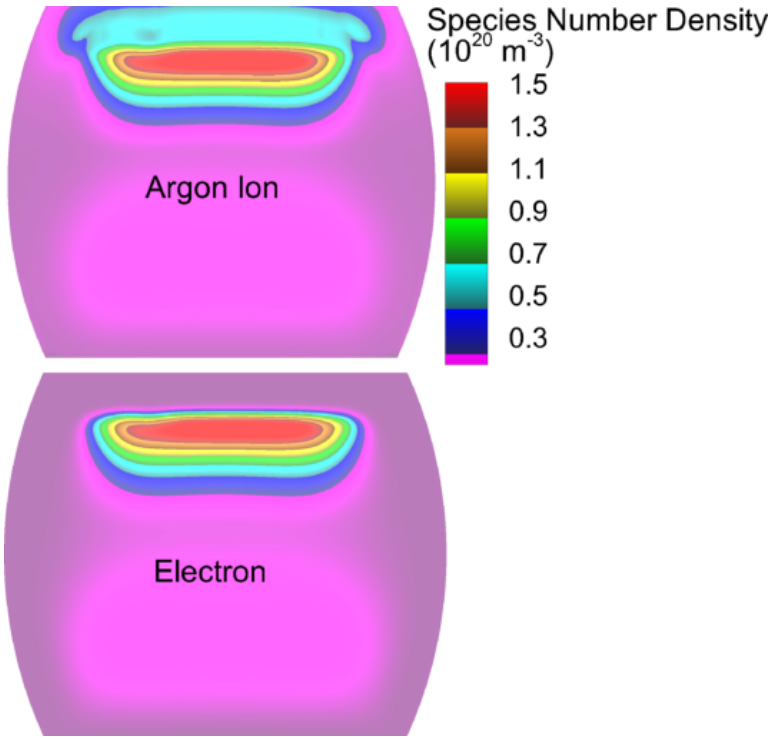

Figure 3.13: Contours of argon ion and electron number density obtained using SOMAFOAM for a high-pressure glow discharge containing a curved plasma-dielectric interface. Only the plasma region is shown in the figure.

In order to compare and contrast the influence of the curved plasma-dielectric interface, we also performed simulations where the plasma-dielectric interface is vertical.

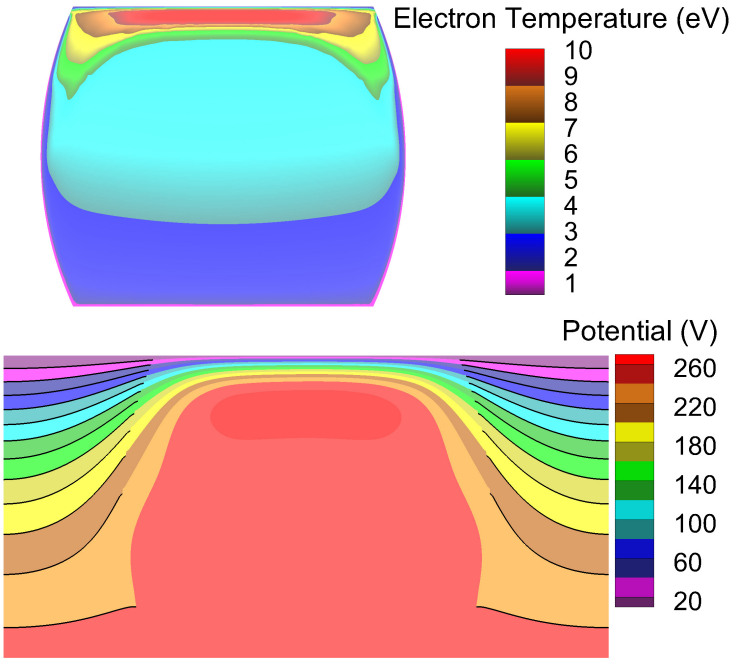

Figure 3.14: Contours of electron temperature and potential obtained using SOMAFOAM for a high-pressure glow discharge containing a curved plasma-dielectric interface. While the electron temperature is only relevant to the plasma region, the potential is shown in both plasma and dielectric regions. The contours in the dielectric region include both lines and colors while the plasma region contours only have color.

To reiterate, the plasma region in this case is a 200 μm square and is coupled with the rectangular dielectric region on both sides. The width of the dielectric region on each side is 100 μm. The plasma region is discretized using 60,000 structured cells and the dielectric region has a total of 9,000 high apect ratio structured cells and is mapped conformally with the plasma mesh. Other simulation parameters are same as for the curved plasma-dielectric simulation reported above. Figure 3.16 shows contours of electron number density and temperature for the vertical plasma-dielectric interface for comparison with the curved plasma-dielectric interface case. Even though the peak number density at about $1.1\times\ 10^20$ m$^-3$ is a little lower, the variation of the electron number density is more gradual than the curved plasma-dielectric case.

It can be seen the curvature of plasma-dielectric interface has significant effect

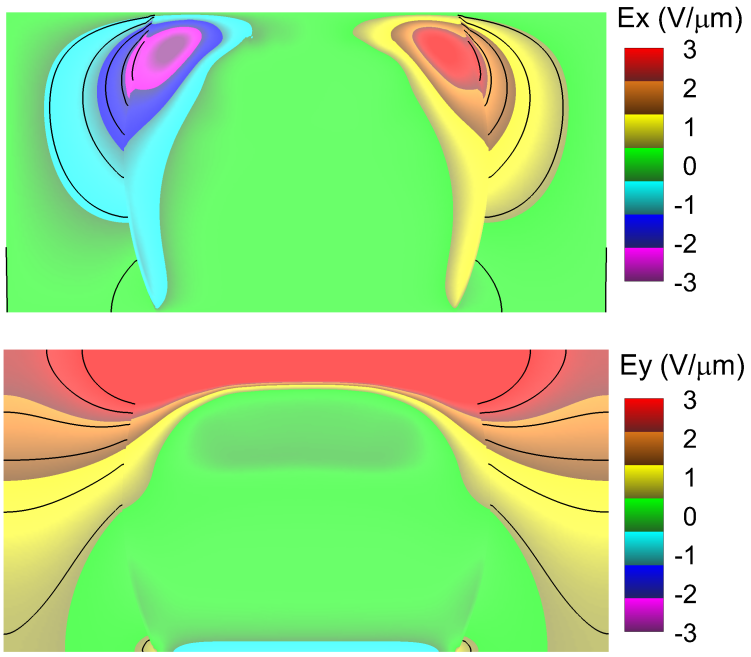

Figure 3.15: Contours of x and y components of the electric field obtained using SOMAFOAM for a high-pressure glow discharge containing a curved plasma-dielectric interface. The contours in the dielectric region include both lines and colors while the plasma region contours only have color.

on the plasma dynamics. The constant potential contour lines are more stretched backwards due to significant effect of dielectric surface. The electron dynamics shows similar tendency where the density contour has more charge in the center region due to higher secondary electron emission from dielectric surface.

For further clarity on the effect of dielectric shape on charge dynamics, one dimensional simulation was performed to establish role of dielectric. The infinitely long, parallel electrodes are placed at a gap of 200 μm is discretize with 300 cells. All the simulation details and numerics are retained the same except no dielectric is present. Figure 3.17 shows comparison between all three simulations results. The results shown for two dimensional simulations, correspond to probe at the axis vertical to electrodes, placed at the center. The results shows clear indication that the curved interface behave closer to one dimensional electrodes configuration, whereas straight wall configuration has significant effect on the plasma. This shows a complex nature

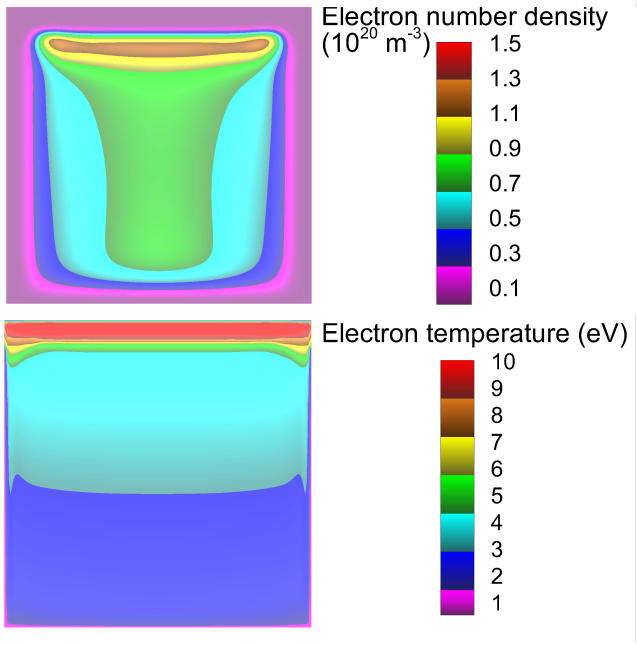

Figure 3.16: Contours of electron number density and electron temperature obtained using SOMAFOAM for a high-pressure glow discharge containing a vertical plasma-dielectric interface. The contours in the dielectric region include both lines and colors while the plasma region contours only have color.

of plasma-dielectric interface topology and further study can exoand to a detailed analysis of topological effects of confined low temperature plasma sources.

Microwave MicroPlasmas

With the presentation of direct current and radio frequency plasmas in the previous sections, we expand our study to microwave microplasmas in this section. Specifically, we present representative results for a microwave microplasma ignited in a split ring resonator (SRR). SRRs have become established as an efficient plasma source with several experimental studies dedicated to their operation [39, 35, 38, 80]. While computational studies have been reported for microwave microplasmas, they have been restricted to one-dimensional simulations or have dealt only with the lower frequencies (1 GHz) in the microwave spectrum. In this study, we have performed two dimensional simulations of a microplasma ignited in an SRR operating at atmospheric pressure with a resonant frequency of 8.7 GHz. The choice of the frequency

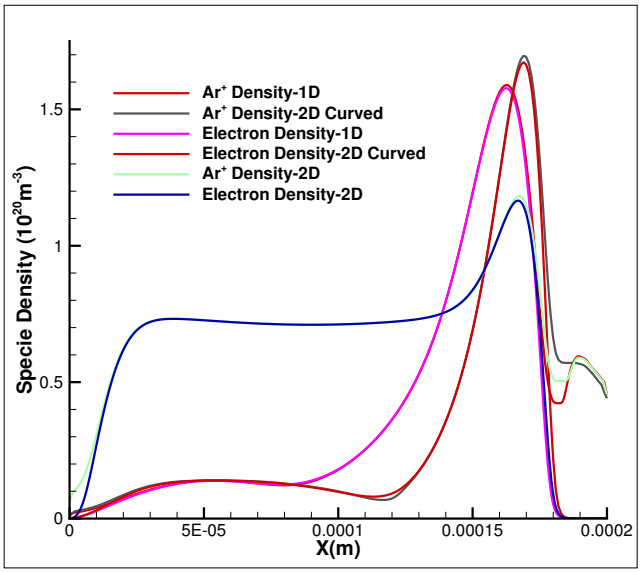

Figure 3.17: Plasma specie number density (m^{-3}) for high pressure glow discharge. The 1D data for 2D simulations shown here, corresponds to probe at center axis between electrodes.

is based on the availability of experimental data thereby enabling direct comparison with experiments. Figure 3.18 shows a schematic of the simulation set-up and the mesh used to discretize the computational domain. The gap between the powered and ground electrodes was set as 100 μm with the thickness fixed at 35 μm. The dielectric thickness was taken to be 2.54 mm and was grounded at the bottom. The simulations presented here were power-controlled and the depth of the geometry (in the third dimension) was fixed at 65 μm and is required to compute the total power deposited. It should be emphasized that the geometrical and plasma parameters were derived from the experimental work done of Hoskinson et. al [35]. The unstructured hexahedral dominated mesh contains 64,333 cells in the plasma region and 3,062 cells in the dielectric region. As in the case of other two-dimensional simulations, the mesh was generated using Gmsh [24] with a combination of hexahedral and pyramidal elements. The mesh was refined in the proximity of the electrode gap for both plasma and dielectric regions in order to resolve the relevant physics in the gap. The size of the plasma domain was chosen to be large enough (4 mm $\times$ 2 mm) so that the open boundaries do not affect the plasma dynamics in the gap.

The microplasma simulation consists of three active species including electrons,

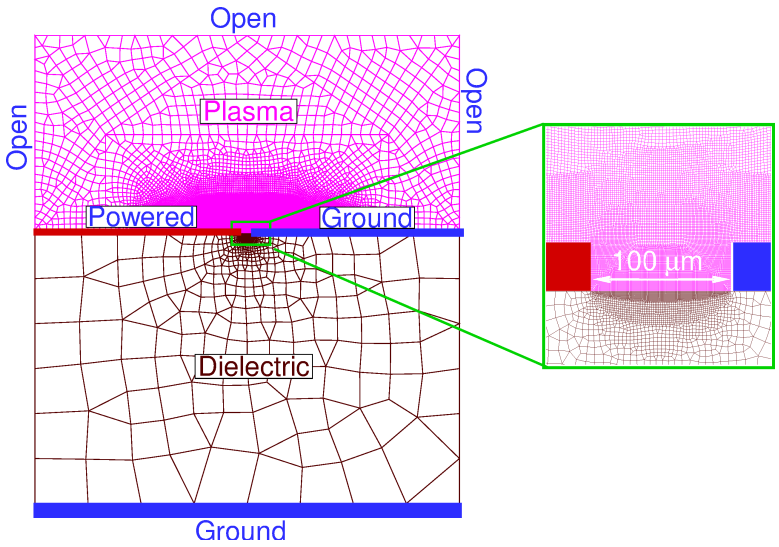

Figure 3.18: A schematic of the simulation set-up used for the microwave microplasma ignited in a split ring resonator. Also shown is the mesh used to discretize the computational domain in the plasma and dielectric.

argon ions and argon metastables. The reaction set and transport coefficients for this study is same as that used for the GEC reference cell simulations. The simulations included the continuity equation solution for all species, full-momentum and energy equation for both charged species and the gas temperature equation for argon which is the background gas. The gas temperature equation's source terms were calculated by time-averaging the plasma parameters over an entire cycle and the gas temperature solution was obtained once during each cycle. Poisson's equation was solved for both plasma and dielectric regions with suitable coupling. Sub-cycling was used for electron continuity and momentum equation such that the time step for these equations is 100 times smaller than the rest of the system (another useful feature of SOMAFOAM). The simulations were power-controlled where the voltage amplitude of the powered electrode was modified until the specified power was achieved. The power input to the plasma was computed by performing a volume integral of the $\mathbf{j} \cdot \mathbf{E}$ term in the entire computational domain. Figure 3.19 shows contours of electron number density and gas temperature both of which can be compared with available experimental data. The peak electron number density predicted from the simulations is about 4×10^{20} m^{-3} and agrees well with the peak electron number density reported by Hoskinson et al. [35]. While gas temperature measurements were not reported for the 8.7 GHz

case, Hoskinson et al. [36] measured gas temperatures for microwave microplasmas at frequencies 2 GHz, 3 GHz and 12 GHz with reported peak values between 800 K and 1000 K. The peak gas temperature of about 1200 K obtained from SOMAFOAM simulations is a little more than the values reported by Hoskinson et al. [36]. To the best of our knowledge, this is the first direct comparison between simulations and experiments for microwave microplasmas ignited in split ring resonators. While three-dimensional simulations are certainly more appropriate and may lead to better agreement, this case represents a suitable validation for SOMAFOAM at microwave frequencies.

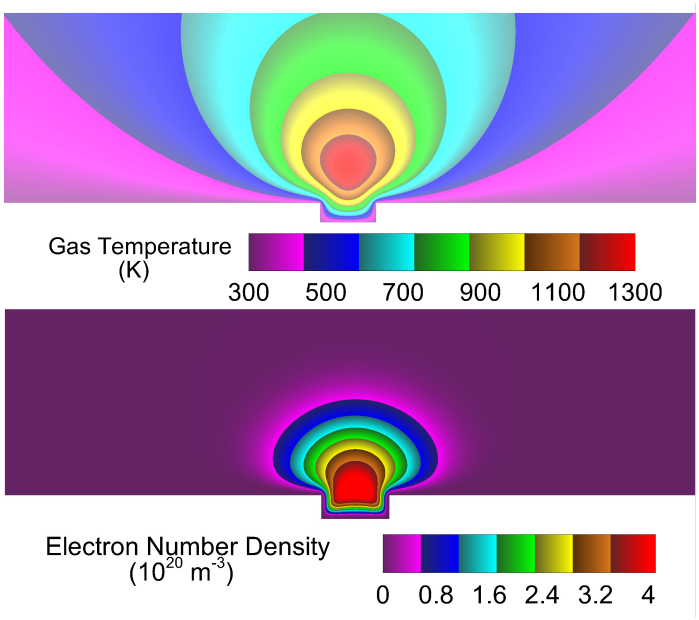

Figure 3.19: Contours of time-averaged electron number density and gas temperature for an atmospherice pressure microwave microplasma ignited using 20 mW of power at 8.7 GHz. The figure does not show the entire computational domain. Only the region close to the electrodes is shown for clarity.

Dielectric barrier discharge plasma

The final case considered to demonstrate the features and capabilities of SOMAFOAM is a dielectric barrier discharge (DBD) plasma. While simulations with the presence of the dielectric were considered earlier in the case of the GEC reference cell and the

direct current plasma bounded by a dielectric, the dielectric region did not play an active role in the plasma dynamics since it was not sandwiched between the powered electrode and the plasma. DBD plasmas are characterized by the presence of a dielectric between the powered and ground electrode and therefore have unique properties that are often of interest to a variety of applications including the rapidly growing area of plasma medicine, plasma-surface modification, nanomaterial synthesis, and greenhouse gas conversion to name a few. Dielectric barrier discharge plasma is an important plasma source from the perspective of engineering applications. A more detailed description of DBD plasmas and their characteristics can be found elsewhere [9].

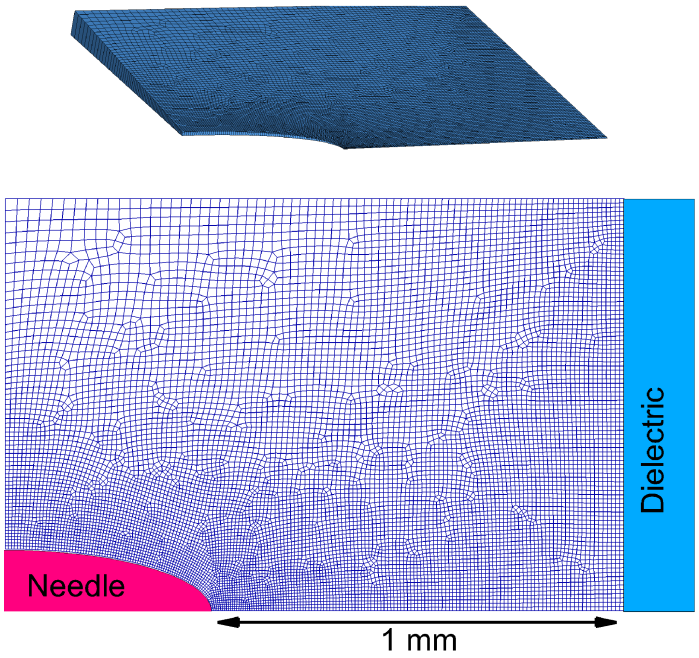

Figure 3.20: The axi-symmetric mixed-element computational mesh used for the atmospheric-pressure needle DBD plasma. The dielectric block is only shown partially in the figure. The wedge angle required for axi-symmetric simulations in OpenFOAM is depicted in the inset

In order to use SOMAFOAM to simulate a DBD plasma, we consider a DBD plasma ignited using a needle electrode. Such a set-up is of relevance to plasma medicine and also has prior simulations for comparison, for example by Sakiyama et

al. [77, 78]. The plasma needle is immensely successful in many scientific applications related to surface treatment [84, 83, 81]. As pointed in [9], barrier discharges operating at high frequency are functioning mostly in α mode (contrary to γ mode contributing to self pulsating behavior present at low frequency) and work as a protection for electrode material from plasma species or surface modification.

#	Process	Reaction	Ref.
1	Elastic scattering	$e^- + He \rightarrow He + e^-$	[29]
2	Ionization	$e^- + He \rightarrow He^+ + 2e^-$	[29]
3	Metastable excitation	$e^- + He \rightarrow He^* + e^-$	[29]
4	Multi-step ionization	$e^- + He^* \rightarrow He^+ + 2e^-$	[29]
5	Dissociative recombination	$e^- + He_2^+ \rightarrow He^* + He$	[10]
6	Dissociative recombination	$e^- + N_2^+ \rightarrow N_2$	[10]
7	Dissociative recombination	$e^- + N_4^+ \rightarrow 2N_2$	[66]
8	He_2^+ ion recharge	$He_2^+ + N_2 \rightarrow N_2^+ + He_2^*$	[10]
9	N_2^+ conversion	$N_2^+ + 2N_2 \rightarrow N_4^+ + N_2$	[66]
10	N_2^+ conversion	$N_2^+ + N_2 + He \rightarrow N_4^+ + He$	[66]
11	He^+ conversion	$He^+ + 2He \rightarrow He_2^+ + He$	[10]
12	N_4^+ conversion	$N_4^+ + N_2 \rightarrow N_2^+ + 2N_2$	[66]
13	N_4^+ conversion	$N_4^+ + He \rightarrow N_2^+ + N_2 + He$	[66]
14	Conversion of metastables	$He^* + 2He \rightarrow He_2^* + He$	[66]
15	Chemoionization	$2He^* \rightarrow He_2^+ + e^-$	[66]
16	Penning ionization	$He^* + N_2 \rightarrow N_2^+ + He + e^-$	[66]
17	Destruction of excimers	$He_2^* + M \rightarrow 2He + M$	[66]
18	Chemoionization	$2He_2^* \rightarrow He_2^+ + e^- + 2He$	[66]
19	Penning ionization	$He_2^* + N_2 \rightarrow N_2^+ + 2He + e^-$	[66]

Table 3.3: List of reactions considered for atmospheric pressure needle barrier discharge

A schematic of the simulation set-up and mesh (in the plasma region) are shown in Figure 3.20. The plasma needle barrier discharge is operating at atmospheric pressure and at a frequency of $13.56\,MHz$ thereby classifying it as a radio frequency (RF) plasma. The plasma needle tip surface is approximated as a prolate spheroid and the simulation was set-up as an axi-symmetric case in SOMAFOAM. The needle's major and minor axis radii are $500\,\mu m$ and $150\,\mu m$ respectively. The needle faces a dielectric surface with a relative permittivity of 5. The distance between the dielectric surface

and needle is 1 mm. The mesh consists of 11, 118 hexahedral dominated unstructured mixed-element cells generated using Gmsh [24]. The mesh elements are graded coarser away from needle tip to provide enough mesh resolution at the curved section that will encounter high electric fields. A self-bias voltage appears at the dielectric surface and is induced due to the asymmetric electrode and barrier configuration. The other side of the dielectric (not shown in figure) is grounded. The simulations are power-controlled by modifying the voltage amplitude at the needle based on the difference between the actual and desired power.

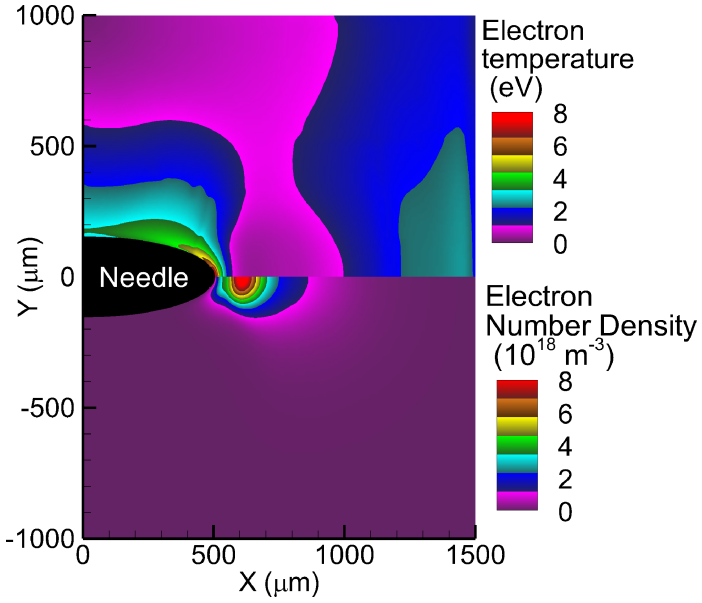

Figure 3.21: Contours of electron number density and electron temperature for a radio frequency (13.56 MHz) needle dielectric barrier discharge plasma ignited at 20 mW

The gap between the needle and dielectric surface is filled with helium and contains nitrogen as an impurity. The He:N_2 mole fraction is fixed at 10^6 : 1. In this study, seven charged and metastable species are used to describe the plasma including $e^-, He^+, He_2^+, He^*, He_2^*, N_2^+, N_4^+$. Table 3.3 lists the chemical reactions that were included in the simulation. As always, the transport coefficients for electron in the He-N_2 gas mixture were obtained from BOLSIG+ [29]. The Helium and Nitrogen ion and metastables transport coefficients are obtained from various experimental datasets available in literature [5, 77, 19].

The RF plasma was ignited at $20\,mW$ at atmospheric pressure and a fixed gas temperature of $300\,K$. The set of governing equations were solved as in the case of Sakiyama et al. [78] except that no ion energy equation was solved. Ions were assumed to be in thermodynamic equilibrium with the background gas and hence their temperature was assumed to be $300\,K$. The boundary conditions for species equations were based on expressions given by Lindsay et al. [61]. For the electron energy equation, a constant electron temperature of $1\,eV$ was used as boundary condition on all solid surfaces. A constant secondary electron emission coefficient of 0.25 was used for charged species of helium and a value of 0.1 was used for nitrogen.

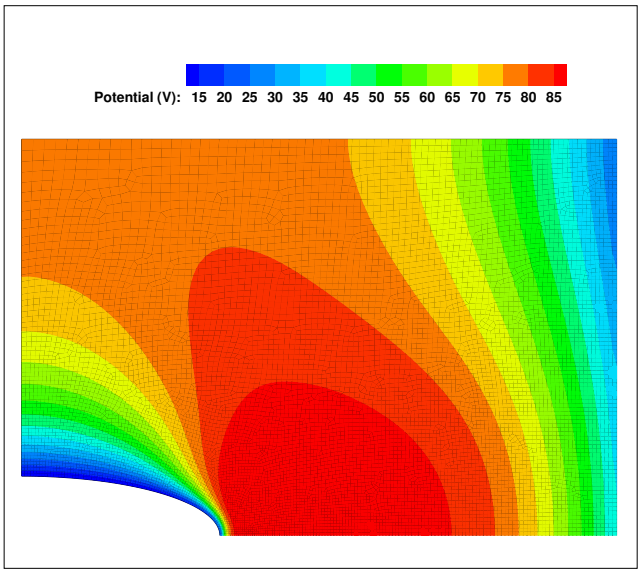

Figure 3.22: Cycle averaged electric potential (V) corresponding to atmospheric pressure rf needle barrier discharge in glow mode.

A simplified plasma-dielectric coupling was used for the solution of the Poisson's equation. The dielectric is assumed to have a uniform electric field normal to the surface, which is a valid assumption given the large size of the dielectric. To satisfy the electric field discontinuity condition at the dielectric surface, an approximated boundary condition expression for Poisson's equation was used and is given by

$$\epsilon_0 E_p - \epsilon_d E_d = \sigma_s \tag{3.2}$$

where E_d is the uniform normal component of electric field inside dielectric, ϵ_d is dielectric constant and E_p is surface normal electric field in plasma. The value of E_d

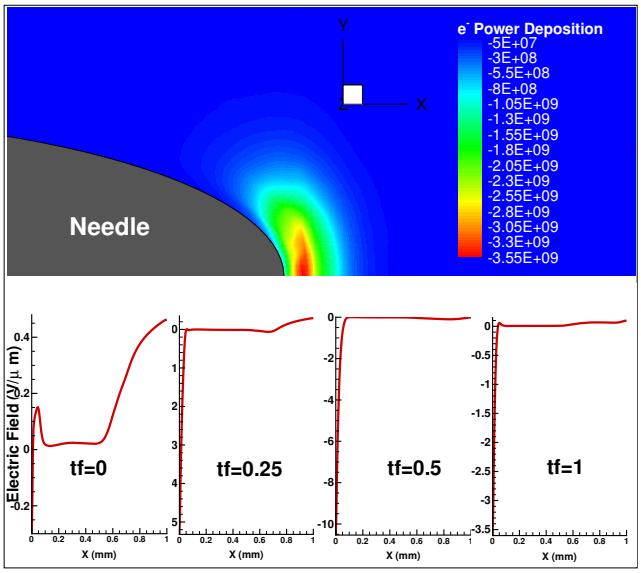

Figure 3.23: Cycle averaged electron power deposition (Wm^{-3}) (top) corresponding to atmospheric pressure rf needle barrier discharge in glow mode. The scalar sign value indicates power gain or loss. The electric field ($V\mu m^{-1}$) (bottom) at quarter cycle instances, probed at axis line between needle tip and dielectric.

was calculated from a simple one-dimensional approximation of the gradient expression and is given by $(-\Delta\Phi/\Delta x)$. The simulation results shown here correspond to a power deposition of $20\,mW$ with the corresponding voltage amplitude of $240\,V$ at converged periodic steady state. Figure 3.21 shows contours of time-averaged electron number density and electron temperature obtained from SOMAFOAM simulations. The electron density contours clearly show the sheath near the needle electrode with the density peaking at about 100 μm from the tip of the needle. The peak electron temperature is about 8 eV and is typical of RF plasmas operating in the α-mode. Figure 3.24 shows the spatial evolution of number density of all the charged species included in the simulation and could be qualitatively compared with the results published by Sakiyama et al. [78]. Even though the plasma operates at 100 mW in the simulations of Sakiyama et al. [78], the results are qualitatively similar. It can be seen that the bulk of the positive charge in the plasma is contributed by the He_2^+ ions. The time-averaged self-bias potential appearing at the dielectric surface was computed as 30 V (potential contours not shown here for brevity).

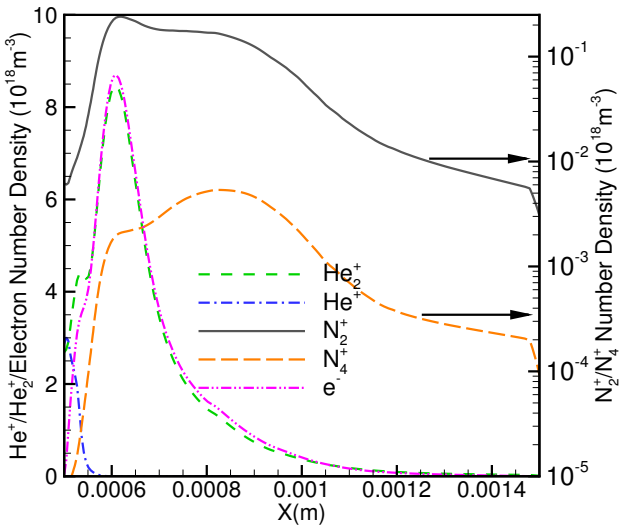

Figure 3.24: Axial profiles of charged species density in an atmospheric pressure RF needle dielectric barrier discharge plasma operating at 20 mW. The nitrogen species profiles are shown on a logarithmic scale.

Chapter 4

Modeling of Microplasmas

This study presents benchmark comparisons between continuum and kinetic simulations of argon microplasmas operating in the direct current and microwave regimes. Kinetic simulations using the particle-in-cell with Monte Carlo collisions (PIC-MCC) method and continuum simulations using the full-momentum equation for both ions and electrons are performed at various operating conditions in order to study the influence of product of pressure and gap size, pd (for a given gap size), influence of gap size (for a given value of pd) and operating frequency.

Historically, the computational techniques used for simulating low-temperature plasmas belong to two categories - continuum/fluid and kinetic methods [52]. The preferred/optimal simulation methodology is problem-specific and depends on the relevant physical mechanisms as well as the computational resources available. One common approach is to assume that the assumed distribution function is only a function of ratio of electric field to gas number density (E/n_b) and is obtained using zero-dimensional solutions to the Boltzmann equation. The validity of the zero-dimensional assumption may be questionable under certain operating conditions but is widely used for fluid modeling of microplasmas.

With the obvious computational advantages of using a continuum model (in comparison with a particle-based method), one of the fundamental questions that remains to be answered is regarding the accuracy of continuum models. While this topic has garnered significant attention in the low-pressure regime (particularly in the context of materials processing) [46], only few researchers [14, 33, 91] have studied this problem in the microplasma regime with the lack of an extensive study. One of the deficiencies of publications comparing continuum and kinetic simulations has been the absence of controlled comparisons where one operating parameter is fixed in both simulation techniques. Also, a majority of these comparisons were performed for a narrow spectrum of operating parameters. For example, Choi et al. [14] compared

PIC-MCC simulations with a drift-diffusion fluid model for a 200 μm helium microplasma operating at a current density of 10^4 A/m^2 and concluded that significant differences were observed between the two models. Hong et al. [33] compared PIC-MCC simulations and fluid simulations for microplasmas operating at 13.56 MHz and 2.45 GHz respectively and concluded that good agreement was observed at the higher frequency. Verma et al. [91] recently reported a comparative study of continuum and kinetic simulations for a direct current argon microplasma integrated operating at $pd = 1$. In this regard, the primary goal of the current work is to perform an exhaustive comparison of continuum and kinetic simulations for a range of operating conditions (direct current/microwave as well as pd values) along with an emphasis on the choice of simulation input parameters (for example transport parameters and reaction rate coefficients).

4.1 Model Description

Kinetic Simulations

The kinetic method for simulating plasmas is the stochastic method referred to as particle-in-cell with Monte Carlo collisions (PIC-MCC) where both electrons and ions are modeled as computational particles with each computational particle representing a large number of real particles (the ratio of real to simulated particles is 10^{10}). While neutral species can also be modeled as computational particles, we restrict this treatment to only ions and electrons in this work. A typical PIC-MCC simulation begins with discretization of the domain into cells followed by initialization of computational particles. The choice of cell size depends on the plasma parameters and should be less than the electron Debye length. The initial number of computational particles in each cell is based on the initial plasma number density and the ratio of real to simulated particles. The locations of computational particles within each cell are randomly chosen with the initial velocities (three components) sampled from a prescribed velocity distribution function (typically chosen to be a Maxwellian distribution). The system is then allowed to evolve in time by updating the positions and velocities of all computational particles using the Newton's laws of motion in conjunction with a second-order leap-frog algorithm[25]. The leap-frog algorithm utilizes a staggered temporal discretization where the velocities and positions are not stored at the same temporal instants. For example, if the position is stored at $t = 0$, Δt, $2\Delta t$, ..., the velocity is stored at $t = -\Delta t/2$, $\Delta t/2$, $3\Delta t/2$, ... thereby allowing the algorithm to achieve second-order accuracy. The timestep restriction purely from considerations of integrating the Newton's equations of motion is given by

$$\Delta t \leq 0.3\omega_{pe} \tag{4.1}$$

where ω_{pe} is the electron plasma frequency given by

$$\omega_{pe} = \sqrt{\frac{n_e e^2}{m_e \epsilon_0}} \tag{4.2}$$

with m_e being mass of electron. Our choice of timestep ensured that an average electron did not cross several cells during one timestep. The ratio of real-to-simulated particles for all PIC-MCC simulations was chosen in such a way that the total number of electron/ion computational particles was $\sim 70,000$. This parameter was based on a convergence study on the average number of computational particles per cell during any given timestep. All results presented were ensemble-averaged over several timesteps (typically $\sim$ 100,000) to produce results with limited statistical noise (as can be seen in our results).

At the end of every timestep, the computational particles crossing the domain boundaries will be removed from the simulation. Also, new computational particles are introduced at the boundaries based on the specified emission mechanisms. For example, secondary electron emission can be triggered by high energy species (ions, electrons and neutrals) bombarding the electrodes, field emission can be observed as a result of the high electric fields encountered at the electrodes, and thermionic emission can be encountered as a result of high temperatures at the electrodes. In this work, the only emission mechanism considered is secondary electron emission due to ion bombardment and is characterized by a constant secondary electron emission coefficient (strictly speaking, the emission coefficient depends on the incident ion energies but is not considered here for simplicity). With a specified constant secondary electron emission coefficient (γ_{se}), the flux of electrons emitted (Γ_e) from the electrodes depend on the flux of incident ions (Γ_i) and is given by

$$\mathbf{\Gamma_i} = \gamma_{se}\mathbf{\Gamma_e} \tag{4.3}$$

The algorithm discussed above is traditionally referred to as PIC since it does not include collisions between different computational particles. With the inclusion of collisions based on a Monte Carlo algorithm, the computational technique becomes PIC-MCC.

We used the XPDP1 code originally developed at the University of California Berkeley with suitable simulation parameters as discussed below. The computational domain was divided into 1000 cells (a convergence study is presented for $pd = 1$ in order to validate this choice). This also ensured that the cell size was less than the

Debye length based on the electron number density in the quasi-neutral region. The timestep was chosen between 10 fs and 100 fs and ensured that probability of missing collisions is less than 0.01 [89].

Finally, it should be mentioned that PIC-MCC simulations can be performed in the constant-current or constant-voltage mode with subtle differences in the implementation. The constant-voltage mode is the more intuitive approach wherein the potential values at both electrodes are specified and used as boundary conditions while solving the Poisson's equations. However, constant-voltage simulations have inherent stability issues without the use of an external circuit and could result in small perturbations either leading to numerical divergence or blow-off of plasma. Therefore, constant-current simulations where current through the system is specified, was preferred in this work. For such simulations, the potential at one electrode is specified (usually grounded) and the potential at the powered electrode is initially zero. During every timestep, the specified current in conjunction with the observed particle current density is used to update the powered electrode potential using Eq.(4.15).

With the use of computational particles to model electrons and ions, we could potentially include five different types of collisions including electron-neutral, ion-neutral, electron-electron, ion-ion and electron-ion interactions. Depending on the plasma operating conditions, several types of collisions may be considered important in order to capture relevant physical mechanisms. The most fundamental input that is required to perform Monte Carlo collisions in our simulations is the collision cross section as a function of incident particle energy relative to the target particle (referred to as collision energy). For collisions between particles of significantly different masses (electron-neutral and electron-ion), the relative velocity can be approximated by the velocity of electrons and hence the collision energy is same as the electron energy. However, for collisions between particles of similar masses (ion-neutral), it is important to consider the collision in a frame of reference in which one of the particles is at rest (usually a frame of reference in which the neutral species is at rest).

It is also worth mentioning that the reaction set considered here is not exhaustive. For example, at the high pressures considered in this work, the formation of argon dimer ions through a reaction between argon ion and argon neutral becomes important. Also, this leads to another reaction pathway where the electrons and dimer ions recombine to form neutral species. These reactions are not considered to ensure that we are dealing with a simple system thereby allowing us to focus on the comparisons between kinetic and continuum simulations. It is also worth mentioning that we do not anticipate the additional reactions to lead to significant changes in the qualitative behavior of the microplasmas considered.

Continuum/Fluid Simulations

Governing Equations

For the continuum simulations, we employed a plasma fluid model (implemented in an in-house code) which is essentially derived by taking velocity moments of the Boltzmann equation coupled with the Poisson's equation and closely follows the description by Fitzpatrick [21]. Our model also resembles several other fluid models for low-temperature plasmas but is described in detail here for self-sufficiency. The particle species density is governed by particle continuity equation described as

$$\frac{\partial n_k}{\partial t} + \nabla \cdot (n_k \mathbf{u}_k) = S_k \tag{4.4}$$

where $k = e, i$ for electrons and ions, respectively, n_k is number density of species k and $\mathbf{u}_k$ is average velocity of species k. S_k is source term for production of species k as a result of plasma chemistry (for example, ionization in the current work). The background gas density is assumed to be constant and is calculated based on ideal gas law using the specified pressure and temperature. The particle species flux is obtained using the moment equation corresponding to momentum of particles,

$$\frac{\partial(m_k \mathbf{u}_k n_k)}{\partial t} + \nabla.(m_k n_k \mathbf{u}_k \mathbf{u}_k) + \nabla(n_k k_b T_k) + Z_k e n_k \nabla\phi + m_k n_k \mathbf{u}_k \nu_{k,b} + m_k(\mathbf{u}_k - \mathbf{u}_j) S_k = 0 \tag{4.5}$$

where m_k is mass of species k, and T_k is temperature of species k; ϕ is the electrostatic potential; $\nu_{k,b}$ is momentum transfer frequency between species k and background gas species (obtained using electron mobility data as described below); k_b is Boltzmann's constant, e is electronic charge and value of Z_k is 1 and -1 for argon ions and electrons respectively. $\mathbf{u}_j$ is average velocity of newly formed particles which is assumed to be 0 in this study. The energy conservation equation is used to evaluate the electron temperature and is given by

$$\frac{\partial}{\partial t}\left(\frac{3}{2} k_b n_e T_e\right) + \nabla.q_e - e\mathbf{\Gamma}_e \cdot \nabla\phi + \sum_j R_{e,j} \Delta H_j + 3 k_b n_e \frac{m_e}{m_b} \nu_{e,b} = 0 \tag{4.6}$$

where $R_{e,j}$ is the rate at which the j^{th} inelastic collision occurs; ΔH_j energy lost per electron in the j^{th} inelastic collision event; m_b is mass of background gas species; $\mathbf{\Gamma}_e = n_e \mathbf{u}_e$ is electron flux and $\mathbf{q}_e$ is total electron energy flux evaluated as

$$\mathbf{q}_e = -K_e \nabla T_e + \frac{5}{2} k_b T_e \mathbf{\Gamma}_e \tag{4.7}$$

where the first term is modeled as heat flux based on Fourier approximation with thermal conductivity

$$K_e = \frac{5}{2m_e\nu_{e,b}} n_e k_b^2 T_e \tag{4.8}$$

The ion temperature T_i is assumed to be same as the background gas temperature T_b which is assumed to be constant for all simulations presented in the current work. Finally, the Poisson's equation is used to couple the conservation equations and is given by

$$\nabla^2\phi = -\nabla.E = \frac{-e}{\epsilon_0}\sum_k Z_k n_k \tag{4.9}$$

In the context of this work, the above system of equations is referred to as the full-momentum model. The above set of governing equations for plasma fluid model are solved using a standard finite volume method (FVM) implementation on a structured grid. The equations are solved in a semi-implicit form using Euler method for temporal discretization and a higher order numerical scheme with Monotonic Upstream-Centered Scheme for Conservation Laws (MUSCL) interpolation and flux limiter for spatial discretization of convective terms. A second order central difference scheme has been implemented for diffusion terms and second order least-squares method for gradient reconstruction.

In many cases, the momentum conservation equation is replaced by a simplified drift-diffusion (DD) model obtained by neglecting the inertial effect and acceleration. The DD model's primary advantages include ease of implementation and reduced computational cost. The DD equation is given by

$$\Gamma_k = \mu_k n_k E - \eta_k \nabla(n_k k_b T_k) \tag{4.10}$$

field on charged particles (drift) and the second term accounts for the effect of diffusion in a non-uniform plasma. However, we do not utilize the DD model and hence do away with the approximations involved by neglecting the inertial term.

Boundary Conditions

In order to solve the above system of equations, boundary conditions are required for each dependent variable including n_e, n_i, u_e, u_i, and T_e. The boundary condition for finite volume schemes is provided at the face of the boundary cell which is then used to compute the corresponding influx/outflux while solving the conservation equations at the boundary cell. In the description provided below, the subscript bf refers to the value at the boundary face and the subscript b refers to the cell-centered value at the boundary cell. Also, the superscript indicates the time-level. Specifically, the

superscript $q+1$ indicates the next timestep with q referring to the current timestep. The boundary condition for electron velocity is given by

$$\mathbf{u}_{e,bf}^{q+1} = \frac{1}{4} v_{th,e,b}^{q+1} \hat{n} - a\gamma_{se} \left(\frac{\mathbf{\Gamma}_{i,b}}{n_{e,b}} \right)^{q} + b\mathbf{u}_{e,b}^{q} \tag{4.11}$$

The value of a is equal to 1 if $\mathbf{\Gamma}_i$ is directed towards the electrode and zero otherwise. The value of b is equal to 1 if $\mathbf{\Gamma}_e$ is directed towards the electrode and zero otherwise. Also, $v_{th,e,b} = \sqrt{8k_b T_{e,b}/\pi m_e}$ is the thermal velocity of electrons in the boundary cell; $\hat{n}$ is the normal vector pointing towards the electrode; $\mathbf{u}_{e,b}$ is electron velocity at the boundary cell. It should be noted that the boundary condition for the next timestep is based on the values of various quantities at the current timestep with the following physical interpretation. The boundary condition for electron velocity is computed using contributions from the thermal velocity, secondary electron emission and mean velocity of electrons. Also, while the thermal velocity is always included, contribution from secondary electrons is included only if the ion flux is directed towards the boundary face. Similarly, the last term is non-zero only if electrons are drifting towards the boundary face. It is worth mentioning that the last term is typically 0 since the mean velocity of electrons is directed away from the boundary in the case of quasi-neutral plasmas with the electric field pointing toward the boundary. The boundary condition for ion velocity is given by

$$\mathbf{u}_{i,bf}^{q+1} = \mathbf{u}_{i,b}^{q} \tag{4.12}$$

where $\mathbf{u}_{i,b}$, is the ion velocity at the boundary cell. The boundary condition for ion velocity is almost identical to that of electron velocity except that no secondary emission is involved and the thermal velocity is neglected. The ions almost always move towards the boundary in a quasi-neutral plasma with the electric field pointing toward the boundary. In order to determine the ion number density at the boundary face, we utilize the condition that the ion flux at the boundary is same as the ion flux at the center of the boundary cell. In conjunction with the boundary condition for ion velocity, this leads to ion number density boundary condition given by

$$n_{i,bf}^{q+1} = n_{i,b}^{q} \tag{4.13}$$

For the electron number density boundary condition, the gradient of electron density at the boundary face is assumed to be zero and is given by

$$\nabla n_{e,bf} \cdot \hat{n} = 0 \tag{4.14}$$

This gradient condition in conjunction with the boundary cell value of electron number density at the current timestep is used to determine the boundary face value of

the electron number density at the next timestep. While the cathode potential is fixed at 0, the anode potential evolves self-consistently based on

$$\epsilon_0 \frac{\partial(\nabla\phi)_{bf}}{\partial t} = j_{i,bf} + j_{e,bf} - j_{tot} \tag{4.15}$$

where $(\nabla\phi)_{bf}$ is the gradient of potential at the powered electrode (anode boundary face), j_{tot} is the prescribed total current density, $j_{i,bf}$ is the ion current current density at the powered electrode (anode boundary face) and $j_{e,bf}$ is the electron current density at the powered electrode (anode boundary face). For the electron energy equation, boundary conditions are enforced on the electron energy flux at the boundary and is given by

$$\mathbf{q}_{e,bf} = \frac{5}{2} k_b T_{e,b} \left[\frac{1}{4} n_e v_{th,e,b} \hat{n} + b\Gamma_{e,b} \right] - a \left(\frac{5}{2} k_b T_{e,se} \right) \gamma_{se} \Gamma_{i,b} \tag{4.16}$$

with T_{se} being the temperature at which secondary electrons are emitted from the electrode surface and is taken to be 300 K for all simulations presented in this work. It should be mentioned that the secondary electrons in the PIC-MCC simulations are also emitted at a temperature of 300 K. The above boundary condition assumes that every electron lost to the boundary or introduced into the domain from the boundary carries an energy of $5k_bT_e/2$. The boundary condition for electron mean velocity and the electon energy flux are consistent with each other.

The fluid description of microplasmas requires several input parameters including reaction rate constants and momentum transfer collision frequency with both these parameters depending on the velocity distribution function. With the lack of direct information of velocity distribution functions of both electrons and ions, certain approximations are required for closure of the fluid model. While the ions are assumed to be in equilibrium (Maxwellian distribution) with the neutral gas, a zero-dimensional version of the Boltzmann's equation is commonly used to solve for the electron energy distribution function (EEDF). BOLSIG+ is a popular freeware for the numerical solution of the Boltzmann equation for electrons in weakly ionized gases in uniform electric fields. It uses a two-term approximation [29] to solve for the EEDF (at a given value of ratio of electric field to background gas number density, E/n_b) to obtain electron transport coefficients (including mobility and diffusion coefficient) and rate constants from fundamental cross section data. Since the mean electron energy (and hence electron temperature) is also obtained as a function of E/n_b, the reaction rate constants were obtained as a function of local mean electron energy (and hence electron temperature) to be provided as input to the continuum simulations presented here. While solving the zero-dimensional version of Boltzmann's equation accounts

for the potential non-Maxwellian behaviour of the EEDF, an even simpler approach is to assume that the EEDF is a Maxwellian distribution function at a given electron temperature. Once the EEDF is assumed to be Maxwellian, the reaction rate constants are obtained using the corresponding cross section data by performing suitable integration. However, it should be noted that the electron mobility still depends on E/n_b and the data obtained from BOLSIG+ (based on a non-Maxwellian EEDF) was used to provide this information to the continuum simulation even when the rate constants were based on a Maxwellian EEDF. Using the mobility data, the collision frequencies $\nu_{e,b}$ and $\nu_{i,b}$ were obtained as

$$\nu_{k,b} = \frac{|e|}{m\mu_k} \tag{4.17}$$

The ion mobility data was obtained from Ellis et al. [19] for $E/N = 8 - 2000\ Td$ and from Phelps [22] for $E/N = 2000 - 100000\ Td$ with extrapolation used to obtain mobility for E/N values outside the data range.

Argon microplasma chemistry

It was ensured that the same reaction set was used for both continuum and kinetic simulations in order to ensure meaningful comparison. We include three electron-neutral collisions and two ion-neutral collisions as summarized below along with corresponding expressions for cross section as a function of incident energy. These cross sections are the same as those summarized by Vahedi and Surendra [89], and represent the default cross sections used in the XPDP1 [90] code. It was shown [91] that the expressions used in XPDP1 agree closely with the cross section described in the Phelps database [23] and the BSR [98] cross sections (B-Spline R-matrix) based on quantum mechanical calculations. For a detailed comparison of cross sections for electron-argon collisions in various databases, the reader is referred to the work of Pitchford et al. [75]. For ion-neutral collisions, we included both charge exchange and elastic scattering collisions [89]. It should be noted that the excited argon atoms were not tracked in the simulations presented here. It is also worth mentioning that the reaction set considered here is not exhaustive. For example, at high pressures, the formation of argon dimer ions through a reaction between argon ion and argon neutral becomes important. Also, this leads to another reaction pathway where the electrons and dimer ions recombine to form neutral species. These reactions are not considered here in order to ensure that we are dealing with a simple system thereby allowing us to focus on the comparisons between kinetic and continuum simulations.

Table 4.1: Summary of electron-neutral and ion-neutral collisions included in this work. The default cross sections in XPDP1 [89] was used to perform both kinetic and continuum simulations.

Collision
$e + Ar \rightarrow e + Ar$ (elastic)
$e + Ar \rightarrow e + Ar^*$ (excitation)
$e + Ar \rightarrow e + e + Ar^+$ (ionization)
$Ar^+ + Ar \rightarrow Ar + Ar^+$ (charge exchange)
$Ar^+ + Ar \rightarrow Ar^+ + Ar$ (elastic scattering)

4.2 Results and Discussion

The kinetic and continuum simulations using various physical models described above were performed for a range of microplasma operating conditions with the results compared and contrasted in detail below.

Effect of pd at constant gap size

In this section, we compare PIC-MCC and continuum simulations for various pd values at a fixed gap size. The simulations were performed for an argon gap of 100 μm with the background gas temperature fixed at 300 K. For these simulations, the pressure was varied from 100 Torr to 700 Torr thereby corresponding to pd values ranging from 1 to 7. The secondary electron emission coefficient was fixed at 0.05. The current-controlled PIC-MCC simulations were performed at 0.2 $\mu A/\mu m^2$ with the applied potential obtained self-consistently from the simulations. While the cross section area was taken as 0.01 m^2 for the purpose of performing the simulations, the results (for example, for current) are presented per unit area and are not affected by the choice of cross section area (as is the norm for one-dimensional simulations). The results obtained from PIC-MCC simulations are known to depend primarily on two simulation parameters including the cell size and the average number of computational particles per cell. Therefore, we first performed a study to quantify the dependence of results on both these parameters. To characterize the dependence on cell size, we performed simulations with 250, 500, 1000 and 2000 cells with the number of computational particles per cell fixed by suitably choosing the ratio of real to simulated particles. The ratio of real to simulated particles for the four cases was chosen as 4×10^{11}, 2×10^{11}, 1×10^{11}, and 5×10^{10} respectively. In order to determine the dependence of the ratio of real to computational particles, we performed three

different simulations with values of 2×10^{11}, 1×10^{11} and 5×10^{10} respectively. The number of cells was fixed as 1000 for all these simulations.

Figures 4.1 and 4.2 show the time history of number of computational particles for various cell size and ratio of real to computational particles. The time history demonstrates that all simulations reached steady state when simulated for about 4 μs. Figures 4.3 and 4.4 show the electron number density profiles obtained for the various cell sizes and various values for the ratio of real to simulated particles. Based on these results, we chose to perform all PIC-MCC simulations reported in this work using 1000 cells and around 50 computational particles per cell. It should be noted that the choice was based on a trade-off between computational accuracy and cost. Figure 4.5 shows a representative convergence study performed for the continuum simulation with results shown for four different cell sizes. The production simulations used to compare with PIC-MCC simulations were performed using 800 cells.

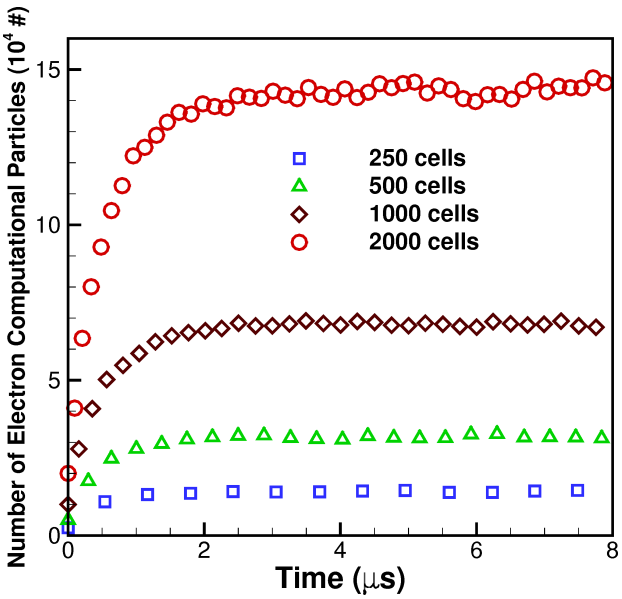

Figure 4.1: Comparison of time history showing the number of computational particles (electron) for various values of cell size. The ratio of real to computational particles was suitably changed to ensure that the number of computational particles per cell was fixed.

The PIC-MCC results are considered benchmark for comparison with results of the continuum simulation using full-momentum equations for both ions and electrons. Simulations were performed using rate constants based on both Maxwellian

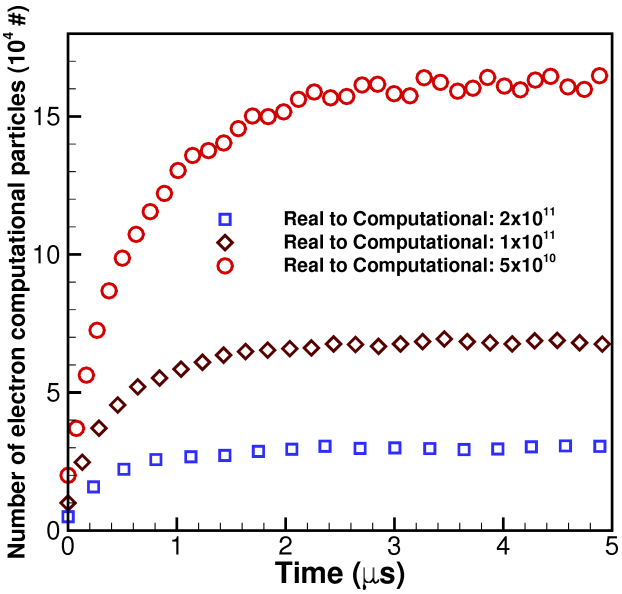

Figure 4.2: Comparison of time history showing the number of computational particles (electron) for various values of the ratio of real to computational particles. The number of cells was fixed at 1000.

and non-Maxwellian (zero-dimensional BOLSIG+ solution) EEDFs. In order to enable meaningful comparisons, the continuum simulations were also performed at the same prescribed current density (0.2 $\mu A/\mu m^2$). Figures 4.6 compares the plasma number density profiles obtained using the continuum model (with full-momentum equations for both electrons and ions) with those obtained using kinetic simulations. It can be seen that the plasma number density is under-predicted by both continuum simulations with the PIC-MCC simulations predicting a peak number density that is a factor of 3 higher than the continuum simulation based on the Maxwellian EEDF. The continuum simulation based on the non-Maxwellian EEDF (from BOLSIG+) leads to a peak number density that is an order of magnitude lower than that predicted by the continuum simulation using a Maxwellian EEDF. However, it is worth pointing out that the ion number density in the sheath is consistent across all three simulations. The electron number density in the sheath region, in spite of subtle differences, is comparable across the three simulations with the continuum simulations leading to extremely similar profiles as expected. As we move away from the cathode, the PIC-MCC simulations demonstrate a more rapid increase of the electron number density and hence a smaller sheath thickness. The continuum simulation using the

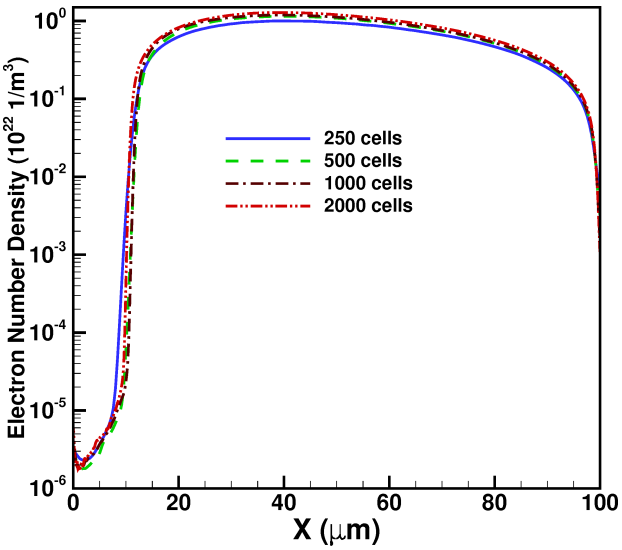

Figure 4.3: Comparison of electron number density profiles obtained using PIC-MCC simulations with various cell sizes.

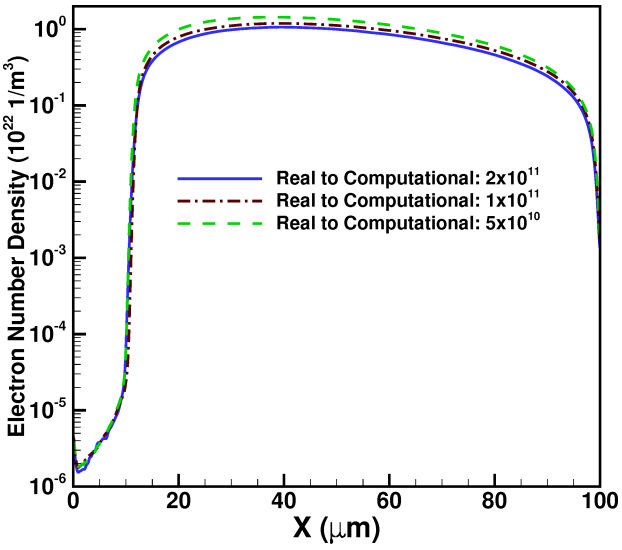

Figure 4.4: Comparison of electron number density profiles obtained using PIC-MCC simulations with various values for the ratio of real to computational particles.

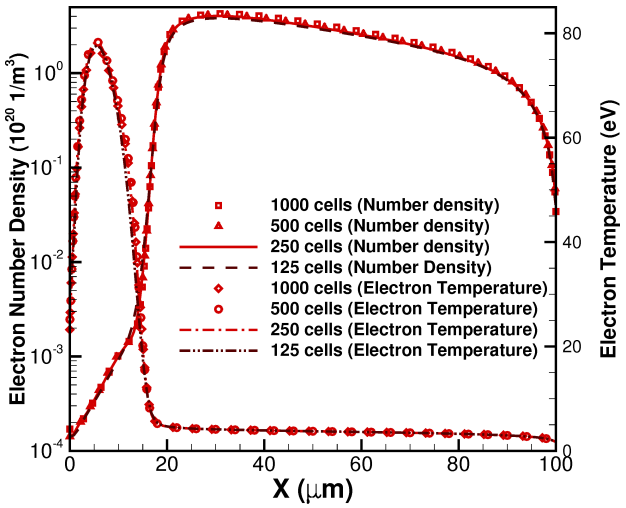

Figure 4.5: Comparison of electron number density and electron temperature profiles obtained using continuum simulations with various cell sizes.

Maxwellian EEDF leads to good qualitative agreement with the number density profile predicted by PIC-MCC. As a result of the higher plasma density, the PIC-MCC simulation has the lowest sheath thickness followed by the Maxwellian continuum simulation with the non-Maxwellian simulation predicting the largest sheath thickness. The sheath thickness predicted by the three simulations are between 10 and 20 μm.

Figure 4.7 shows the potential profiles across the gap for the PIC-MCC and the continuum simulations. While all three simulations were performed at a prescribed total current density of 0.2 $\mu A/\mu m^2$, the required applied potential to achieve this current density is significantly different. Specifically, applied potential in the PIC-MCC simulations is about 385 V in comparison to 605 V in the continuum simulation using Maxwellian EEDF which further increases to 680 V for the continuum simulation using non-Maxwellian EEDF.

Figure 4.8 compares the electron temperature profiles obtained from the three simulations with the electron temperature predicted by PIC-MCC simulations being significantly higher than the continuum simulations. Both continuum simulations (with Maxwellian and non-Maxwellian EEDF) predict comparable electron temperature profiles with a peak value of 70 eV which is at least a factor of 2 lower than the value of 160 eV predicted by the PIC-MCC simulations. The electric field profiles (not shown here) including the peak electric field in the sheath are in good agreement

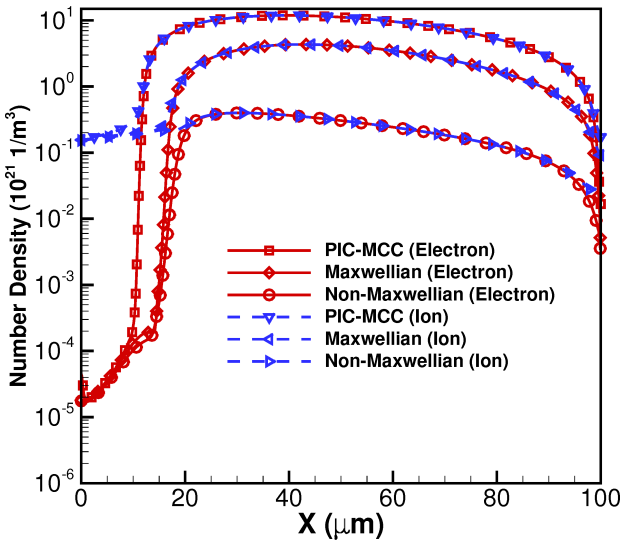

Figure 4.6: Comparison of plasma number density profiles obtained using PIC-MCC and continuum simulations for $pd = 1$. Results obtained using both Maxwellian and non-Maxwellian EEDF obtained from BOLSIG+ are shown for the continuum simulation.

with each other. Figure 4.9 shows the electron and ion velocities obtained from kinetic and continuum simulations. While the overall trend is consistent across simulations, both continuum simulations over-predict the electron velocities. The ion velocities from all three simulations agree reasonably well with each other which is a direct consequence of the good agreement for ion number density in the sheath and hence the cathode electric field. The over-prediction of the electron velocities and under-prediction of plasma number densities are related since the total current density is fixed at 0.2 $\mu A/\mu m^2$ for all three simulations.

The next set of simulations were performed at a pressure of 300 Torr thereby corresponding to $pd = 3$. Figures 4.10 and 4.11 show comparisons of representative parameters obtained from kinetic and continuum simulations (with Maxwellian EEDF) for $pd = 3$. The current density for both simulations was 0.2 $\mu A/\mu m^2$. It should be mentioned that a current density of 0.2 $\mu A/\mu m^2$ produced a plasma with positive charge in the entire gap (pre-breakdown regime with no quasi-neutral region) when simulated with the non-Maxwellian EEDF and hence is not considered here. This is likely due to the fact that the minimum current density for plasma ignition is greater than 0.2 $\mu A/\mu m^2$. In comparison to the $pd = 1$ simulations, the peak number

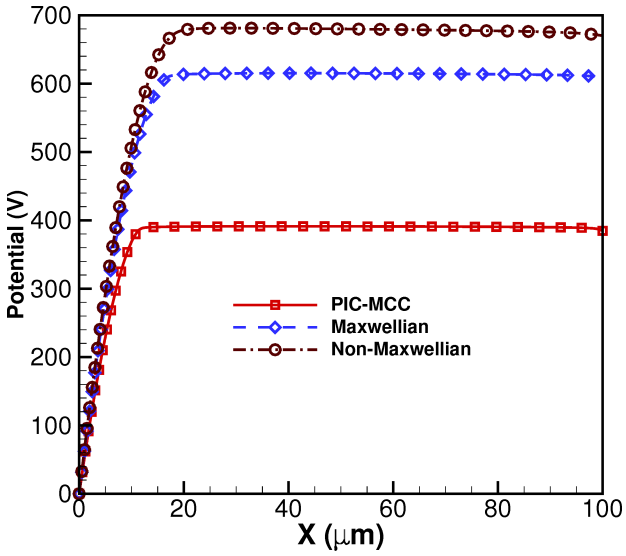

Figure 4.7: Comparison of potential profiles obtained using PIC-MCC and continuum simulations for $pd = 1$. Results obtained using both Maxwellian and non-Maxwellian EEDF obtained from BOLSIG+ are shown for the continuum simulation.

density shifts towards the cathode in both kinetic and continuum simulations. Unlike the $pd = 1$ simulations, the applied voltage required to obtain a current density of 0.2 $\mu A/\mu m^2$ are comparable (approximately 250 V) for both kinetic and continuum simulations. The sheath thickness predicted by both simulations are comparable at about 10 μm even though the discrepancy in the peak number densities is significant. The number density profile obtained from the continuum simulation also has a sharper peak (in comparison to the PIC-MCC simulations followed by a region of almost constant number density. The electron temperature (not shown here) in the quasi-neutral region decreased when compared to the $pd = 1$ simulation. As in the previous case, the continuum simulation performed using the Maxwellian EEDF under-predicts the electron temperature in the quasi-neutral region. The peak electric field magnitude at the cathode (not shown here) predicted by the continuum simulation agrees extremely well with the PIC-MCC simulations which is a consequence of the good agreement for ion number density and ion velocity in the sheath (refer to Figure 4.11). However, the electron velocity profiles demonstrate differences by as high as an order of magnitude and is one of the reasons for the under-prediction of the plasma number density.

The final set of simulations presented here correspond to a pressure of 700 Torr

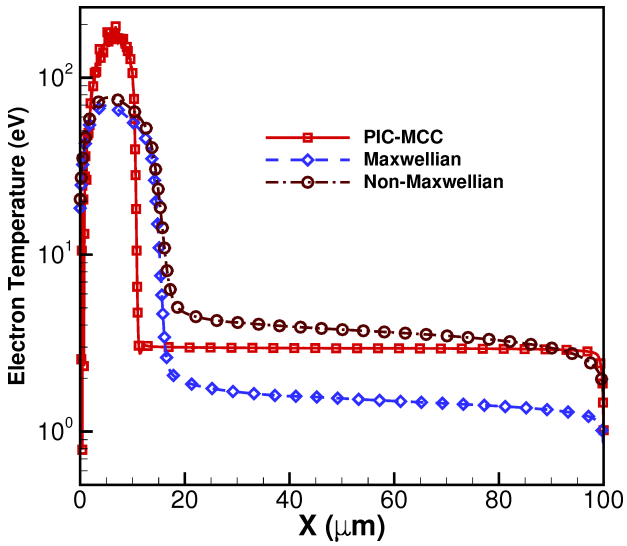

Figure 4.8: Comparison of electron temperature profiles obtained using PIC-MCC and continuum simulations for $pd = 1$. Results obtained using both Maxwellian and non-Maxwellian EEDF obtained from BOLSIG+ are shown for the continuum simulation.

and therefore $pd = 7$. Figures 4.12 and 4.13 present representative comparisons of PIC-MCC and continuum simulations for $pd = 7$. It should be reiterated that the non-Maxwellian EEDF could not be ignited at the prescribed current density of 0.2 $\mu A/\mu m^2$ and hence is not considered here. Of all the cases considered in this work, the $pd = 7$ case has the best agreement for plasma number density between kinetic and continuum simulations. However, it should be pointed out that the continuum simulation leads to a region with flat plasma number density which is not observed in the PIC-MCC simulation. The electron temperature in the quasi-neutral region predicted by the continuum simulation is lower than the corresponding value in PIC-MCC simulations which has been a consistent trend for all pd values considered here. The magnitude of peak electric field in the sheath is predicted accurately as a result of consistent prediction of ion number density in the sheath by both simulations.

Figure 4.14 compares the ensemble-averaged (same as time-averaged for direct current simulations) electron energy probability function (EEPF) obtained from PIC-MCC simulations (at various spatial locations characterized by distance from cathode) along with the Maxwellian EEPF at the corresponding electron temperature. It is clear that the PIC-MCC EEPF has a high-energy tail region which cannot be ac-

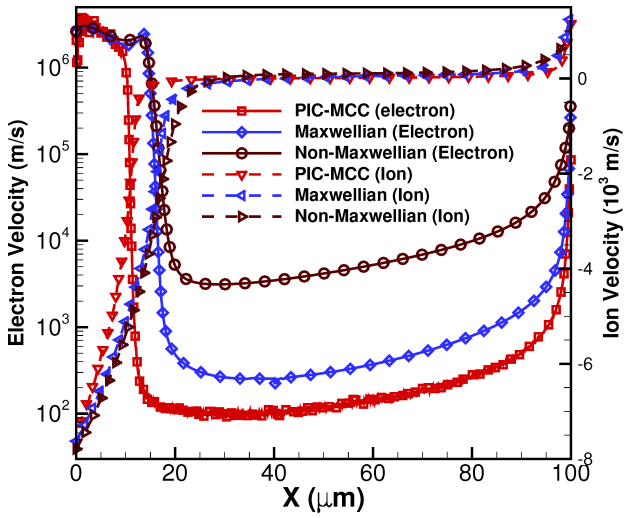

Figure 4.9: Comparison of electron and ion velocity profiles obtained using PIC-MCC and continuum simulations for $pd = 1$. Results obtained using both Maxwellian and non-Maxwellian EEDF obtained from BOLSIG+ are shown for the continuum simulation.

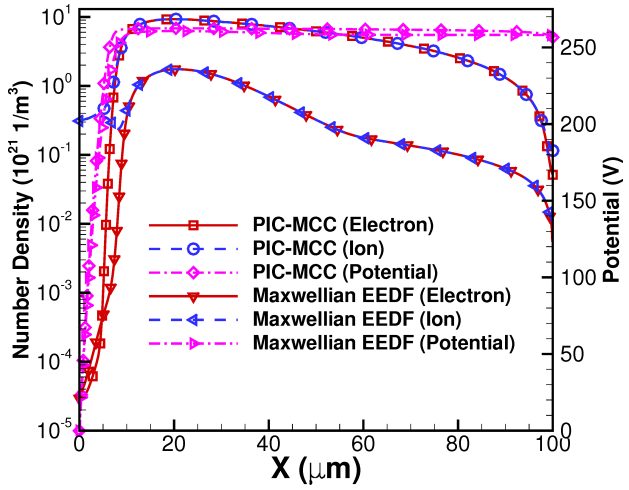

Figure 4.10: Comparison of plasma number density and potential profiles obtained using PIC-MCC and continuum simulations (using Maxwellian EEDF) for $pd = 3$.

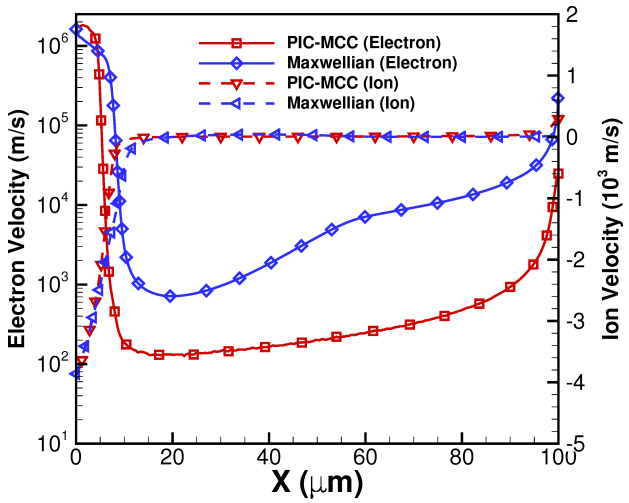

Figure 4.11: Comparison of electron and ion velocity profiles obtained using PIC-MCC and continuum simulations (using Maxwellian EEDF) for $pd = 3$.

counted for in the continuum simulations using Maxwellian/non-Maxwellian EEPF. Specifically, the non-Maxwellian EEPF predicted by BOLSIG+ has a depleted high-energy tail which explains the observation that the non-Maxwellian continuum simulations required much higher potentials to ignite the plasma. While the Maxwellian EEPF does not deplete the tail, it still does not capture the high-energy tail of the EEPF accurately. The high energy tail region can be attributed to runaway [55, 57] secondary electrons that gain significant energy while traveling across the sheath and these electrons extend well into the quasi-neutral region in the microplasmas simulated in this work. Also, the PIC-MCC EEPFs could possibly be described by a bi-Maxwellian distribution with two characteristic temperatures and formulating multi-temperature models could be an important direction in improving the accuracy of continuum simulations of DC microplasma devices that are expected to have significant secondary electron emission. Our results for microwave microplasmas presented in a subsequent section agree with this explanation.

With the PIC-MCC simulations providing accurate non-Maxwellian EEDF information including the presence of runaway electrons, performing continuum simulations by using this information was considered as a possible option to enhance their accuracy. However, this option was dismissed for the following reasons. Firstly, the runaway electrons and hence the EEDF greatly depend on the operating conditions. Therefore, the rate coefficient dependence on electron temperature is not expected

to be unique even for microplasmas operating at different voltages, let alone different *pd* values. Also, with the spatial variation of EEDF and electron temperature particularly in the sheath, the rate coefficient for a given electron temperature is not unique thereby leading to ambiguity. The use of PIC-MCC EEDFs in continuum simulations was therefore discounted in this work particularly for the lack of generality and uniqueness. In other words, the best way to feed information to the continuum simulations would be one-dimensional PIC-MCC simulations at the corresponding conditions which would then defeat the purpose of a continuum simulation in the first place.

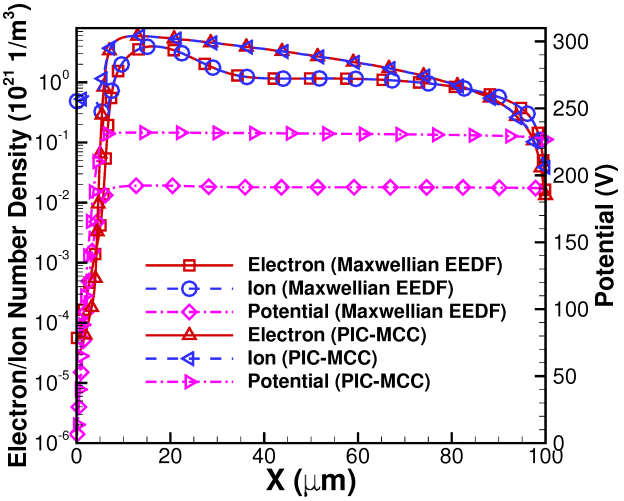

Figure 4.12: Comparison of plasma number density and potential profiles obtained using PIC-MCC and continuum simulations (using Maxwellian EEDF) for $pd = 7$.

In order to understand the influence of secondary electron emission coefficient on the high-energy runaway electrons and hence on agreement between continuum and kinetic simulations, we compared the results obtained for $\gamma_{se} = 0.005$ at $pd = 7$. The current density was fixed at 0.2 μA/μm^2 (same as for other simulations presented earlier). Figure 4.15 shows the spatial profiles of plasma number density and potential obtained from both continuum (with Maxwellian EEDF) and kinetic simulations. The plasma density predicted by the PIC-MCC simulations is about a factor of 8 higher than that predicted by the continuum simulation. In other words, the discrepancy between the continuum and kinetic simulations is higher for the $\gamma_{se} = 0.005$ case when compared to the $\gamma_{se} = 0.05$ case presented earlier. Also, the PIC-MCC simulation predicted a significantly higher applied voltage (in comparison to the Maxwellian

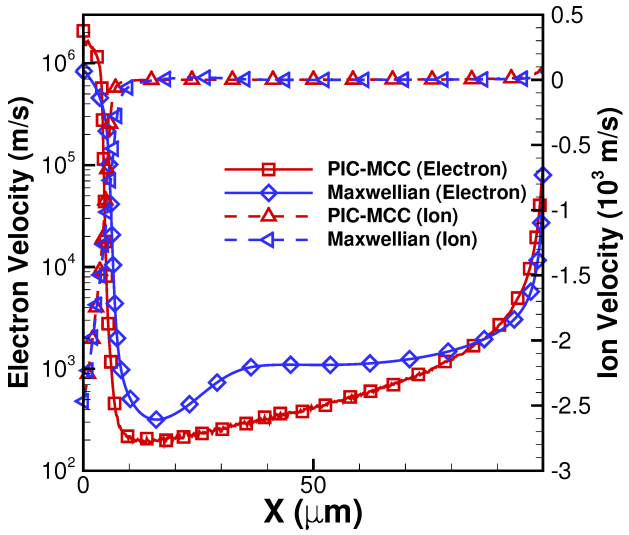

Figure 4.13: Comparison of electron and ion velocity profiles obtained using PIC-MCC and continuum simulations (using Maxwellian EEDF) for $pd = 7$.

EEDF continuum simulation) to achieve the given current density. Specifically, the PIC-MCC voltage of 520 V is about 180 V higher than the Maxwellian EEDF continuum simulation voltage. These results point to a very interesting connection between the secondary electron emission coefficient, the resulting applied voltage and the influence of runaway electrons. While one would anticipate that decreasing the influence of boundary processes by decreasing secondary electron emission coefficient would lead to a decrease in the fraction of high-energy electrons, the corresponding increase in applied voltage actually leads to an effectively larger contribution of runaway electrons. Specifically, the difference in voltage between the $\gamma_{se} = 0.05$ and $\gamma_{se} = 0.005$ PIC-MCC simulations is about 280 V. This difference in voltage leads to electrons being accelerated to much higher energies (as confirmed by the EEDF results presented below). While Maxwellian EEDF continuum simulations predict the same (expected) trend with higher voltage for the $\gamma_{se} = 0.005$ case, the predicted increase is only about 150 V. Therefore, apart from the value of the secondary electron emission coefficient, the resulting operating voltage plays a significant role in the utility of continuum simulations.

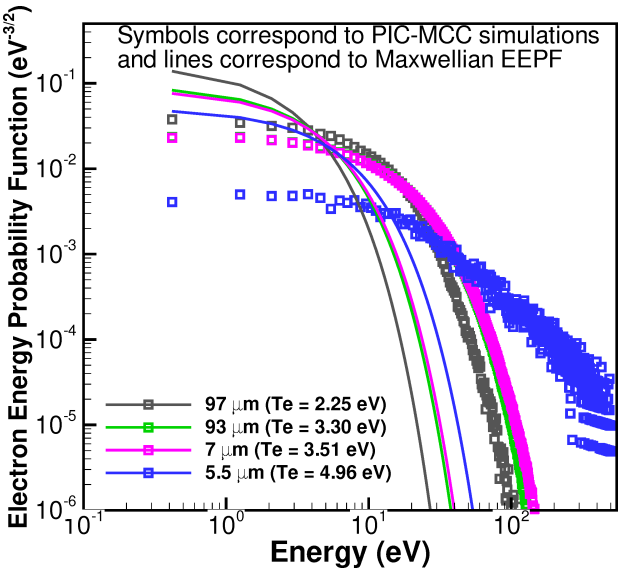

Figure 4.14: Comparison of ensemble-averaged (same as time-averaged for direct current simulations) EEPF obtained using PIC-MCC and corresponding Maxwellian EEPF based on local electron temperature at various spatial locations for $pd = 7$. The locations are characterized by distances from cathode.

Effect of gap size at constant pd

The next set of simulations were performed for two different gap sizes (20 μm and 1 cm) at constant $pd = 1$ in order to study the influence of gap size on the agreement between continuum and kinetic simulations. It should be noted that results were already presented and discussed for the $pd = 1$ case corresponding to a gap size of 100 μm. The pressures for the simulations at 1 cm and 20 μm were taken as 1 Torr and 500 Torr respectively. As a result of pd scaling, we anticipate that decreasing the gap size (for a given voltage) by a factor of 10 will lead to a factor of 100 increase in the number density and hence current density. Therefore, we simulated the 1 cm plasma at a current density of 20 A/m^2, the 100 μm and the 20 μm plasma at a current density of 5 $\mu A/\mu m^2$. It is worth noting that the 100 μm microplasma simulated earlier was operating at a current density of 0.2 $\mu A/\mu m^2$. Figure 4.16 compares the number density profiles obtained for the 1 cm plasma using kinetic and continuum simulations (including Maxwellian and Non-Maxwellian EEDF based reaction rate coefficients) and the striking similarity with the results of the 100 μm microplasma is immediately evident. The PIC-MCC simulation predicts a plasma

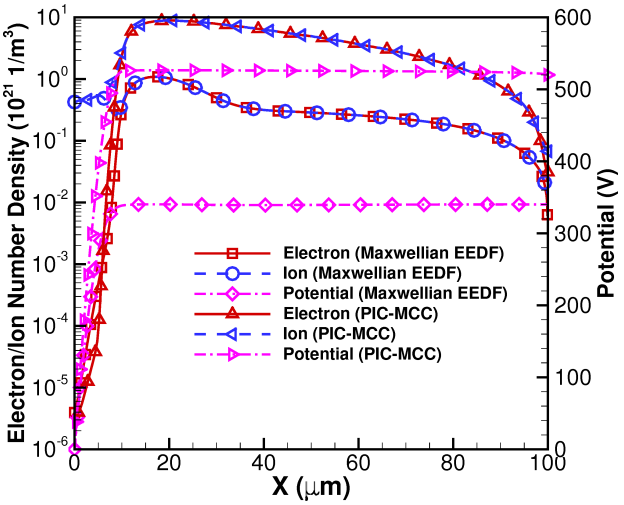

Figure 4.15: Comparison of plasma number density and potential profiles obtained using PIC-MCC and continuum simulations (using Maxwellian EEDF) for $pd = 7$. The secondary electron emission coefficient was fixed at $\gamma_{se} = 0.005$

density that is about a factor of 4 higher than the Maxwellian EEDF continuum simulation. The continuum simulation using the non-Maxwellian EEDF continues to significantly underpredict (by close to an order of magnitude) the plasma densities. Figure 4.17 shows the potential profiles obtained using the three simulations with the applied potential to achieve a current density of 20 A/m^2 being comparable to the required potential to achieve a current density of 0.2 $\mu A/\mu m^2$ in the 100 μm microplasma. This demonstrates that all three simulations predict results that are consistent with the pd scaling. Interestingly, the simulations (Figures 4.18 and 4.19) for the 20 μm gap also predict pd scaling with almost identical applied potentials to achieve a current of 5 $\mu A/\mu m^2$. In summary, the conclusions regarding agreement of continuum and kinetic simulations based on results presented earlier are expected to show no dependence on the gap size.

Microplasma at microwave frequency

Finally, we also present one representative simulation of microplasmas operating at microwave frequencies since ignition of microplasma devices using GHz to THz frequencies is actively pursued by several researchers [58]. In this work, we present results an argon microwave microplasma operating in a gap size of 200 μm at a pres-

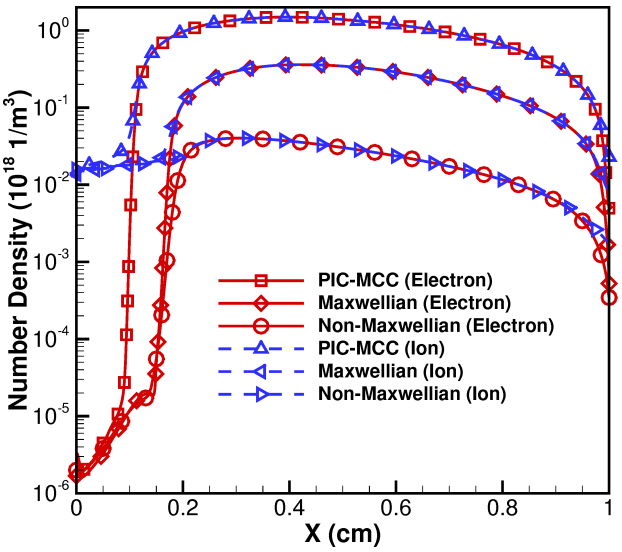

Figure 4.16: Comparison of number density profiles obtained using PIC-MCC and continuum simulations (Maxwellian and non-Maxwellian EEDF) of an argon plasma operating in a 1 cm gap at a current density of 20 A/m^2.

sure of 760 Torr. These conditions are similar to the operating parameters of split-ring resonator microplasma devices that have been extensively tested by Hopwood *et al.* (for example [41, 40, 27, 34]). One-dimensional fluid simulations have also been reported [36, 26] based on the drift-diffusion model (using an effective electric field approach) for the electrons and the full-momentum equation for ions (that are more or less stationary under these conditions). The secondary electron emission was set to be equal at both electrodes for the PIC-MCC and continuum simulations reported here. At the lower current density considered in this work, the microplasma is anyway expected to operate in the α-mode with limited influence on boundary processes. We confirm this by comparing the $\gamma_{se} = 0.07$ and $\gamma_{se} = 0$ and the results are shown to be nearly identical. While operation at the higher current density is expected to show some dependence on boundary processes, this work restricted itself to the case of $\gamma_{se} = 0$ for these current densities to study current density and frequency effects without the additional complexity of boundary processes. The gas temperature was set to 800 K based on measurements [36] performed in a comparable microplasma device. All time-averaged results presented here were obtained by averaging over half the cycle. Continuum simulation parameters such as electron collision frequency were same as for the DC simulations presented earlier. Also, it should be noted that the

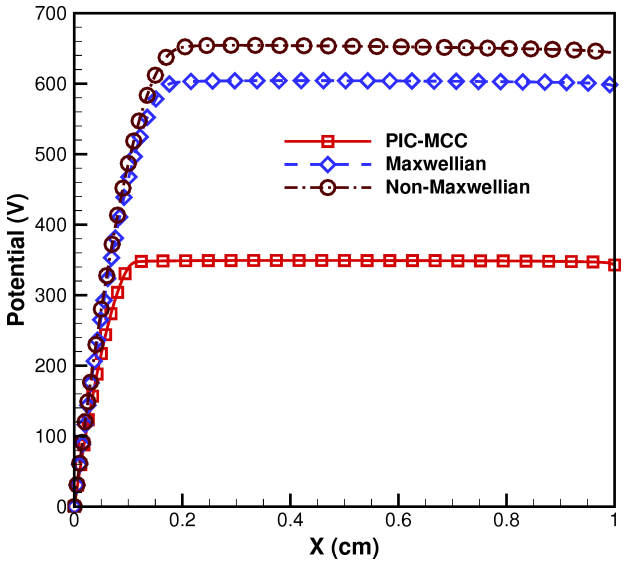

Figure 4.17: Comparison of potential profiles obtained using PIC-MCC and continuum simulations (Maxwellian and non-Maxwellian EEDF) of an argon plasma operating in a 1 cm gap at a current density of 20 A/m^2.

simulations assume that an electrostatic description obtained by solving the Poisson's equation is sufficiently accurate. This is supported by the fact that the gap size of 200 μm is significantly smaller than the wavelength corresponding to the excitation frequency for frequencies up to 150 GHz. The wavelength of 2 mm would still be a factor of 10 higher than the gap size at an excitation frequency of 150 GHz. At higher frequencies, an electromagnetic description enabled by solving the Maxwell's equations would be more suitable.

We first performed a study to determine the dependence of the PIC-MCC results on the ratio of real to computational particles. The simulation parameters included a current density amplitude of 0.05 $\mu A/\mu m^2$, $\gamma_{se} = 0$ and an excitation frequency of 0.5 GHz. Figure 4.20 compares the electron number density profiles obtained using three different values for the ratio of real to computational particles. Based on the results, it was determined that a value of 5×10^8 produced acceptable results and was used to perform the simulations presented below. The total number of computational particles for this simulation was about 70,000. The simulations at other frequencies and current densities utilized a comparable number of computational particles by suitably varying the ratio of real to computational particles.

Figure 4.21 shows the time-averaged electron and ion number density profiles ob-

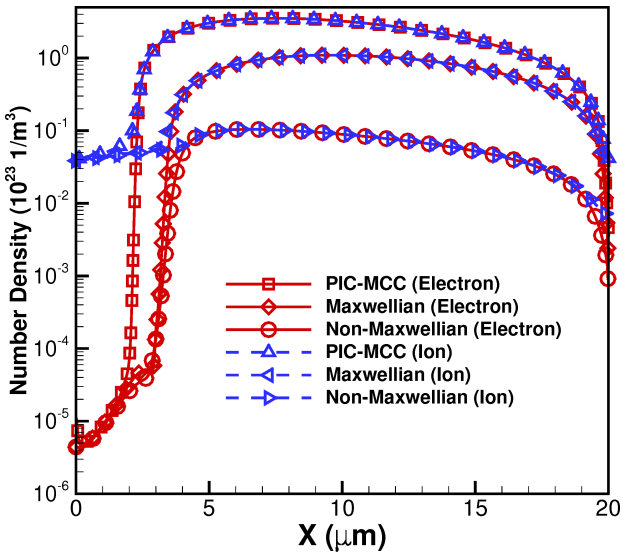

Figure 4.18: Comparison of number density profiles obtained using PIC-MCC and continuum simulations (Maxwellian and non-Maxwellian EEDF) of an argon plasma operating in a 20 μm gap at a current density of 5 $\mu A/\mu m^2$.

tained from PIC-MCC and continuum simulations (Maxwellian and non-Maxwellian EEPF) for a microplasma operating at a current density amplitude of 0.05 $\mu A/\mu m^2$, frequency of 0.5 GHz and $\gamma_{se} = 0.07$. The number densities obtained using rate constants based on the non-Maxwellian EEPF agree extremely well with the PIC-MCC simulations indicating that the EEPF in microwave microplasmas is comparable to the non-Maxwellian EEPF predicted from BOLSIG+. However, we were not able to make direct comparisons with the PIC-MCC EEPF since capturing the unsteady behavior of EEDFs accurately would require an infeasible number of computational particles. The sheath thicknesses corresponding to the three simulations correlate well with the number density with the Maxwellian simulation leading to the thinnest sheath. Unlike the direct current simulations presented earlier, the ion number density profile in the sheath is predicted to be slightly higher by the Maxwellian simulation in spite of the total current density being the same for all three cases. This can be attributed to the interplay between the ion number density, electric field and hence displacement current. Figure 4.22 compares the time history profiles of voltages obtained using continuum (using non-Maxwellian EEDF) and PIC-MCC simulations. The PIC-MCC simulation continues to predict a lower applied voltage to achieve a given current density at 105 V amplitude in comparison to about 150 V predicted by

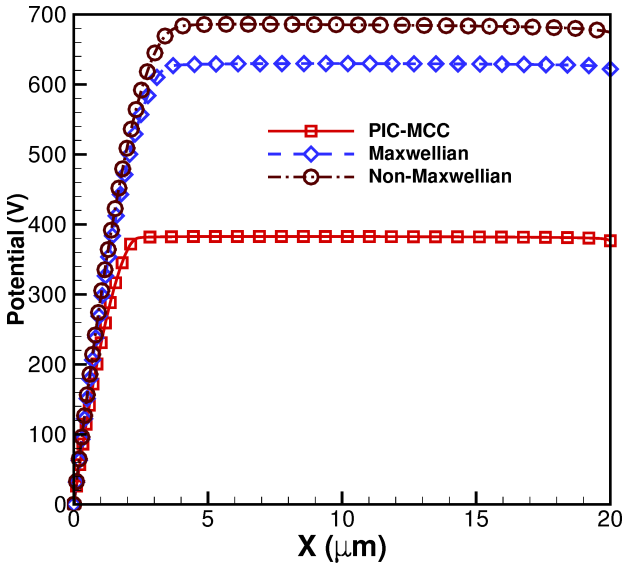

Figure 4.19: Comparison of potential profiles obtained using PIC-MCC and continuum simulations (Maxwellian and non-Maxwellian EEDF) of an argon plasma operating in a 20 μm gap at a current density of 5 $\mu A/\mu m^2$.

the continuum simulations. Both simulations predict that current leads voltage by about 0.4π radians with the PIC-MCC simulation predicting a slightly higher phase difference than the continuum simulations. The magnitude of impedance $|Z|$ (per unit cross section area) is obtained as the ratio of voltage amplitude to current amplitude as 0.003 Ω/m^2 (PIC-MCC simulations) and 0.0021 Ω/m^2 (continuum simulations) respectively.

Figures 4.23 and 4.24 show the corresponding results for a microplasma operating at $\gamma_{se} = 0$. Based on the results obtained for the $\gamma_{se} = 0.07$, continuum simulations were performed only using the Non-Maxwellian EEDF. The results are are very similar to that obtained for $\gamma_{se} = 0.07$. In spite of the similarities, there are differences worth mentioning. For example, the continuum simulation predicts a slightly larger number density than the PIC-MCC simulation. Also, the phase shift between current and voltage predicted by the two simulation techniques are different by about 0.1π radians with the continuum simulation predicting a smaller phase shift than the PIC-MCC simulation. This difference was concluded to be small enough to confirm that boundary processes do not have a significant effect on the operation of microwave microplasmas at the low current density considered here.

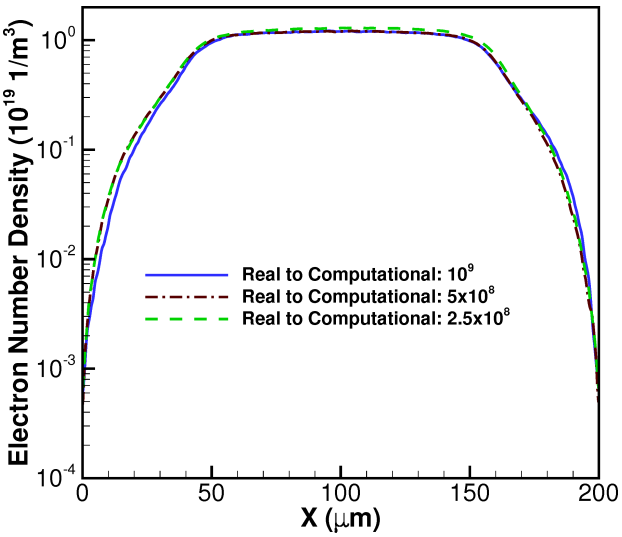

Figure 4.20: Comparison of electron number density profiles in an argon microplasma (200 μm and 760 Torr) obtained using PIC-MCC simulations with various values for the ratio of real to computational particles.

Figures 4.25 and 4.26 show the corresponding results for a microplasma operating at 0.8 GHz. The current density amplitude was taken to be 0.05 $\mu A/\mu m^2$ (same as above) and γ_{se} was fixed at 0. The number density profiles obtained from the two techniques were once again nearly identical with only subtle differences. The peak number density was around 1.6×10^{19} 1/m^3 from the PIC-MCC simulation and 1.2×10^{19} 1/m^3 from the continuum simulation. This peak number density value is also comparable to the peak number density obtained for the 0.5 GHz simulations presented earlier indicating that fixing the current density is equivalent to fixing the peak number density. The peak voltage predicted by the PIC-MCC simulation (55 V) continued to be lower than the voltage predicted by the continuum simulation (90 V). Also, it should be noted that the peak voltage to obtain a given current density (equivalent to a given number density) decreased with the increase in frequency indicating that the power requirement to achieve a given number density is lower for the 0.8 GHz excitation.

Simulations were also performed at a higher peak current density of 0.4 $\mu A/\mu m^2$ for a microplasma operating at 2 GHz. The value of γ_{se} was set to be 0. A higher current density was chosen for the higher frequency partially because of experimental evidence that fixing the power and operating a microplasma at higher frequency auto-

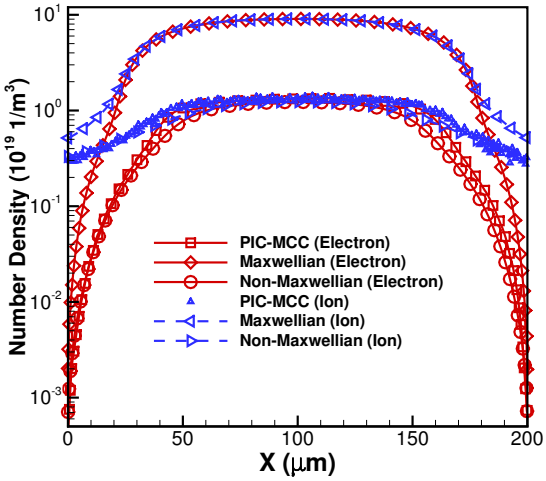

Figure 4.21: Comparison of number density profiles obtained using PIC-MCC and continuum simulations (Maxwellian and non-Maxwellian EEDF) of an argon microplasma operating in a 200 μm gap at a current density amplitude of 0.05 $\mu A/\mu m^2$, frequency of 0.5 GHz and $\gamma_{se} = 0.07$.

matically results in a higher current density. Figure 4.27 compares the number density profiles obtained using both continuum (non-Maxwellian EEDF) and PIC-MCC simulations. Once again, there is good overall agreement between the two methods even though the PIC-MCC simulation present a local minimum at the mid-point with symmetrical off-center peaks which is not captured by the continuum simulation. Figure 4.28 shows the time history of potential using both simulation techniques. As with the previous cases, the PIC-MCC simulation predicts a lower voltage (90 V in comparison to 120 V) for a given current density and the phase difference between current and voltage waveforms are comparable (0.3π from continuum simulations and 0.4π from PIC-MCC simulations.

A second set of simulations were also performed at a peak current density of 0.4 $\mu A/\mu m^2$ and a frequency of 4 GHz with results summarized in Figures 4.29 and 4.30. The results are consistent with other results presented in this work and demonstrated good agreement between the non-Maxwellian EEDF continuum simulations and PIC-MCC simulations. Once again, the increase in frequency leads to a decrease in power requirements to achieve a given current density (or peak plasma density). Also, the PIC-MCC simulations predict a lower peak voltage (45 V) than the contin-

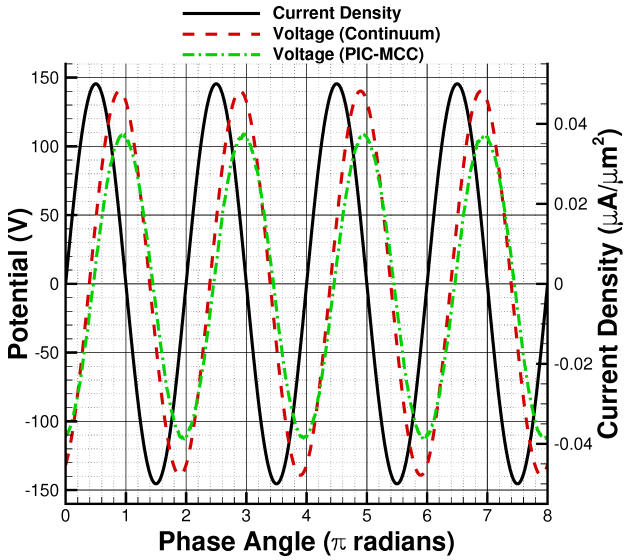

Figure 4.22: Comparison of history profiles of current density and applied potential obtained using PIC-MCC and continuum simulations (non-Maxwellian EEDF) of an argon microplasma operating in a 200 μm gap at a current density amplitude of 0.05 $\mu A/\mu m^2$, frequency of 0.5 GHz and $\gamma_{se} = 0.07$.

uum simulations (80 V) with good agreement in the phase shift predictions.

The general trend in all microwave microplasma simulations considered in this work was that the number density profiles predicted by continuum simulations were in good agreement with corresponding results from PIC-MCC simulations. The lower voltage (and hence lower power) predicted by the PIC-MCC simulations to achieve a given current density (or given plasma density) could be attrbuted to the electron heating modes that are captured in each of the techniques. Specifically, the continuum simulations only account for ohmic heating whereas the PIC-MCC simulations account for both ohmic and stochastic heating. The small discrepancy in voltages could therefore be attributed to the contribution of stochastic heating which is not included in the continuum simulations. However, other reasons are also possible and require further studies. In spite of the results presented here, it is worth mentioning that this work is non-exhaustive. Microwave microplasmas have several interesting operating modes that have been considered by several researchers [51, 56, 54]. Comparisons at all of these conditions is beyond the scope of this work and future work should focus on comparing and validating microwave microplasmas at some of these other operating conditions.

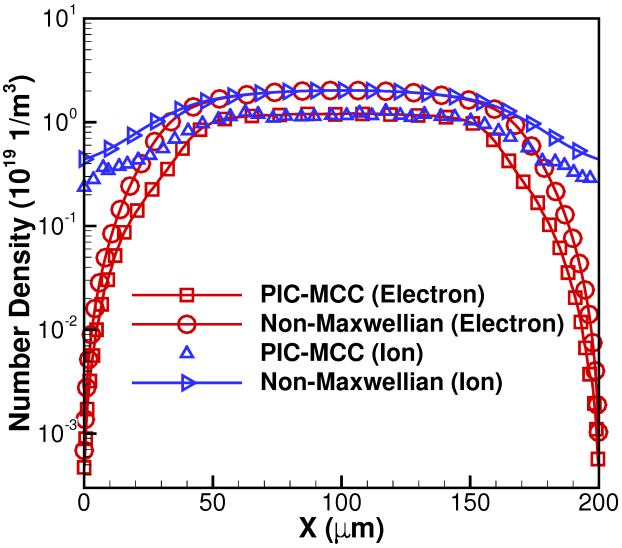

Figure 4.23: Comparison of number density profiles obtained using PIC-MCC and continuum simulations (non-Maxwellian EEDF) of an argon microplasma operating in a 200 μm gap at a current density amplitude of 0.05 $\mu A/\mu m^2$, frequency of 0.5 GHz and $\gamma_{se} = 0$.

While a more detailed analysis (at higher frequencies and/or higher current densities) comparing continuum and kinetic simulations is imperative as discussed above, this comparison shows that continuum simulations using non-Maxwellian EEDFs predicted by BOLSIG+ are likely to be more accurate than continuum simulations using a Maxwellian EEDF for microwave microplasmas. Also, the simulations presented here have fewer input parameters when compared to the drift-diffusion model that include an equation for effective electric field. Unlike the direct-current microplasmas considered earlier, the microwave microplasmas that were considered here did not have any contribution from secondary electron emission and hence did not have the influence of runaway electrons. This is one of the reasons for excellent agreement between kinetic and continuum simulations based on the non-Maxwellian EEDF. It should be reiterated that the continuum model used here does not use the drift-diffusion formulation and consequently does not require the effective electric field approach even at high frequencies encountered here.

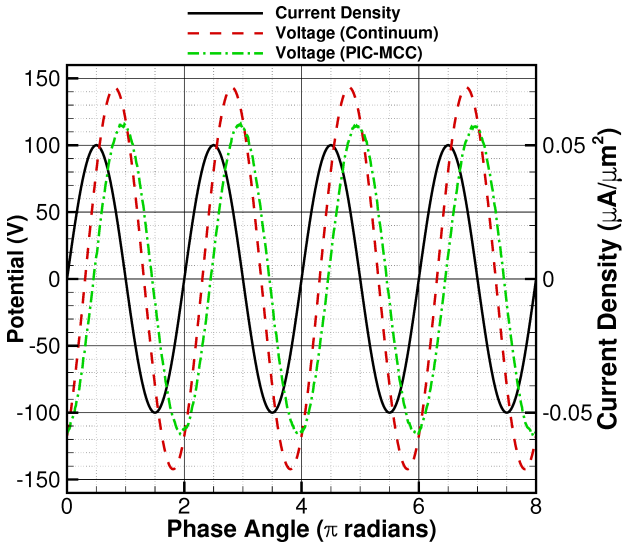

Figure 4.24: Comparison of history profiles of current density and applied potential obtained using PIC-MCC and continuum simulations (non-Maxwellian EEDF) of an argon microplasma operating in a 200 μm gap at a current density amplitude of 0.05 $\mu A/\mu m^2$, frequency of 0.5 GHz and $\gamma_{se} = 0$.

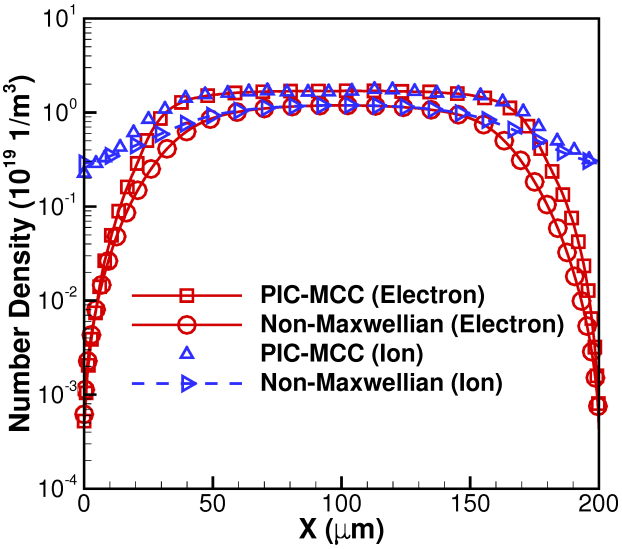

Figure 4.25: Comparison of number density profiles obtained using PIC-MCC and continuum simulations non-Maxwellian EEDF) of an argon microplasma operating in a 200 μm gap at a current density amplitude of 0.05 $\mu A/\mu m^2$, frequency of 0.8 GHz and $\gamma_{se} = 0$.

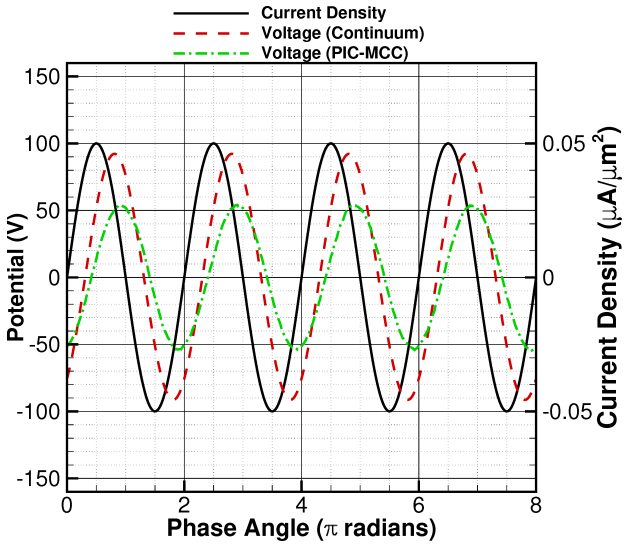

Figure 4.26: Comparison of history profiles of current density and applied potential obtained using PIC-MCC and continuum simulations (non-Maxwellian EEDF) of an argon microplasma operating in a 200 μm gap at a current density amplitude of 0.05 $\mu A/\mu m^2$, frequency of 0.8 GHz and $\gamma_{se} = 0$.

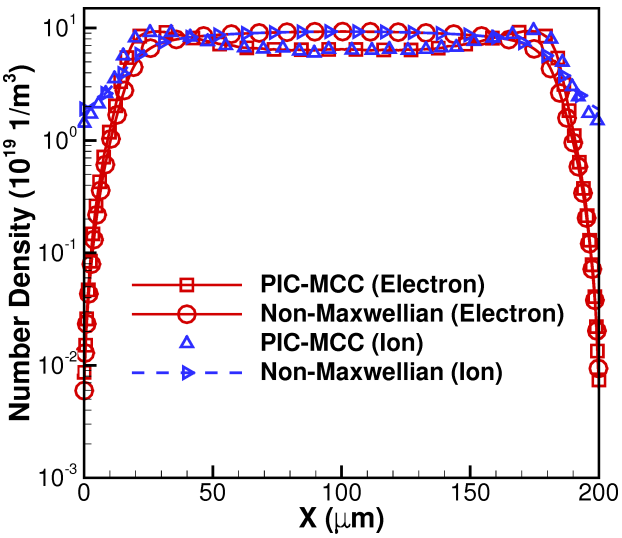

Figure 4.27: Comparison of number density profiles obtained using PIC-MCC and continuum simulations non-Maxwellian EEDF) of an argon microplasma operating in a 200 μm gap at a current density amplitude of 0.4 $\mu A/\mu m^2$, frequency of 2 GHz and $\gamma_{se} = 0$.

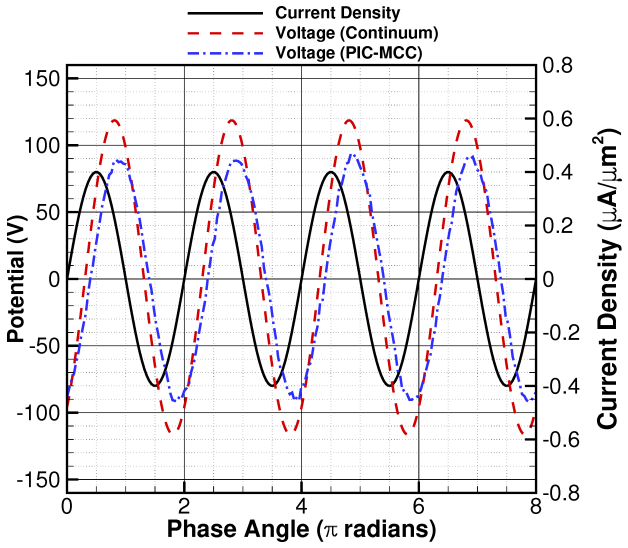

Figure 4.28: Comparison of history profiles of current density and applied potential obtained using PIC-MCC and continuum simulations (non-Maxwellian EEDF) of an argon microplasma operating in a 200 μm gap at a current density amplitude of 0.4 $\mu A/\mu m^2$, frequency of 2 GHz and $\gamma_{se} = 0$.

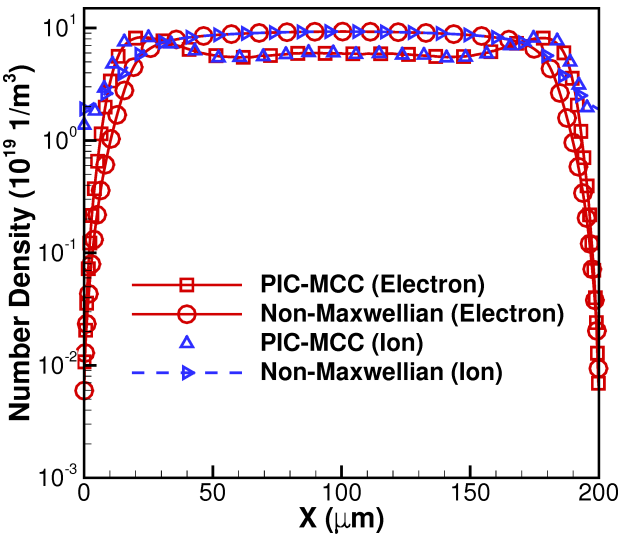

Figure 4.29: Comparison of number density profiles obtained using PIC-MCC and continuum simulations non-Maxwellian EEDF) of an argon microplasma operating in a 200 μm gap at a current density amplitude of 0.4 $\mu A/\mu m^2$, frequency of 4 GHz and $\gamma_{se} = 0$.

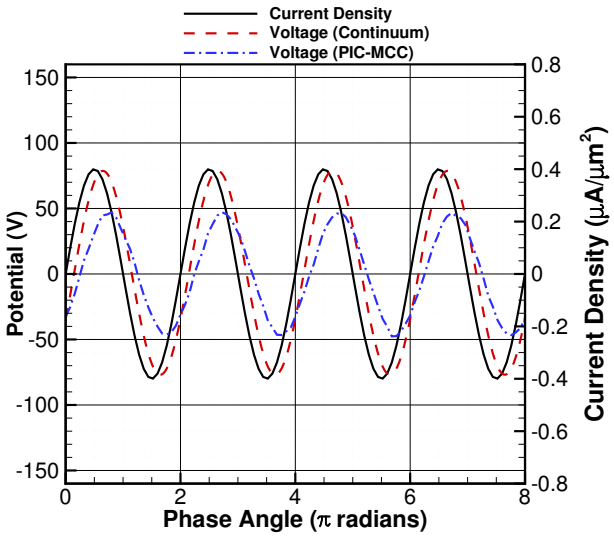

Figure 4.30: Comparison of history profiles of current density and applied potential obtained using PIC-MCC and continuum simulations (non-Maxwellian EEDF) of an argon microplasma operating in a 200 μm gap at a current density amplitude of 0.4 $\mu A/\mu m^2$, frequency of 4 GHz and $\gamma_{se} = 0$.

Chapter 5

Conclusions

This dissertation includes simulation framework development and simulation studies of low temperature microplasmas. The keystone of this research is the numerical framework development included in chapter 3. Chapter 4 addresses a couple of fundamental questions of the adequacy of continuum simulation for microplasma simulations.

5.1 Summary

The development of a high-performance computational framework for the simulation of low-temperature plasmas was described with emphasis on its general capabilities, model formulation, and performance. SOMAFOAM is an open source code that utilizes the finite volume method framework of OpenFOAM solver suite thereby retaining all of its features including the ability to handle arbitrary geometry/mesh, chemical reactions, choice of a variety of numerical schemes for spatial/time discretization and parallel simulations to name a few. The governing equations solved by SOMAFOAM were described in detail including boundary conditions with the understanding that the open source nature of the code allows for the implementation of new models/boundary conditions as long as they could be described using mathematical equations. The presented code for simulating plasma includes descriptions of the kernels used to create plasma governing equations, auxiliary kernels for computing important system variables, libraries used to describe features of the plasma specie, boundary conditions describing the interactions of our domains with the environment, and interfacial kernels for connecting the physics in the plasma and dielectric domains.

The current version of the code is capable of solving the full-momentum equation

for all species or a combination of drift-diffusion approximation and full-momentum equation as specified by the user. Several classical benchmark problems were considered for simulation using SOMAFOAM in such a way that a wide range of operating pressures (0.03 Torr - 760 Torr), excitation frequencies (direct current to microwave) and complexity of geometry (simple one-dimensional to curved surfaces) were covered. The simulations reported here were verified (with prior numerical work) or validated (using experimental data) whenever possible. Finally, we also considered the parallel performance of the code by performing three-dimensional simulations of the GEC reference cell and demonstrated good speedup and scaling efficiency for up to 512 cores. While the code in its current form is quite general and can be expected to be beneficial for several research groups, the highly modular implementation (that is a feature of solvers built on OpenFOAM) also allows for significant extension.

A systematic comparative study of kinetic simulations using the particle-in-cell with Monte Carlo collisions (PIC-MCC) method and continuum simulations using the full-momentum two-fluid model was performed for one-dimensional argon microplasmas operating at a wide range of conditions. The continuum simulations were performed by assuming a Maxwellian electron energy distribution at the local electron temperature as well as a non-Maxwellian electron energy distribution function that was obtained using BOLSIG+. The first set of comparative simulations assessed the influence of product of pressure and gap for a 100 μm direct current argon microplasma. It was demonstrated that the continuum simulations under-predicted the plasma number densities with the non-Maxwellian continuum simulations predicting a number density that was an order of magnitude lower (for $pd = 1$) than the PIC-MCC simulations. The Maxwellian continuum simulations performed better with the agreement with PIC-MCC simulations increasing with pd. The higher plasma number densities predicted by the PIC-MCC simulations was attributed to the secondary electrons that were accelerated in the sheath thereby leading to a high-energy tail that could not be accounted for in the continuum simulations. Two-temperature continuum models that include two electron temperature are therefore likely to perform better and need to be formulated in order to enhance the predictive utility of continuum models especially for device simulations where kinetic simulations may be infeasible. The comparative simulations when repeated for an argon microwave microplasma operating at 0.5 GHz showed that the Maxwellian continuum simulations lead to a significant over-prediction of plasma number densities. However, unlike the direct current simulations, the non-Maxwellian continuum simulations and PIC-MCC simulations predicted almost identical results for microplasmas operating at 0.5 GHz, 0.8 GHz, 2 GHz, and 4 GHz thereby providing a stronger proof that the discrepancy in direct current simulations is due to secondary/boundary processes that were insignificant in microwave microplasmas. Finally, the PIC-MCC simulations predicted

a lower voltage (and power) for a given current density as a result of the inclusion of both ohmic heating and stochastic heating unlike the continuum simulations where ohmic heating is the only mechanism. While comparison with experiments was not performed, PIC-MCC simulations can be expected to be more accurate as a result of the fewer approximations involved and can be a valuable tool for benchmarking continuum simulations. For researchers utilizing the traditional continuum methods, this work serves as a documentation of the potential discrepancies of their results when compared with PIC-MCC simulations. We anticipate that the information presented in this work will aid in the decision-making including design and optimization of microplasma devices apart from triggering the interest for other similar studies at various operating conditions.

5.2 Recommendation for future research

A natural extension of this work is to develop fully coupled plasma and electromagnetics description. Studies in other areas of computational science have shown that fully coupled methods achieves more robust convergence than segregated methods [31]. In the long term, higher order discretization methods can be used to improve the accuracy and efficiency of numerical solution of plasma and Maxwell's equations along with high order temporal schemes.

The development of matrix-free implicit Coupled LU-SGS solver [62] formulation could be a topic of interest. The LU-SGS factorization is useful to accelerate the convergence and reduce the memory requirements with good stability properties.

Adaptive mesh refinement can be useful for modeling low temperature plasmas to significantly reduce the computational cost. During the transient simulation of plasma, the requirement of mesh resolution varies significantly to resolve plasma dynamics, hence adaptive mesh refinement could be used to minimize the number of mesh cells.

Bibliography

[1] Ankur Agarwal, Shahid Rauf, and Ken Collins. "Gas heating mechanisms in capacitively coupled plasmas". In: *Plasma Sources Science and Technology* 21.5 (Aug. 2012), p. 055012.

[2] Arghavan Alamatsaz and Ayyaswamy Venkattraman. "A kinetic study of electron heating and plasma dynamics in microwave microplasmas". In: *Physics of Plasmas* 26.1 (2019), p. 013512.

[3] Rocco Arpa and Domenic D'Ambrosio. "High-order accurate implicit scheme for drift-diffusion equations and application to dielectric barrier discharges". In: *40th AIAA Plasmadynamics and Lasers Conference*. 2009, p. 3909.

[4] Adam Bass, Conrad Chevalier, and M. W. Blades. "A capacitively coupled microplasma (CCμP) formed in a channel in a quartz wafer". In: *J. Anal. At. Spectrom.* 16 (9 2001), pp. 919–921. DOI: 10.1039/B103507J.

[5] E. Basurto et al. "Mobility of He^+, Ne^+, Ar^+, N_2^+, O_2^+, and CO_2^+ in their parent gas". In: *Phys. Rev. E* 61 (3 Mar. 2000), pp. 3053–3057.

[6] Marsha Berger, Michael Aftosmis, and Scott Muman. "Analysis of slope limiters on irregular grids". In: *43rd AIAA Aerospace Sciences Meeting and Exhibit*, p. 490.

[7] JP Boeuf and LC Pitchford. "Two-dimensional model of a capacitively coupled rf discharge and comparisons with experiments in the Gaseous Electronics Conference reference reactor". In: *Physical Review E* 51.2 (1995), p. 1376.

[8] L. Boltzmann. "Weitere studien über das wärmegleichgewicht unter Gasmolekülen". In: *Sit. Akad. Wiss. (Wiener Berichte)* 66 (1872), p. 275.

[9] Ronny Brandenburg. "Dielectric barrier discharges: progress on plasma sources and on the understanding of regimes and single filaments". In: *Plasma Sources Science and Technology* 26.5 (Mar. 2017), p. 053001.

[10] W. J. M. Brok et al. "Numerical description of discharge characteristics of the plasma needle". In: *Journal of Applied Physics* 98.1 (2005), p. 013302.

[11] A.H.L.M. Charin et al. "A Moving Mesh Interface Tracking Method for Simulation of Liquidliquid Systems". In: *J. Comput. Phys.* 334.C (Apr. 2017), pp. 419–441. ISSN: 0021-9991.

[12] Guangye Chen and Laxminarayan L. Raja. "Fluid modeling of electron heating in low-pressure, high-frequency capacitively coupled plasma discharges". In: *Journal of Applied Physics* 96.11 (2004), pp. 6073–6081.

[13] K.-F. Chen and J. G. Eden. "The plasma transistor: A microcavity plasma device coupled with a low voltage, controllable electron emitter". In: *Applied Physics Letters* 93.16 (2008), p. 161501. DOI: 10.1063/1.2981573.

[14] J. Choi et al. "Electron and Ion Kinetics in a DC Microplasma at Atmospheric Pressure". In: *IEEE Transactions on Plasma Science* 35.5 (2007), pp. 1274–1278.

[15] Phillip Colella, Milo R Dorr, and Daniel D Wake. "A Conservative Finite Difference Method for the Numerical Solution of Plasma Fluid Equations". In: *Journal of Computational Physics* 149.1 (1999), pp. 168–193. ISSN: 0021-9991.

[16] Phillip Colella, Milo R Dorr, and Daniel D Wake. "Numerical Solution of Plasma Fluid Equations Using Locally Refined Grids". In: *Journal of Computational Physics* 152.2 (1999), pp. 550–583. ISSN: 0021-9991.

[17] T. Deconinck, S. Mahadevan, and L.L. Raja. "Discretization of the Joule heating term for plasma discharge fluid models in unstructured meshes". In: *Journal of Computational Physics* 228.12 (2009), pp. 4435–4443. ISSN: 0021-9991.

[18] Jan van Dijk et al. "The plasma modelling toolkit Plasimo". In: *Journal of Physics D: Applied Physics* 42.19 (2009), p. 194012.

[19] H.W. Ellis et al. "Transport properties of gaseous ions over a wide energy range". In: *Atomic Data and Nuclear Data Tables* 17.3 (1976), pp. 177–210. ISSN: 0092-640X.

[20] H. Feng et al. "The Interaction of a Direct-Current Cold Atmospheric-Pressure Air Plasma With Bacteria". In: *IEEE Transactions on Plasma Science* 37.1 (2009), pp. 121–127.

[21] R. Fitzpatrick. *Plasma Physics: An Introduction*. Taylor & Francis, 2014. ISBN: 9781466594265.

[22] L. S. Frost and A. V. Phelps. "Momentum-Transfer Cross Sections for Slow Electrons in He, Ar, Kr, and Xe from Transport Coefficients". In: *Phys. Rev.* 136 (6A Dec. 1964), A1538–A1545. DOI: 10.1103/PhysRev.136.A1538.

[23] L. S. Frost and A. V. Phelps. "Momentum-Transfer Cross Sections for Slow Electrons in He, Ar, Kr, and Xe from Transport Coefficients". In: *Phys. Rev.* 136 (6A Dec. 1964), A1538–A1545. DOI: 10.1103/PhysRev.136.A1538.

[24] Christophe Geuzaine and Jean-François Remacle. "Gmsh: A 3-D finite element mesh generator with built-in pre-and post-processing facilities". In: *International journal for numerical methods in engineering* 79.11 (2009), pp. 1309–1331.

[25] V A Godyak, R B Piejak, and B M Alexandrovich. "Measurement of electron energy distribution in low-pressure RF discharges". In: *Plasma Sources Science and Technology* 1.1 (Mar. 1992), pp. 36–58.

[26] J. Gregório, A. R. Hoskinson, and J. Hopwood. "Modeling of microplasmas from GHz to THz". In: *Journal of Applied Physics* 118.8 (2015), p. 083305. DOI: 10.1063/1.4928468.

[27] José Gregório, Stephen Parsons, and Jeffrey Hopwood. "Microwave harmonic generation and nonlinearity in microplasmas". In: *Plasma Sources Science and Technology* 25.3 (Apr. 2016), p. 035018. DOI: 10.1088/0963-0252/25/3/035018.

[28] J Gregório et al. "Self-consistent modelling of atmospheric micro-plasmas produced by a microwave source". In: *Plasma Sources Science and Technology* 21.1 (2012), p. 015013.

[29] G J M Hagelaar and L C Pitchford. "Solving the Boltzmann equation to obtain electron transport coefficients and rate coefficients for fluid models". In: *Plasma Sources Science and Technology* 14.4 (Oct. 2005), pp. 722–733.

[30] P. J. Hargis et al. "The Gaseous Electronics Conference radio-frequency reference cell: A defined parallel-plate radio-frequency system for experimental and theoretical studies of plasma-processing discharges". In: *Review of Scientific Instruments* 65.1 (1994), pp. 140–154.

[31] Matthias Heil, Andrew L Hazel, and Jonathan Boyle. "Solvers for large-displacement fluid–structure interaction problems: segregated versus monolithic approaches". In: *Computational Mechanics* 43.1 (2008), pp. 91–101.

[32] Roger W Hockney and James W Eastwood. *Computer simulation using particles*. crc Press, 1988.

[33] Yong Jun Hong et al. "Modeling High-Pressure Microplasmas: Comparison of Fluid Modeling and Particle-in-Cell Monte Carlo Collision Modeling". In: *Plasma Processes and Polymers* 5.6 (2008), pp. 583–592. DOI: 10.1002/ppap.200800024.

[34] Jeffrey Hopwood, Alan R Hoskinson, and José Gregório. "Microplasmas ignited and sustained by microwaves". In: *Plasma Sources Science and Technology* 23.6 (Dec. 2014), p. 064002. DOI: 10.1088/0963-0252/23/6/064002. URL: https://doi.org/10.1088%2F0963-0252%2F23%2F6%2F064002.

[35] Alan R. Hoskinson, Stephen Parsons, and Jeffrey Hopwood. "Gas breakdown and plasma impedance in split-ring resonators". In: *The European Physical Journal D* 70.2 (Feb. 2016), p. 30. ISSN: 1434-6079.

[36] Alan R Hoskinson et al. "Electron confinement and heating in microwave-sustained argon microplasmas". In: *Journal of Applied Physics* 117.16 (2015), p. 163301.

[37] L. G. H. Huxley and R. W. Crompton. "The Diffusion and Drift of Electrons in Gases". In: *Interscience, New York: Wiley* (1974).

[38] Akinori Iwai et al. "Experimental observation and model analysis of second-harmonic generation in a plasma-metamaterial composite". In: *Applied Physics Express* 8.5 (Apr. 2015), p. 056201.

[39] F. Iza and J. A. Hopwood. "Low-power microwave plasma source based on a microstrip split-ring resonator". In: *IEEE Transactions on Plasma Science* 31.4 (Aug. 2003), pp. 782–787.

[40] F. Iza and J. A. Hopwood. "Rotational, vibrational, and excitation temperatures of a microwave-frequency microplasma". In: *IEEE Transactions on Plasma Science* 32.2 (2004), pp. 498–504.

[41] F Iza and J Hopwood. "Split-ring resonator microplasma: microwave model, plasma impedance and power efficiency". In: *Plasma Sources Science and Technology* 14.2 (May 2005), pp. 397–406. DOI: 10.1088/0963-0252/14/2/023.

[42] Felipe Iza and J Hopwood. "Influence of operating frequency and coupling coefficient on the efficiency of microfabricated inductively coupled plasma sources". In: *Plasma sources science and technology* 11.3 (2002), p. 229.

[43] George Karypis and Vipin Kumar. "A Fast and High Quality Multilevel Scheme for Partitioning Irregular Graphs". In: *SIAM J. Sci. Comput.* 20.1 (Dec. 1998), pp. 359–392. ISSN: 1064-8275.

[44] Carl T Kelley. *Iterative methods for linear and nonlinear equations*. SIAM, 1995.

[45] H C Kim et al. "Particle and fluid simulations of low-temperature plasma discharges: benchmarks and kinetic effects". In: *Journal of Physics D: Applied Physics* 38.19 (2005), R283.

[46] H C Kim et al. "Particle and fluid simulations of low-temperature plasma discharges: benchmarks and kinetic effects". In: *Journal of Physics D: Applied Physics* 38.19 (Sept. 2005), R283–R301. DOI: 10.1088/0022-3727/38/19/r01.

[47] Prashanth S. Kothnur and Laxminarayan L. Raja. "Two-dimensional simulation of a direct-current microhollow cathode discharge". In: *Journal of Applied Physics* 97.4 (2005), p. 043305.

[48] P. Kuberry, P. Bochev, and K. Peterson. "An Optimization-Based Approach for Elliptic Problems with Interfaces". In: *SIAM Journal on Scientific Computing* 39.5 (2017), S757–S781.

[49] Mark J Kushner. "Hybrid modelling of low temperature plasmas for fundamental investigations and equipment design". In: *Journal of Physics D: Applied Physics* 42.19 (2009), p. 194013.

[50] Mark J Kushner. "Modelling of microdischarge devices: plasma and gas dynamics". In: *Journal of Physics D: Applied Physics* 38.11 (May 2005), pp. 1633–1643.

[51] H. C. Kwon et al. "Abnormal electron-heating mode and formation of secondary-energetic electrons in pulsed microwave-frequency atmospheric microplasmas". In: *Physics of Plasmas* 21.3 (2014), p. 033511. DOI: 10.1063/1.4870005.

[52] A. B. Langdon. "Evolution of Particle-in-Cell Plasma Simulation". In: *IEEE Transactions on Plasma Science* 42.5 (2014), pp. 1317–1320.

[53] L Lauro-Taroni, MM Turner, and N StJ Braithwaite. "Analysis of the excited argon atoms in the GEC RF reference cell by means of one-dimensional PIC simulations". In: *Journal of Physics D: Applied Physics* 37.16 (2004), p. 2216.

[54] M. U. Lee et al. "Non-Maxwellian to Maxwellian transitions of atmospheric microplasmas at microwave frequencies". In: *Physics of Plasmas* 23.7 (2016), p. 070704. DOI: 10.1063/1.4959857.

[55] Dmitry Levko. "Electron kinetics in a microdischarge in nitrogen at atmospheric pressure". In: *Journal of Applied Physics* 114.22 (2013), p. 223302. DOI: 10.1063/1.4848055.

[56] Dmitry Levko and Laxminarayan L. Raja. "Effect of frequency on microplasmas driven by microwave excitation". In: *Journal of Applied Physics* 118.4 (2015), p. 043303. DOI: 10.1063/1.4927535.

[57] Dmitry Levko and Laxminarayan L. Raja. "Fluid modeling of a high-voltage nanosecond pulsed xenon microdischarge". In: *Physics of Plasmas* 23.7 (2016), p. 073513. DOI: 10.1063/1.4959172.

[58] Dmitry Levko and Laxminarayan L. Raja. "Fluid modeling of a high-voltage nanosecond pulsed xenon microdischarge". In: *Physics of Plasmas* 23.7 (2016), p. 073513. DOI: 10.1063/1.4959172.

[59] Michael A. Lieberman and Allan J. Lichtenberg. "Principles of Plasma Discharges and Materials Processing: Lieberman/Plasma 2e". In: 2005.

[60] A. D. Lindsay. "Coupling of Plasmas and Liquids". PhD thesis. North Carolina State University, 2016.

[61] Alexander D Lindsay, David B Graves, and Steven C Shannon. "Fully coupled simulation of the plasma liquid interface and interfacial coefficient effects". In: *Journal of Physics D: Applied Physics* 49.23 (May 2016), p. 235204.

[62] Hong Luo, Joseph D Baum, and Rainald Löhner. "An accurate, fast, matrix-free implicit method for computing unsteady flows on unstructured grids". In: *Computers & fluids* 30.2 (2001), pp. 137–159.

[63] D.P. Lymberopoulos and D.J. Economou. "Two-dimensional self-consistent radio frequency plasma simulations relevant to the Gaseous Electronics Conference RF Reference Cell". In: *Journal of Research of the National Institute of Standards and Technology* 100.4 (July 1995).

[64] Shev MacNamara and Gilbert Strang. "Operator Splitting". In: *Splitting Methods in Communication, Imaging, Science, and Engineering*. Ed. by Roland Glowinski, Stanley J. Osher, and Wotao Yin. Cham: Springer International Publishing, 2016, pp. 95–114. ISBN: 978-3-319-41589-5.

[65] Davide Mariotti and R Mohan Sankaran. "Microplasmas for nanomaterials synthesis". In: *Journal of Physics D: Applied Physics* 43.32 (July 2010), p. 323001. DOI: 10.1088/0022-3727/43/32/323001.

[66] T. Martens et al. "The dominant role of impurities in the composition of high pressure noble gas plasmas". In: *Applied Physics Letters* 92.4 (2008), p. 041504.

[67] M. Miclea et al. "The dielectric barrier discharge — a powerful microchip plasma for diode laser spectrometry". In: *Spectrochimica Acta Part B: Atomic Spectroscopy* 56.1 (2001), pp. 37–43. ISSN: 0584-8547.

[68] A-AH Mohamed, JF Kolb, and KH Schoenbach. "Low temperature, atmospheric pressure, direct current microplasma jet operated in air, nitrogen and oxygen". In: *The European Physical Journal D* 60.3 (2010), pp. 517–522.

[69] J. H. Morrison. *A compressible Navier-Stokes solver with two-equation and Reynolds stress turbulence closure models*. Tech. rep. May 1992.

[70] Lawrence J. Overzet and Michael B. Hopkins. "Comparison of electron-density measurements made using a Langmuir probe and microwave interferometer in the Gaseous Electronics Conference reference reactor". In: *Journal of Applied Physics* 74.7 (1993), pp. 4323–4330.

[71] Lawrence J. Overzet and Michael B. Hopkins. "Spatial variations in the charge density of argon discharges in the Gaseous Electronics Conference reference reactor". In: *Applied Physics Letters* 63.18 (1993), pp. 2484–2486.

[72] P. Pai and M. Tabib-Azar. "Micro-Plasma Field Effect Transistor Operating With DC Plasma". In: *IEEE Electron Device Letters* 35.5 (2014), pp. 593–595.

[73] P. Pai and M. Tabib-Azar. "SUB 3-micron gap microplasma fet with 50 V turn-on voltage". In: *2014 IEEE 27th International Conference on Micro Electro Mechanical Systems (MEMS)*. 2014, pp. 171–174.

[74] S. G. Parsons and J. Hopwood. "Millimeter Wave Plasma Formation Within a 2D Photonic Crystal". In: *IEEE Electron Device Letters* 38.11 (2017), pp. 1602–1605.

[75] L C Pitchford et al. "Comparisons of sets of electron–neutral scattering cross sections and swarm parameters in noble gases: I. Argon". In: *Journal of Physics D: Applied Physics* 46.33 (Aug. 2013), p. 334001. DOI: 10.1088/0022-3727/46/33/334001.

[76] Osamu Sakai and Kunihide Tachibana. "Plasmas as metamaterials: a review". In: *Plasma Sources Science and Technology* 21.1 (Jan. 2012), p. 013001. DOI: 10.1088/0963-0252/21/1/013001.

[77] Y Sakiyama and D B Graves. "Finite element analysis of an atmospheric pressure RF-excited plasma needle". In: *Journal of Physics D: Applied Physics* 39.16 (Aug. 2006), pp. 3451–3456.

[78] Y Sakiyama, D B Graves, and E Stoffels. "Influence of electrical properties of treated surface on RF-excited plasma needle at atmospheric pressure". In: *Journal of Physics D: Applied Physics* 41.9 (Apr. 2008), p. 095204.

[79] Karl H Schoenbach et al. "High-pressure hollow cathode discharges". In: *Plasma Sources Science and Technology* 6.4 (Nov. 1997), pp. 468–477. DOI: 10.1088/0963-0252/6/4/003.

[80] Pramod K Singh, Jeffrey Hopwood, and Sameer Sonkusale. "Metamaterials for remote generation of spatially controllable two dimensional array of microplasma". In: *Scientific reports* 4 (2014), p. 5964.

[81] R E J Sladek and E Stoffels. "Deactivation ofEscherichia coliby the plasma needle". In: *Journal of Physics D: Applied Physics* 38.11 (May 2005), pp. 1716–1721.

[82] R. H. Stark et al. "Microhollow cathode discharges in atmospheric air". In: *IEEE Conference Record - Abstracts. 1999 IEEE International Conference on Plasma Science. 26th IEEE International Conference (Cat. No.99CH36297).* 1999, pp. 117–.

[83] E. Stoffels, R. E. J. Sladek, and I. E. Kieft. "Gas Plasma Effects on Living Cells". In: *Physica Scripta* T107.5 (2004), p. 79.

[84] E Stoffels, I E Kieft, and R E J Sladek. "Superficial treatment of mammalian cells using plasma needle". In: *Journal of Physics D: Applied Physics* 36.23 (Nov. 2003), pp. 2908–2913.

[85] G. Strang. "On the Construction and Comparison of Difference Schemes". In: *SIAM Journal on Numerical Analysis* 5 (Sept. 1968), pp. 506–517.

[86] Peter K Sweby. "High resolution schemes using flux limiters for hyperbolic conservation laws". In: *SIAM journal on numerical analysis* 21.5 (1984), pp. 995–1011.

[87] John Sealy Edward Townsend. "The diffusion of ions into gases". In: *Proceedings of the Royal Society of London* 65.413-422 (1900), pp. 192–196.

[88] M. M. Turner et al. "Simulation benchmarks for low-pressure plasmas: Capacitive discharges". In: *Physics of Plasmas* 20.1 (2013), p. 013507.

[89] V. Vahedi and M. Surendra. "A Monte Carlo collision model for the particle-in-cell method: applications to argon and oxygen discharges". In: *Computer Physics Communications* 87.1 (1995). Particle Simulation Methods, pp. 179–198. ISSN: 0010-4655. DOI: https://doi.org/10.1016/0010-4655(94)00171-W.

[90] J.P. Verboncoeur et al. "Simultaneous Potential and Circuit Solution for 1D Bounded Plasma Particle Simulation Codes". In: *Journal of Computational Physics* 104.2 (1993), pp. 321–328. ISSN: 0021-9991. DOI: https://doi.org/10.1006/jcph.1993.1034.

[91] Abhishek Kumar Verma, Arghavan Alamatsaz, and Ayyaswamy Venkattraman. "A comparison of continuum and kinetic simulations of moderate pd microplasmas integrated with high secondary yield cathodes". In: *Plasma Processes and Polymers* 14.4-5 (2017), p. 1600130.

[92] Abhishek Kumar Verma, Arghavan Alamatsaz, and Ayyaswamy Venkattraman. "Benchmark continuum and kinetic simulations of argon microplasmas in the direct current and microwave regimes". In: *Journal of Physics D: Applied Physics* 50.42 (2017), p. 424005.

[93] H. G. Weller et al. "A tensorial approach to computational continuum mechanics using object-oriented techniques". In: *Computers in Physics* 12.6 (1998), pp. 620–631.

[94] C. G. Wilson and Y. B. Gianchandani. "Spectral detection of metal contaminants in water using an on-chip microglow discharge". In: *IEEE Transactions on Electron Devices* 49.12 (2002), pp. 2317–2322.

[95] Hao Wu, Peter C. Ma, and Matthias Ihme. "Efficient time stepping for reactive turbulent simulations with stiff chemistry". In: *2018 AIAA Aerospace Sciences Meeting*.

[96] W. Yuan, F. K. Chowdhury, and M. Tabib-Azar. "Microplasma field effect transistors". In: *2012 IEEE 25th International Conference on Micro Electro Mechanical Systems (MEMS)*. 2012, pp. 293–296.

[97] M. Zakari et al. "An Axisymmetric Unstructured Finite Volume Method Applied to the Numerical Modeling of an Atmospheric Pressure Gas Discharge". In: *J. Comput. Phys.* 281.C (Jan. 2015), pp. 473–492. ISSN: 0021-9991.

[98] O Zatsarinny and K Bartschat. "B-spline Breit–Pauli R-matrix calculations for electron collisions with argon atoms". In: *Journal of Physics B: Atomic, Molecular and Optical Physics* 37.23 (Nov. 2004), pp. 4693–4706. DOI: 10.1088/0953-4075/37/23/010.

[99] Xi-Ming Zhu, Wen-Cong Chen, and Yi-Kang Pu. "Gas temperature, electron density and electron temperature measurement in a microwave excited microplasma". In: *Journal of Physics D: Applied Physics* 41.10 (May 2008), p. 105212. DOI: 10.1088/0022-3727/41/10/105212.